ÇUKUROVA UNIVERSITY
INSTITUTE OF NATURAL AND APPLIED SCIENCES

PhD THESIS

Olcay ALTINTAŞ

INDUSTRIAL APPLICATIONS OF METAMATERIAL BASED SENSORS

DEPARTMENT OF ELECTRICAL AND ELECTRONICS ENGINEERING

ADANA-2020

ABSTRACT

PhD THESIS

INDUSTRIAL APPLICATIONS OF METAMATERIAL BASED SENSORS

Olcay ALTINTAŞ

ÇUKUROVA UNIVERSITY
INSTITUTE OF NATURAL AND APPLIED SCIENCES
DEPARTMENT OF ELECTRICAL AND ELECTRONICS ENGINEERING

Supervisor	: Assoc. Prof. Dr. Murat AKSOY
Co-supervisor	: Prof. Dr. Emin ÜNAL
	Year: 2020, Pages: 169
Jury	: Assoc. Prof. Dr. Murat AKSOY
	: Prof. Dr. Emin ÜNAL
	: Prof. Dr. Mustafa GÖK
	: Assoc. Prof. Dr. Muharrem KARAASLAN
	: Asst. Prof. Dr. Şule ÇOLAK

In the industry, the sensor structures must meet crucial requirements such as sensitivity, accuracy and linear response in advance level. With the help of these sensors, it is quite possible to obtain mass manufacturing, low cost and high quality products. Therefore, metamaterial (MTM) based sensor structures have been developed for different application areas in microwave concept. MTMs have strong electrical and magnetic coupling due to their resonator geometry. The sensing abilities of the MTM based sensor structures have been tested both numerically and experimentally. In numerical phase, the sensor structures have been designed by examining dimension and equivalent circuit parameters, electric field and surface current distributions, impedance matching and resonance frequency. In experimental phase, the sensor structures have been produced and the electrical characteristics of the samples have been measured. The transmission/reflection magnitude and resonance frequency variations have been obtained both numerically and the experimentally. The results have been compared and evaluated. Finally, 7 unique sensor structures and a novel approach with artificial neural network (ANN) have been proposed for various industrial applications.

Key Words: MTM, microwave sensors, industrial sensors, microwave resonators, electrical coupling, magnetic coupling, dielectric

ÖZ

DOKTORA TEZİ

METAMALZEME TABANLI SENSÖRLERİN ENDÜSTRİYEL UYGULAMALARI

Olcay ALTINTAŞ

ÇUKUROVA ÜNİVERSİTESİ
FEN BİLİMLERİ ENSTİTÜSÜ
ELEKTRİK – ELEKTRONİK MÜHENDİSLİĞİ ANABİLİM DALI

Danışman : Doç. Dr. Murat AKSOY
İkinci Danışman : Prof. Dr. Emin ÜNAL
Year: 2020, Pages: 169
Jüri : Doç. Dr. Murat AKSOY
: Prof. Dr. Emin ÜNAL
: Prof. Dr. Mustafa GÖK
: Doç. Dr. Muharrem KARAASLAN
: Dr. Öğr. Üyesi Şule ÇOLAK

Endüstride kullanılan sensör yapıları hassasiyet, doğruluk ve doğrusal davranış gibi önemli gereksinimleri ileri düzeyde karşılamalıdır. Bu sensörler yardımıyla seri imalat, düşük maliyetli ve kaliteli ürünler elde etmek oldukça mümkündür. Bu nedenle, mikrodalga konseptinde farklı uygulama alanları için metamalzeme (MTM) tabanlı sensör yapıları geliştirilmiştir. MTM'ler, rezonatör geometrileri nedeniyle güçlü elektriksel ve manyetik etkileşime sahiptir. MTM tabanlı sensör yapılarının algılama yetenekleri hem sayısal hem de deneysel olarak test edilmiştir. Sayısal aşamada, boyut ve eşdeğer devre parametreleri, elektrik alan ve yüzey akım dağılımları, empedans uyumu ve rezonans frekansı incelenerek sensor yapıları tasarlanmıştır. Deneysel aşamada sensör yapıları üretilmiş ve numunelerin elektriksel özellikleri ölçülmüştür. İletim/yansıma büyüklüğü ve rezonans frekansı değişimleri hem sayısal hem de deneysel olarak elde edilmiştir. Sonuçlar karşılaştırılmış ve değerlendirilmiştir. Sonuç olarak, çeşitli endüstriyel uygulamalar için 7 benzersiz sensör yapısı ve yapay sinir ağı (YSA) ile yeni bir yaklaşım önerilmiştir.

Anahtar Kelimeler: MTM, mikrodalga sensörler, endüstriyel sensörler, mikrodalga resonatörler, elektriksel etkileşim, manyetik etkileşim, dielektrik

EXTENDED SUMMARY

Growing and improving industry needs technological developments more than ever for mass and safe production. Therefore, improving novel sensing techniques instead of traditional methods is getting more important due to robotic and artificial intelligence (AI) in accordance with the new industrial developments. This thesis study offers new solutions for many industrial issues with novel sensing structures having more sensitivity and durability. The designated sensor structures are inspired from the MTM resonators with unique geometries. These resonators have stronger electrical and magnetic coupling than usual ones since their inductive and capacitive layers are easily manipulated. The sensor studies are focused on electrical variations of samples such as ethanol water mixtures, lubricant oil, gasoline diesel and etc. These samples placed on the sensing layer of the proposed sensor structure changes of the electrical properties of the sensing mechanism. In this way, the sensing processes are realized by observing resonance frequency variations and/or transmission/reflection magnitude differences of the sensor structures.

The sensor studies have been achieved by comparing and evaluating numerical and experimental results. In numerical studies, the sensor structure has been designed and it has been examined in many respects. Computer simulation technology (CST) Microwave Simulation software has been used to get numerical results. In this phase, sensor designs, parametric studies, electric field and surface current distributions, impedance matching plots with real and imaginary parts of impedance, equivalent circuit diagrams, and the other numerical calculations have been realized by CST Microwave Simulation program. In addition, the transmission and reflection coefficient in microwave frequency axis has been observed by placing samples with different dielectric properties. In experimental studies, the sensor structures are produced by a computer numerical control (CNC) based LPKF E33 printed circuit board (PCB) prototyping machine. After that, the connector soldering process is made for transmission line based implementations. The produced sensor

structure is placed to the sample holder with a waveguide and two suitable adapters for waveguide based implementations. The experimental analysis of the sensing studies has been realized by using PNA-L model Agilent vector network analyzer (VNA) having an operating frequency range between 10 MHz – 43.5 GHz. The transmission and/or reflection coefficient are obtained by using VNA calibrating desired frequency ranges. Moreover, the electrical characteristics of the samples are determined by a dielectric probe connected to the VNA.

Circular split ring resonator (CSRR) based sensor structure has been proposed for various applications such as strain, micro-fluid and rotation sensing. The center gap of the circular path is chosen as the sensing layer. The study has been realized between 3 GHz and 5 GHz. The electrical characteristics of the ethanol water mixtures with different ethanol ratios are determined for liquid sensing application. The metallic rods with various thickness has been selected and inserted in the sensing layer to monitor capacitive changes which effects resonance in strain sensing application. A 0.8 mm thick metal rod has been chosen and placed in the sensing layer at different theta angles ($-90 \leq \theta \leq 90$) to observe rotation sensing ability of the proposed sensor structure.

Chemical liquid and transformer oil quality sensing study have been achieved by labyrinth type resonator (LTR) based sensor structure with transmission line implantation. The study is performed between the frequencies of 4 GHz and 5 GHz. Liquid sensing ability of the sensor structure has been firstly tested by ethanol water mixture with different ethanol ratios. The linear relationship between resonance frequency and ethanol ratio in the mixture has been monitored. Different chemical liquids with common properties such as color and odor have been used to test the distinctive feature of the study. In the transformer oil quality application, waste and clean transformer oil has been distinguished with non-destructive technique.

A microfluidic sensor structure has been proposed for operating frequency configuration study. The split ring resonator based sensor has been used for this application. The sensor structure has been firstly tested by ethanol water mixtures. A multiplier namely as ‘k’ having five different numbers as 1.4, 1.2, 1.0, 0.8 and 0.6 is used for dimension configuration of resonator. The operating frequency ranges of these five structure configured with multiplier k have been monitored. The linear relationship between the operating frequency shift and multiplier k has been obtained.

Double split ring resonator (DSRR) based microfluidic sensor structure with transmission line implementation has been proposed for wastewater treatment facilities. The dielectric properties of the wastewater samples in ventilation, back return and output process has been firstly measured. These samples is then placed to the sensing layer of the DSRR based sensor. The resonance frequency point difference has been finally monitored and the sensor structure is a good candidate to analyze wastewater quality with respect to suspended solid, colloid and/or organic/inorganic matter.

Split meander line resonator (SMLR) based permittivity and thickness sensor has been studied for dielectric materials having flat surfaces. The study is achieved in X band frequency regime with waveguide implementation. Various type of dielectric layers have been used to verify permittivity sensing ability of the structure. The Arlon and Rogers type of dielectric substrates having different thickness has been chosen for thickness sensing applications. The linear relation between thickness and resonance frequency has been observed.

An omega shaped resonator (OSR) based sensor structure has been implemented for four different discriminating applications at X band frequency regime with waveguide implementation. The discriminant applications have been carried out between (i) authentic and inauthentic gasoline samples, (ii) authentic and inauthentic diesel samples, (iii) clean and waste lubricant samples and (iv) clean and waste transformer oil samples. The results have been precisely obtained and the proposed structure can be used efficiently in many industrial applications as it has a non-destructive technique.

LC resonator type MTM based sensor structure has been performed for the engine lubricant oil quality detection study. Clean and waste lubricant oil samples are firstly examined in terms of electrical characteristics via dielectric probe kit. These samples have been then placed on the sensing layer of the proposed sensor structure to be distinguished from each other. The study has been achieved at X band with waveguide implementation and result has been monitored as 100 MHz of resonance frequency difference.

A novel approach is proposed for detection locomotive maintenance technique by monitoring dielectric properties of lubricants instead of old traditional, high cost and time consume applications. This new technique focuses on relation between the contaminant in the lube oil and electrical characteristics of lube oil samples. Hence the ANN method is performed to monitor linear relationship between observed and estimated dielectric properties of lubricant samples. The study is carried out at four different frequencies and the regression coefficients of dielectric constant and dielectric loss for four different frequencies are 0.7239, 0.7951, 0.8513, 0.7463 and 0.7627, 0.7196, 0.8015, 0.7334, respectively. In addition, the mean square error (MSE), mean absolute error (MAE) and mean absolute percentage error (MAPE) have been estimated and evaluated.

ACKNOWLEDGEMENTS

I would like to thank to my supervisor Assoc. Prof. Dr. Murat AKSOY and my co-supervisor Prof. Dr. Emin ÜNAL for their mentoring, advice, criticism and understanding through the preparations of this study. Without their help, guidance, cooperation and encouragement I would not have an opportunity to accomplish my thesis.

I wish to express my special thanks to Assoc. Prof. Dr. Muharrem KARAASLAN, Prof. Dr. Mustafa GÖK and Assoc. Prof. Dr. Oğuzhan AKGÖL whose suggestions and very constructive criticisms have contributed immensely to the evolution of my ideas on my thesis.

I would also thank to my parents and my wife Gizem BEHZAT ALTINTAŞ for their strong patience and support to me during my researches and my entire life.

The financial support of Scientific Project Unit of Cukurova University (Project Number: FDK-2018-10488) during my Ph.D. is gratefully acknowledged.

Finally, I acknowledge Turkish State Railway (TSR) for supporting my research.

CONTENTS **PAGE**

LIST OF TABLES **PAGE**

LIST OF FIGURES **PAGE**

LIST OF ABBREVIATIONS

A : Amperes
AI : Artificial Intelligence
ANN : Artificial Neural Networks
CNC : Computer Numerical Control
CSRR : Circular Split Ring Resonator
CST : Computer Simulation Technology
DSRR : Double Split Ring Resonator
EM : Electromagnetic
FEM : Finite Element Method
FIT : Finite Integration Technique
FR4 : Flame Retardant 4
GHz : Gigahertz
Hz : Hertz
KW : Kilo Watts
KHz : Kilo Hertz
LC : Inductance & Capacitance
LTR : Labyrinth Type Sensor
MAE : Mean Absolute Error
MAPE : Mean Absolute Percentage Error
MHz : Megahertz
MSE : Mean Square Error
MTM : Metamaterial
OSR : Omega Shaped Resonator
P : Power
PCB : Printed Circuit Board
PEC : Perfect Electric Conductor
PLA : Polycutic Acid

PPM : Parts Per Million
SAM : Spectral Analysis Method
SMLR : Split Meander Line Resonator
SRR : Split Ring Resonator
TE : Transverse Electric
THz : Terahertz
TLM : Transmission Line Matrix Method
TSR : Turkish State Railways
V : Volts
VNA : Vector Network Analyzer

1. INTRODUCTION

1.1. Background

Recently, the researchers have been made a huge efforts to investigate more sensitive sensor structures by exploring new technological areas. It is an important issue to meet medical or industrial needs by improving new sensing techniques. The Industry requires the sensors which have real-time operated without requiring human resources. Moreover, some industrial establishments ask for the sensing mechanism which can be achieved more sensitive, durable and long term stability with non-destructive methods. For instance, the locomotives in railways have huge power engine systems and their maintenance is very crucial for safety and cost of the journey or commercial consignment. Engine failures and maintenances of the locomotives are detected and realized by observing engine lubricant qualities. A real-time operated sensor device is a need in this field. On the one hand, the crack detection and thickness measurement of an iron slab or rod are research topics in the iron steel industry. In this sector and some other chemical industries, the observations of the purity of the chemical liquids and mixture ratios by non-destructive sensing methods are another vital research objects among the scientists. On the other hand, the detections of the transformer oil quality and machine oil quality are the main subject to monitor maintenance time and failures in power and energy industry. In addition to these determining the adulteration and distinguishing the branded and unbranded samples are another phenomena especially petroleum industry and trade.

In this point, metamaterial (MTM) based sensor structures promise solutions which meet the requirements coming with technological improvements. MTMs are materials that do not exist in natural medium and are obtained in artificial ways. They have extraordinary electromagnetic features such as simultaneously negative permittivity and permeability and so negative refraction index. It has been possible to obtain reverse Snell Law, reverse Cherenkov and Doppler effects by using these unusual features. MTMs first theoretically described by Veselago (1968) and they were called as left-handed mediums or materials. After 32 years, Pendry (2000) achieved a negative index medium to obtain perfect lens in numerical. Following year, Shelby et al. (2001) produced a negative index medium with wires and split rings and verified the theory. Thanks to these huge improvements, researchers have been interested in left-handed materials in last two decades. They have used this unusual periodic medium to investigate and improvement application fields such as perfect lenses (Pendry, 2000; Aydin et al., 2007; Chen et al., 2010), negative refraction (Foteinopoulou et al., 2003; Hoffman et al., 2007; Lezec et al., 2007), invisibility (Liu et al., 2009; Maci, 2010; Wang et al., 2013), perfect absorbers and energy harvesters (Landy et al., 2008; Sabah et al., 2014, Chen et al., 2014; Wang et al., 2015; Bağmanci et al., 2018; Karaaslan et al., 2018; Muhammad et al., 2018), polarization converters (Cong et al., 2013; Zhu et al., 2013; Altintas et al., 2017,Wang et al., 2018), antennas (Erentok and Ziolkowski, 2008; Alkurt et al., 2020), waveguides (Holloway et al., 2009), chiral surfaces providing optical activity (Rizza et al., 2015) and etc.

One of the study field in MTM based concept is sensor structures which have a resonance frequency varying with liquid and/or solid samples. MTMs are made of subwavelength resonators and they can be effectively response electromagnetic waves considering the subwavelength dimensions. The metallic loop in the resonator part of the MTM based sensor structure can be supposed as a main component and it provides strong resonance. The metallic inclusions can couple with the electric or magnetic waves at a wavelength due to their geometrical shape or orientation. Therefore, the strong current and electric field distribution can be observed in metallic loops or gaps at resonance frequency. These local regions react very sensitively to changes in their dielectric properties. Consequently, the high sensitive performance of MTM resonators promise for sensing applications with respect to dielectric characteristics of the samples.

1.2. Literature Review

In the MTM based sensor concept, many type of researches have been investigated in various application fields. Bakir et al. (2018) experimentally and numerically suggested chiral MTM sensor to achieve the two different types of sensor applications which are liquid chemical and fuel adulteration applications. Soffiatti et al. (2018) proposed a MTM based sensor structure to determine the dielectric characterization of liquid samples at microwave. A MTM absorber based microfluidic sensor structure has been studied by Hu et al. (2016) at terahertz regime for label-free refractive index sensing. Ebrahimi et al. (2014) proposed a MTM based U-shaped structure as rotation sensor in a wide dynamic range. Shih et al. (2017) experimentally demonstrate a microfluidic MTM sensor for selective trapping and remote sensing of microparticles. Abdulkarim et al. (2019) proposed a MTM absorber based swastika shaped sensor structure to detect of the liquid chemicals depending on their electrical characteristics.

The sensor characterization and some application studies such as humidity, pressure and thickness sensing are realized by Akgol et al. (2017) and Bakir et al. (2018) at X band frequency regime. These studies use the waveguide measurement technique with proper waveguide adapter and sample holder. Some researchers focus on the detection of the difference between the authentic and inauthentic fuel samples since the fuel adulteration is a big energy and financial problem for the countries (Bakir et al., 2018; Tamer et al., 2018; Tümkaya et al., 2018). Thin film and strain sensing are also studied researched by the scientists in the thickness determination concept at terahertz and microwave regime (Melik et al., 2009; Reinhard et al., 2012; Chen et al., 2016). The other phoneme in MTM based researches is biosensing. Lee et al. (2012) and Torun et al. (2014) investigate split ring resonator based sensors to detect biomolecules. The researchers use different type of MTM based sensor structure such as 3D plasmonic crystal MTMs, plasmonic nanorod MTMs and hyperbolic MTMs to obtain ultrasensitive sensing mechanism for biosensing (Kabashin et al., 2009; Aristov et al., 2016; Sreekanth et al., 2016). Geng et al. (2017)

study a MTM biosensor integrated with microfluidics to mark the liver cancer at terahertz regime. Many microfluidic MTM based sensing researches are achieved by using transmission line methods to detect chemical liquids ratios and to characterize sensor behavior at microwave regime (Withayachumnankul et al., 2013; Ebrahimi et al., 2013; Abduljabar et al. 2014).

Albishi et al. (2017) proposed a highly sensitive MTM based sensor structure which can be detected the cracks in the metallic materials. Gargari et al. (2018) studied a wireless MTM inspired rotation sensor. Their sensing mechanism has sub milliradian resolution to measure elastic-region bending in materials such as steel. Saghati et al. (2017) improved a transmission line integrated sensor structure for dielectric spectroscopy of liquid chemicals in a wideband frequency regime both numerically and experimentally. Wu et al. (2018) implemented a rectangular complementary-ring resonator based sensor to monitor permittivity of liquids at a working frequency of 900 MHz. He et al. (2010) realized a thin film sensing application by using a tip shaped split ring resonator MTM at microwave frequency regime. Ni et al. (2017) proposed an MTM absorber based sensor structure to observe humidity of environment. Keshavarz et al. (2017) realized an ultrahigh sensitive temperature sensor structure based on graphene semiconductor MTM in terahertz (THz) frequency regime. Tumkaya et al. (2017) designed a MTM based sensor structure at X-band to discriminate authentic and inauthentic fuel samples. Tamer et al. (2018) investigated a transmission line based sensor for determining authentic and inauthentic gasoline samples. Shahmarvandi et al. (2016) implemented a CMOS MTM absorber based gas sensing. Rawat et al. (2016) studied a sensor structure which can achieve to sense the toxic and hazardous materials for human health. Sethi et al. (2018) improved a blood glucose sensing mechanism by using a photonics based MTM. Keshavarz et al. (2018) presented a novel water-based terahertz MTM and a semiconductor film to detect skin cancer.

Many studies have been realized by researchers about microwave sensors with different kinds of resonator geometry for liquid detection applications. Gordon et al. (2011) proposed metasurface consisting of metallic electric-field coupled resonators operating in S band for chemicals. Abduljabar et al. (2014) used a double split ring resonator to determine the dielectric properties of common liquids at around 3 GHz. Miyamaru et al. (2014) designed a rectangular complementary split ring resonator to achieve sensitive sensing application for glycerol-water mixtures in terahertz regime. Sadeqi et al. (2017) presented MTM on low cost and ubiquitous paper substrate by implementing an array of the circular disk for detection of dielectric properties of liquids. Chen et al. (2017) realized terahertz sensing of highly absorptive water-methanol mixtures by using asymmetric dual wire resonator. Lin (2017) achieved volatile organic solutions sensing application with complementary U-shaped resonator at terahertz regime.

One of the best known resonator geometry in MTM design is split ring. Split ring resonator (SRR) based sensor structures and their derivatives have been received very much attention among the scientific community. The determination of glucose concentration in aqueous glucose solutions has been achieved by Govind et al. (2019) via a high sensitive SRR. Yoo et al. (2016) designed a split ring cross resonator structure as a chemical sensor by injecting the liquids to the microfluidic channel. Jaruwongrungsee et al. (2012) proposed a traditional SRR integrated with a disposable flow-channel made of a transparency film for chemical discrimination. Ebrahimi et al. (2013) developed a complementary split ring resonator based sensor structure with the strong electric field and sides of the resonator producing a very sensitive area have been used as a sensing layer. Another SRR based microfluidic sensor with a micro-channel for dielectric characterization has been proposed by Withayachumnankul et al (2013). Salim and Lim (2016) improved an ethanol chemical sensor structure having complementary split-ring resonator topology. Velez et al. (2018) suggested a symmetric splitter/combiner configuration loaded with a pair of identical SRRs for dielectric characterization of liquids. Zhou et al. (2019) proposed a multi-band sensing application for dielectric properties of chemical by using a double split ring resonator.

1.3. Research Objectives and Contributions

In this thesis, sensing applications and solutions of the MTM based sensor structures have been approached in parallel with the requirements of the industry. After determining an issue, electrical characteristics of the samples have been measured and the sensor structure has been designed. All studies have been realized by comparing the numerical and experimental results. The original objectives and contributions are as follows;

- To focus on the needs of the industrial applications with a high sensitivity ratio and high durability.
- To observe the electrical characteristics of the samples used in the various sectors such as energy, iron-steel, oil refinery, railway, chemistry, and etc. at different microwave frequency bands.
- To compare electrical characteristics and environmental properties of the samples with respect to linearity.
- To obtain sensor structures which is inspired MTM type resonators designed with parametric studies for the most suitable frequency ranges.
- To evaluate the numerical and experimental studies for the MTM based sensor applications by using the samples differentiate with electrical property.
- To bring in the literature many highly sensitive sensor structures by examining the electric field and surface current distributions around the sensing layer.

1.4. Organization of the Thesis

The organization of thesis is as follows;

Chapter 1 introduces sensing technologies and needs in industry and explains MTM based sensing techniques with literature review. It also explains research objectives and contributions in substances.

Chapter 2 presents the principles and methods in the thesis study.

Chapter 3 presents (i) a transmission line integrated circular split ring resonator based sensor structure at the frequency band between 3 GHz to 5 GHz, (ii) a MTM inspired labyrinth type resonator based sensor structure for microfluidic and transformer oil quality detection applications at the operating frequency range between 4 GHz and 5 GHz, (iii) split ring resonator based microfluidic sensor structure for operating frequency reconfiguration applications and (iv) wastewater treatment applications with a double split ring resonator based sensor structure.

Chapter 4 proposes (i) permittivity and thickness sensing applications with a split meander line resonator based sensor design at X band frequency regime, (ii) presents omega shaped resonator based sensor design for four different industrial implementation at X band frequency regime and (iii) electric LC resonator type MTM based sensor structure for engine lubricant oil quality detection application.

Chapter 5 offers artificial neural network approach for detection locomotive engine lubricant quality by monitoring electrical characteristics of lubricant samples at four different frequency points.

Chapter 6 finally summarize the contributions of the proposed sensor structures and sensing techniques.

2. MATERIALS AND METHODS

In this section, the principles and methods of the thesis are explained. The applications have been realized by both numerical and experimental methods. Full wave solver finite integration technique based CST Microwave Studio simulation software and artificial neural network technique have been used as materials in the numerical methods. The LPKF E33 type CNC based prototyping machine, Agilent PNA-L type Vector Network Analyzer, Keysight 85070 coaxial type dielectric probe kit and X band waveguide with proper adapters have been employed in the experimental methods. Materials and methods have been classified into three sections which are (i) principles of sensor design, (ii) numerical methods and (iii) experimental methods.

2.1. Principles of Sensor Design

The sensor structure of an implementation should be carefully constructed by considering its application purposes. In this thesis study, two implementation techniques have been applied for the sensing studies. These are waveguide based and transmission line based implementations. The waveguide based implementations have advantages such as high sensitivity and accurate results for the samples having close electrical characteristics. On the other side, the transmission line based implementations have advantages such as low cost and easy integration to the sensor devices. After the chosen of the implementation method with respect to application areas and dielectric properties of the samples, the sensor design principles construct as illustrated in Figure 2.1.

The MTMs are the subwavelength structures. Hence, the unit cell dimension values of them must be lower than the wavelength of the center frequency of operating band. The resonator parts of the proposed sensor structures have been designed this technical properties of the MTMs. In the numerical designs, it is paid attention that the highest dimension value of the resonators must be lower than the quarter wavelength value of the center frequency to provide minimum return power loss.

Another important point is to select operating frequency ranges of the proposed sensor structures. This choice is depend on the variations of the frequency dependent electrical properties of the samples. Therefore, it is chosen an operating frequency band which is observed the greatest electrical property difference between the samples.

The first step while designing a sensor structure is chosen a resonator geometry selection. The split gaps interacted with the metallic lines are the key point while the design a MTM based sensor structure. The determining the resonance frequency of the sensor structure depends on these parts of the resonator since the split gaps generate a capacitive effects and the lines has inductive effects. Moreover, these parts, especially capacitive parts can be easily manipulated with the samples with frequency dependent electrical characteristic by creating a sensing layer inside them. Hence, the resonance frequency changes have been observed clearly with the variations of capacitive or inductive parts originated from the samples.

The omega-shaped resonator which is applied in the section 4.2 is selected as an example in Figure 2.1(a). The resonator dimension of the structure must be determined as parametric values that can be changed. Purpose of selecting the dimension values as parametric symbols is that specifying the optimum resonance frequency point in an operating frequency range by varying these parameters.

The sensor configuration of the sensor structure should be examined in detail given in Figure 2.1(b). The inductive lines, capacitive gaps, sensing layer thickness and location must be determined since these properties are very crucial for the equivalent circuit diagram which determines the optimum resonance frequency point. The adjusted sensing layer thickness must be compatible with the experimental conditions. In addition, chosen dielectric layer properties and resonator material type should also have the same characteristics with the practical application.

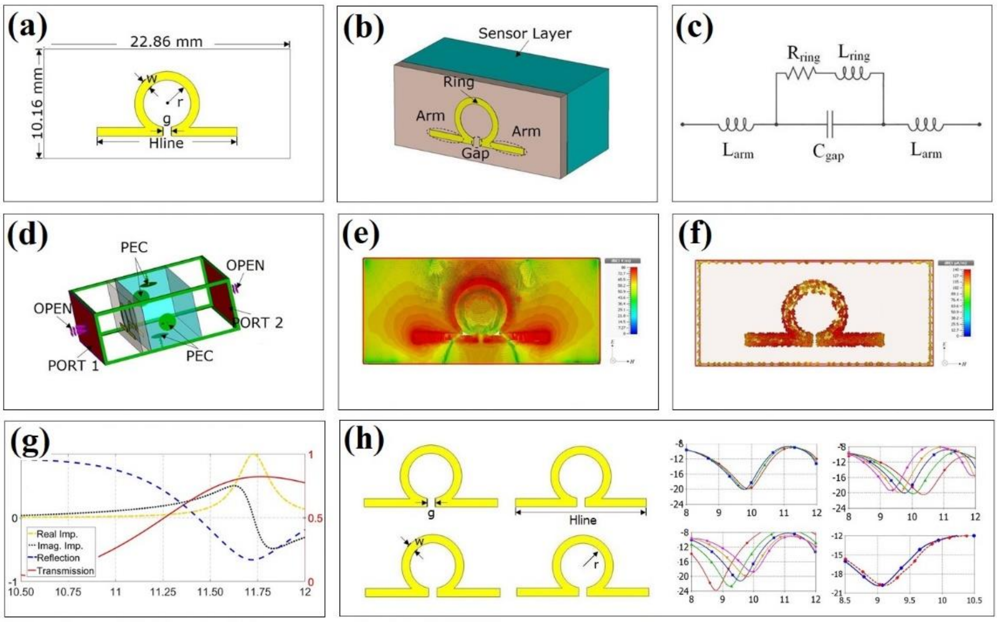

Figure 2.1. Design steps for a sensor structure; (a) resonator selection, (b) sensor configuration, (c) equivalent circuit diagram, (d) numerical setup configuration, (e) electric field distribution, (f) surface current distribution, (g) impedance matching analysis, and (h) parametric studies

To understand physical and working mechanism, an equivalent circuit diagram examination is another important phase as illustrated in Figure 2.1(c). It is obtained by finding inductive, resistive, and capacitive parts of the sensor structure. The geometry shape of the resonator, applied frequency, and location of the sensing layer determines the values of these passive circuit elements. Hence, total capacitive and inductive values are observed. It is investigated how is the resonance frequency points affected by these values.

The proposed sensor structures has an equivalent circuit diagram which behaves like a simple RLC circuit shown in Figure 2.1(c). The sensing layer which can be varied from the samples having different electrical properties also creates additional capacitive effect as C_{sens}. The permittivity of the sample placed on the sensing layer can be expressed as;

$$\varepsilon_{samp} = \varepsilon'_{samp} - j\varepsilon''_{samp} \tag{2.1}$$

Hence the total capacitance (C_t) of the proposed structure is a function of the dielectric constant (ε'_{samp}) and dielectric loss ($j\varepsilon''_{samp}$) of the sample loaded in the sensing layer.

$$C_t = F_c(\varepsilon'_{samp}, \varepsilon''_{samp}) \tag{2.2}$$

The total capacitance (C_t) of the sensor can be expressed as;

$$C_t = C_0 + C_{eq} + \varepsilon_{samp}C_{sens} \tag{2.3}$$

where C_0 is the capacitive effects which are stem from the environmental space, C_{eq} is the equivalent capacitance value of the RLC circuit, and the $\varepsilon_{samp}C_{sens}$ denotes the capacitive effect of the sensing layer.

The total inductance value of the sensor structures can be expressed as;

$$L_t = L_{eq} + M \tag{2.4}$$

where L_{eq} is the equivalent inductance value of the RLC circuit and M is the mutual inductance occurred between the resonator and transmission lines. M is only used in the sensor structure designed with transmission line implementation. It is negligible in the other applications since the electromagnetic waves is applied via free space, not with the transmission line ($M = 0$ in waveguide implementations). The mutual inductance (M) can be defined as;

$$M = k\sqrt{L_{eq}L_s} \tag{2.5}$$

where k is the coefficient of coupling which is the fraction of magnetic flux that links in one coil to another ($0 \le k \le 1$). L_s is the inductance of the transmission line.

The total resistance of the sensor structures is defined as (R_t). Most of the applied power is spent on this part.

The resonance frequency (f_0) of the structure can be written as;

$$f_0 = \frac{1}{2\pi\sqrt{L_t C_t}} \tag{2.6}$$

The sensing ability of the structure can be easily observed by the resonance frequency shifts.

The equivalent impedance of the sensor can be written as;

$$Z_{eq}(\omega) = R_t + j\omega L_t + \frac{1}{j\omega C_t} \tag{2.7}$$

The impedance of the free space is defined as;

$$Z_0 = \frac{\mu_0}{\varepsilon_0} = 377\,\Omega \tag{2.8}$$

The reflection calculation between these two mediums can be represented as;

$$R(\omega) = \frac{Z_{eq}(\omega) - Z_0}{Z_{eq}(\omega) + Z_0} \tag{2.9}$$

The numerical setup configuration as shown in Figure 2.1(d) must be created to observe electric field and surface current distributions, impedance matching analysis and parametric studies. The waveguide or discrete ports and their reference planes should be located correctly. The boundary conditions and the operating frequency range must be the arranged with the same conditions as the experimental works.

To observe sensitivity of the sensor against the electrical changes in sensing layer, electric field and surface current distributions should be examined as illustrated in Figure 2.1(e) and (f). In addition to this, the impedance matching analysis with respect to real/imaginary impedance and transmission/reflection coefficient should be studied for interaction between incident wave and resonator, especially in waveguide implementations as demonstrated in Figure 2.1(g). The parametric study must be realized to obtain desired resonance frequency point and transmission or reflection coefficient in working frequency range as shown in Figure 2.1(h).

Two types of substrate material has been used in sensor designs. One of them is FR4 type material that has a relative permittivity of 4.3, loss tangent of 0.02 and thickness of 1.6 mm. The other selected substrate is Arlon AD350 type dielectric material with a thickness, relative permittivity, and loss tangent values of 0.78 mm, 3.5 and 0.003, respectively. The metallic layers as resonator part and ground plane consists of copper type metal having a conductivity of 5.80001×10^7 S / m. Moreover, various Arlon and Rogers types of dielectric material has been used in the sensor studies to observe sensing abilities of the proposed sensor structures. These types of materials has been selected as different dielectric properties and thickness values which are tabulated in related sections.

2.2. Numerical Methods

2.2.1. CST Microwave Studio Simulation Software

The sensor structure designs, resonance frequency examination, operating frequency determination, and the other numerical applications have been realized by using CST Microwave Studio Simulation Program. The simulation software gives multiple electromagnetic (EM) simulation solvers (frequency domain, time domain, and eigenmode etc.) which use the techniques such as finite element method (FEM), finite integration technique (FIT) and transmission line matrix method (TLM).

Eigenmode solver is used for resonant filter structures, and high-Q particle accelerator cavities, and slow wave structures such as travelling wave tubes. It also suitable for sensitivity analysis. Application areas for this solver can be presented as filters, cavities and MTMs/periodic structures.

Time domain solver is based on both FIT and TLM. This solver is suitable for extremely large, complex and detail simulations. Application areas for this solver can be listed as high-frequency applications using medium or large models, transient effects and 3D electronics.

Frequency domain solver is generally used for multipurpose 3D full wave applications. It is based on FEM and can calculate all ports at the same time. Application areas for this solver can be presented as general high-frequency applications using small or medium sized models, resonant structures, multi-port systems, 3D electronics.

In the numerical studies, some optimization techniques which is supported by CST Microwave Studio simulation software have been used. Hence it is founded that optimum design parameters to achieve fulfill a certain aim. It is also adapted material properties to fit measured data. The optimization techniques which used in the sensing studies can be listed as (i) genetic algorithm, (ii) particle swarm optimization, and (iii) interpolated quasi newton. They are suitable for complex problem domains, computationally demanding models and models with many parameters.

2.2.2. Artificial Neural Network Tool

The ANN method is used in Chapter 5 as a novel approach for engine lubrication quality determination. The method is studied to observe the correlation between the electrical characteristics and chemical properties of the lube oil samples. ANN is developed with the aim of gaining knowledge and experience through learning from the characteristics of the human brain. The working principle is based on the parallel information architecture situated in the brain neuron systems.

The back propagation network (Haykin, 1998) which is the most popular among the ANN phenomena is used for the thesis study. The network consists of different interconnected layers which are hidden layer (having at least 2 layers), input and output layers. These three layers called feed forward neural network architecture are interconnected with the weights and between the layers of neurons as shown in Figure 2.2. Calculated weight values are gradually controlled and corrected during the training process by comparing predicted outputs with observed outputs. These estimated values propagates back for any errors (right to left) to obtain proper weight configuration (Kisi, 2007).

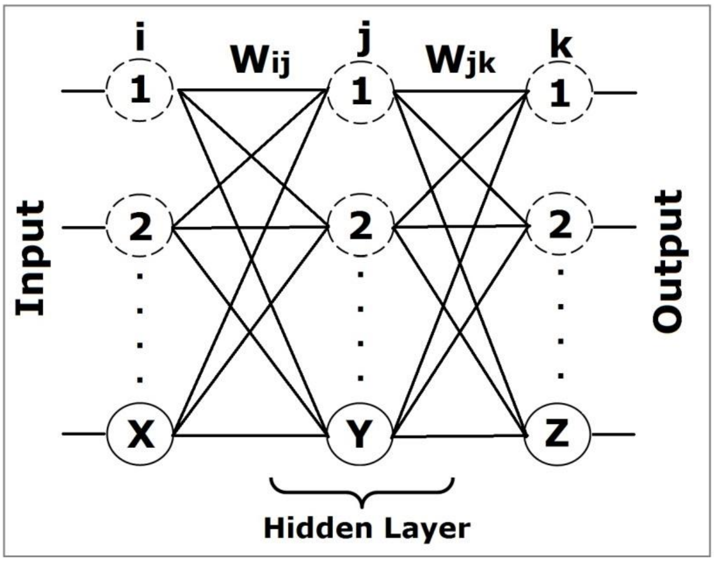

Figure 2.2. A three layer feed forward neural network architecture

Quasi-Newton backpropagation algorithm is applied to monitor linear relationship between a dependent variable with independent variables. The dependent variable represents dielectric constant or dielectric loss and the independent variables represent particles in parts per million (ppm) inside the lube oil sample.

The training and testing data sets are applied to the ANN to observe regression characteristics. For each specified frequency point, MSE, MAE and MAPE is calculated as below;

$$MSE = \frac{1}{N}\left[\sum_{i=1}^{N} Yi_{observed} - Yi_{forecast}\right]^2 \tag{2.10}$$

$$MAE = \frac{1}{N}\left|\sum_{i=1}^{N} Yi_{observed} - Yi_{forecast}\right| \tag{2.11}$$

$$MAPE = \frac{1}{N}\left|\sum_{i=1}^{N}\frac{Yi_{observed} - Yi_{forecast}}{Yi_{observed}}\right| \times 100 \qquad (2.12)$$

where N and Y denote the number of data sets and dielectric constant or dielectric loss values, respectively. It can be noted that the method is to be convenient to minimize the sum of squares between differences of observed and forecast values.

2.3. Experimental Methods

2.3.1. LPKF E33 Prototyping Machine

In the manufacturing process of the sensor structure, CNC based LPKF E33 type prototyping machine has been used as shown in Figure 2.3. The technical drawing of the sensor structures are taken by CST Microwave Studio simulation program in dxf file format. The drawing files are then imported to the CircuitPro which is a PCB prototyping machine software program and the dielectric substrate having double sided or single sided copper metal is located in the machine platform by making necessary placement adjustments. The spiral drill tool is then used to obtain sensing layers gap, after milling and plotting processes. Highly sensitive plotter tools are used in the fabrication process of the architecture of the resonators which are in the micro level.

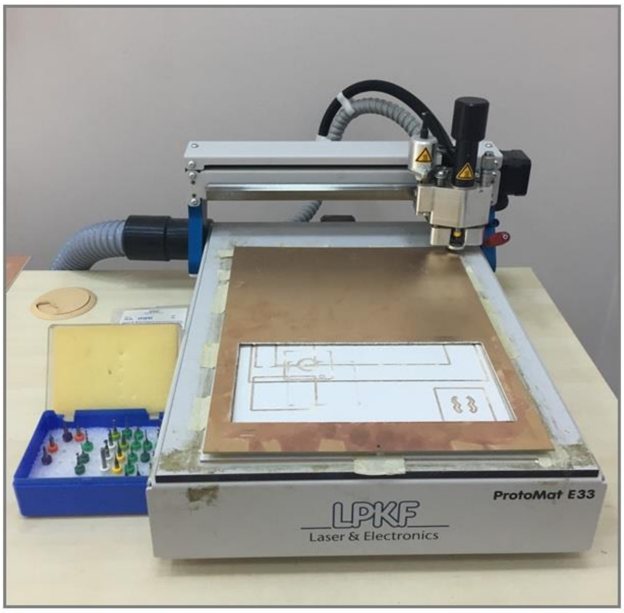

Figure 2.3. CNC based LPKF Protomat E33 PCB prototyping machine

Prototyping machine has milling and drilling process for both single- and double-sided circuit boards. In the production, different kinds dielectric layers (such as flame retardant 4 (FR4), Arlon and Rogers) covered by copper type metal with various thicknesses have been used. All studied sensor structures have been produced by using this CNC based PCB prototyping machine as illustrated Figure 2.3. The sensor structure have been obtained by milling the copper surfaces expect the resonator area. PCB prototyping machine has a resolution of less than 1 μm and a repeatability of ±5 μm for circuit board plotting process. Although it meets the requirements for many sensor structure, some minor fabrication errors have been occurred in the manufacturing process especially in high frequency applications.

2.3.2. Agilent PNA-L VNA

Experimental studies of the manufactured sensors are performed by the Agilent PNA-L type VNA which is capable of operating up to 43.5 GHz as demonstrated in Figure 2.4. Before the measurement, VNA is calibrated properly to the reference values using the proper calibration kit by applying open circuit, short circuit and 50 Ω load connectors without connecting the sensor structure. Two coaxial test cables are connected to the sensor structure and transmission and/or reflection coefficients are monitored. To ensure the accuracy of the calibration, 50 Ω load are connected to the testing cables and the corresponding results are checked with the simulation results.

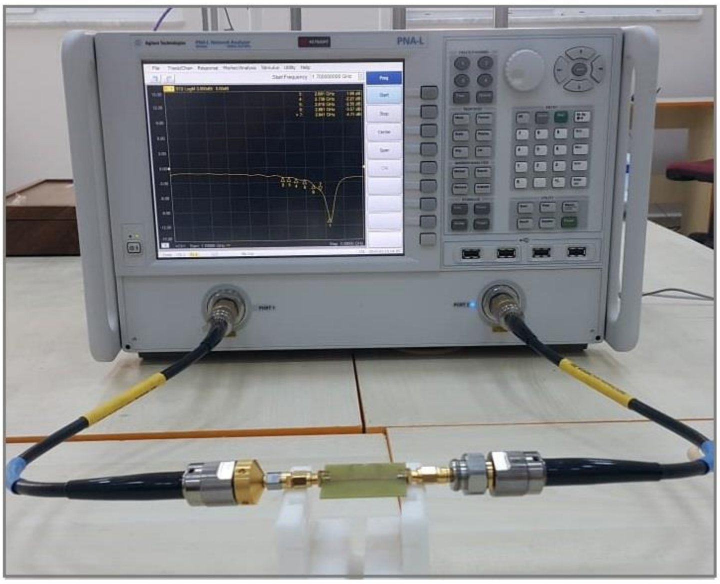

Figure 2.4. Agilent PNA-L type VNA with two coaxial cables

2.3.3. Permittivity Measurement Method

In this section, dielectric values are analyzed for lube oil samples at various frequency points. Every medium in the nature has electrical constitutive parameters such as permittivity, permeability and conductivity. Permittivity is one of the fundamental electrical properties of the materials existing in the environment. The dielectric constant of a material indicates the ability to store energy compared to free space. It can be changed with different circumstances such as frequency, temperature, mixture, orientation and pressure of the material [Mumby, 1989; Zeng et al., 2010; Zhao et al., 2016; Jafari and Ahmadi-Shokouh, 2018]. Permittivity is related with the external electric field and has a real and imaginary part;

$$k = \frac{\varepsilon}{\varepsilon_0}\varepsilon_r = \varepsilon_r' - j\varepsilon_r'' \tag{2.13}$$

where *k* is the dielectric constant and it is equivalent to ε_r which is called relative permittivity. Real part of dielectric constant (ε_r') shows energy storage capability of a material exposed to an external electric field. Imaginary part of dielectric constant (ε_r'') indicates loss factor and it is a measure of loss of a material in an electric field. ε_r'' is originated from both dielectric loss and conductivity.

The relative energy dissipation of a material named as loss tangent $(\tan\delta)$ is obtained by dividing by the energy lost to the stored energy.

$$\tan\delta = \frac{\varepsilon_r''}{\varepsilon_r'} = D = \frac{1}{Q} = \frac{Energy\ Lost}{Energy\ Stored} \tag{2.14}$$

D is dissipation and Q denotes quality factor or Q-factor. Loss tangent or $(\tan\delta)$ is called as dissipation factor.

In the measurement process of electrical properties, an open-ended coaxial dielectric probe (performance probe type) connected to Agilent PNA-L vector network analyzer (VNA) and corresponding software are used for dielectric constant measurement of samples. Many dielectric measurement methods such as a waveguide, free space or ring resonator methods exist. However, in this study, the coaxial probe method has been selected to measure liquid or solid samples since this method provides faster and easier results than other methods when considering the numbers of samples. The researches present the formulas of permittivity by coaxial probe measurement methods (Blackham et al., 1997; Wang et al., 1998). The dielectric probe is capable of measuring scattering parameters (S-parameters) for solids, semisolids (powder) and liquids. Before the measurement process, it must be calibrated by the way of air, pure water having 25°C temperature and special calibration kit for short circuit. As a second step, the probe-end is directly immersed to the liquids or touched solids (or powders) and the signal adjusted to a desired frequency range is applied to the sample. Reflected signal (S_{11}) is then received and calculated as a function of permittivity via VNA as illustrated in Figure 2.5(a). The experimental setup with the dielectric probe and VNA is shown in Figure 2.5(b).

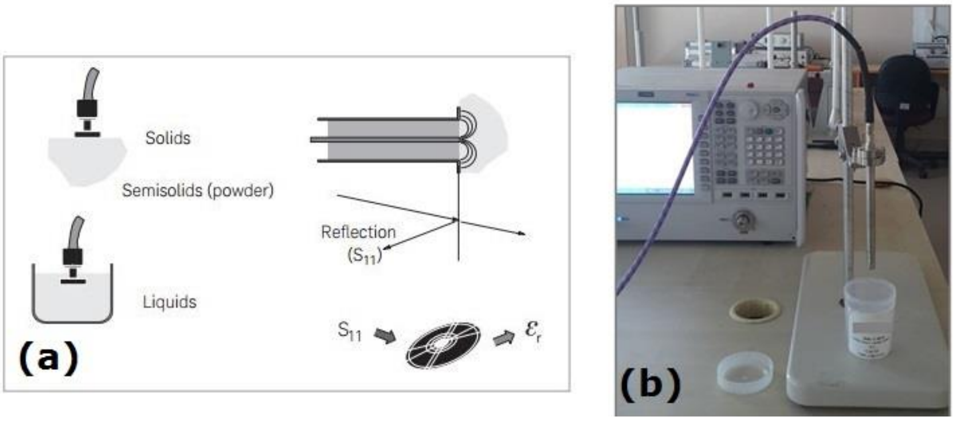

Figure 2.5. (a) Coaxial probe method and (b) dielectric constant measurement setup

The performance probe withstands between -40°C to 200°C temperature range which allows measurement versus frequency and temperature. The probe is very useful for food, medical and chemical industries as it has a slim design that integrates rugged, high temperature and frequency performance. Furthermore, the measurement method provides to the user many advantages such as broadband frequency range, non-destructive solution and low-loss resolution.

2.3.4. X Band Waveguide

In the sensor applications which have been used operating frequency range between 8 GHz and 12 GHz, X band waveguide implementations have been adjusted. Experimental studies are realized using an X-band waveguide, two WR90 waveguide adapter and a sample holder as illustrated in Figure 2.6. The sample holder with a depth of 10 mm is loaded with liquid or solid samples at each measurement step and it is placed to the front side of the waveguide. The fabricated sensor structure has been embedded to the waveguide adapter coincided with the sample. After the configuration, the waveguide has been connected to PNA-L Agilent VNA with a frequency range between 10 MHz and 43.5 GHz as shown in Figure 2.4. Before the measurements, the frequency range has been arranged between 8 GHz to 12 GHz.

In the X band waveguide based implementations, the dimensions of the sensor structures has been adjusted as 22.86 mm and 10.16 mm which corresponds the exact dimensions of an X band waveguide. The aim of these types of applications is to embedding the sensor structures and sample holders to the waveguide along with a closed cavity which is not affected by the environmental conditions. Hence, the measurement results are more reliable and precise with this technique.

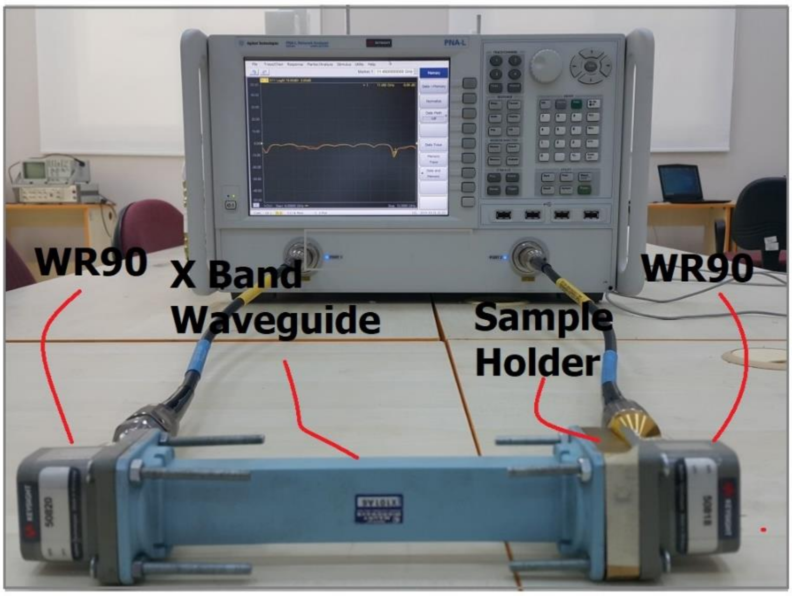

Figure 2.6. X band waveguide implementation with Agilent PNA-L VNA

3. APPLICATIONS WITH TRANSMISSION LINE TECHNIQUE

In this section, transmission line integrated sensor structures are examined and they are tested in various industrial samples. These samples are placed into the cavities in capacitive regions of the structures. The transmitted or reflected power has been observed with respect to electrical characteristics of the samples via transmission lines. In this way, it has been detected how the samples affect the electrical responses of the sensor structures.

Four different sensor applications which are (i) fluid, strain and rotation sensing, (ii) chemical liquid and transformer oil quality detection, (iii) operating frequency configuration, and (iv) wastewater quality sensing have been studied in this chapter. The sensor structures have been tested with various samples such as ethanol, metallic rod, transformer oil, different liquid chemicals, wastewater, and etc.

3.1. Fluid, Strain and Rotation Sensing Applications

In this part, fluid strain and rotation sensing applications have been realized by using a CSRR numerically and experimentally. The proposed structure consists of basic SRR architecture and it is integrated on a transmission line by matching half of outer edge to monitor transmitted power from a port to other.

3.1.1. Design and Theory of the CSRR based Sensor

CSRR based sensor structure consists of a three layers which can be expressed as bottom layer or ground plane, subtract layer and top layer or resonator layer. A transmission line is surrounded on the circular split ring resonator as shown in Figure 3.1(a). A radial space is placed into the middle of the circular resonator used as sensing layer. The magnetic coupling has been occurred between the transmission line and the resonator part of the structure. The resultant electrical changes in sensing layer has been monitored by transmitted power on transmission line.

The operating frequency of the CSRR based sensor has been adjusted between 3 GHz and 5 GHz since the permittivity difference for samples studied in this section is monitored at this frequency range. The dimensions of the resonator given in Table 3.1 have been obtained by considering the quarter wavelength of the center frequency.

The bottom layer of the proposed structure is metallic plate as ground plane. FR4 type material has been chosen as subtract layer. The top layer as resonator part consists of copper type metal. The dimensions of the resonator part illustrated in Figure 3.1(a) have been tabulated in Table 3.1. The dimension parameters can be defined as outer radius of main ring (*r1*), inner radius of main ring (*r2*), diameter of sensing ring (*rd*), radius of inner and outer resonator ring (*sr2*, *sr1*) and gap on resonator ring (*rg*)

Table 3.1. Dimensions of CSRR

r1	***r2***	***sr1***	***sr2***	***rg***	***rd***
7.0 mm	5.0 mm	4.35 mm	3.85 mm	2.0 mm	7.30 mm

Quasi TEM mode of wave propagation is stimulated by the end of the microstrip line and the equivalent circuit model of the structure has been examined in Figure 3.1(b). C_p and R_p present the equivalent capacitance and resistance values of the resonator, respectively.

Dielectric properties of the samples can be presented as Eq. (2.1). Therefore, the total capacitance of the sensor structure (C_t) is depend on the dielectric constant and dielectric loss of the sample given Eq. (2.2). It is expressed as Eq. (2.3) by replacing equivalent capacitance variable with C_p.

A mutual inductance can be observed between L_p and L_s. L_p is the equivalent inductance of the resonator and L_s is the inductance of the transmission line. The mutual inductance (M) is calculated by the Eq. (2.5) and total inductance (L_t) is estimated by Eq. (2.4).

The resonance frequency (f_0) of the CSRR is then described by using total capacitance (C_t) and inductance (L_t) in Eq. (2.6).

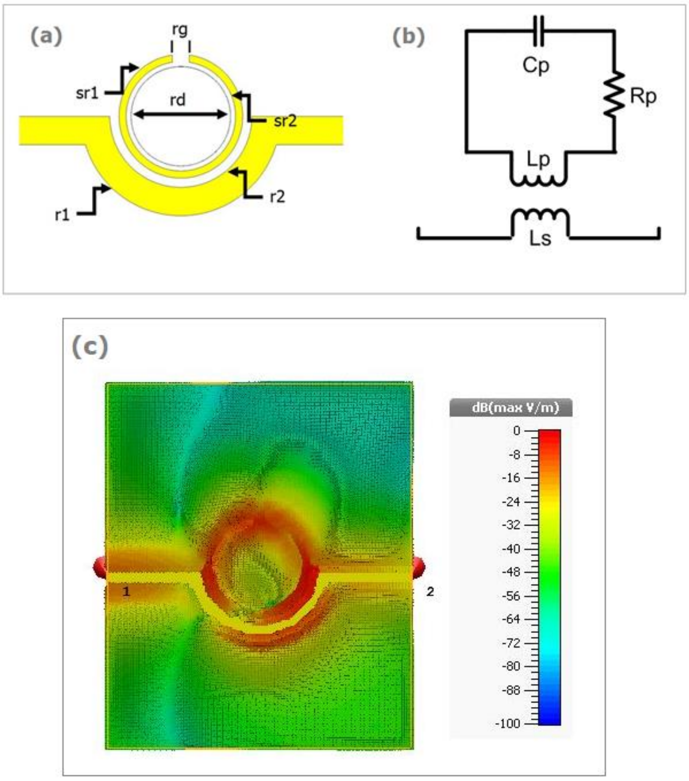

Figure 3.1. (a) Geometrical dimensions, (b) equivalent circuit diagram and (c) electric field distribution of the proposed MTMs based sensor

The electric field distribution of the suggested sensor structure is given in dB in Figure 3.1(c). The electric field is distributed around the resonator part and it is focused on especially circular split ring resonator. Since the sensing layer has been surrounded by the circular split ring resonator, the electric field distribution is effected any electrical changes in sensing layer. The samples placing on the sensing layer can have different dielectric characteristics. Hence they have huge impact on the electrical filed distribution around the sensing layer and CSRR. This electrical changes under different circumstances of the sensing layer play key role on the transmitted power through the transmission line.

The manufactured sensor structure and the simulation model have been demonstrated in Figure 3.2. The front and rear views of the sensor produced using a CNC based machine can be seen in Figure 3.2(a) and (b), respectively. The sensor structure has been produced with the same dimensions and similar design idea as simulation model given in Figure 3.2(c). The FR4 type substrate with 1.6 mm thickness and same dielectric characteristics with simulated one has been chosen as dielectric material. Two 50 ohm SMA type connectors have been soldered both end sides of the transmission line. The impedance of the ports are compatible with cables of the VNA. The sensing layer has been created by drilling middle of the CSRR with same dimension with simulated model.

The experimental setup is illustrated in Figure 3.3. After the proper calibration process of the VNA, the sensor structure has been connected to the VNA by both ports. A silicon based sample holder has been used for liquid samples and it is directly placed to sensing layer. Transmission and reflection coefficients, phase differences and frequency shifts are then monitored for different samples at operating frequency range of the sensor.

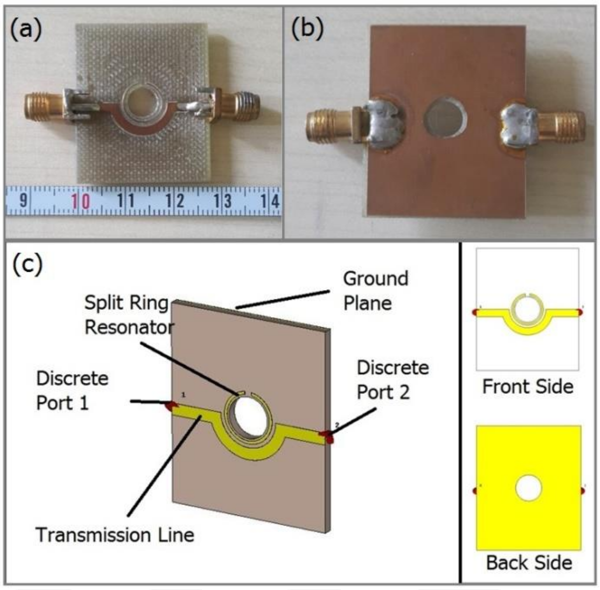

Figure 3.2. (a) Front view of the manufactured sensor, (b) Back view of the manufactured sensor, (c) Simulation model of the sensor structure

Figure 3.3. Experimental setup view with proposed sensor structure

The experimental and numerical results of the transmission coefficient are drawn together in the same graph for comparison purposes and are given in Figure 3.4. The results have been examined by letting the sensing layer empty. The operating frequency range is between 3 GHz and 5 GHz. The resonance frequency point which has lowest transmitted power is 3.912 GHz for numerical study and it is 4.078 GHz for experimental study. The transmission coefficient in dB at resonance frequency is -15 dB for numerical study and it is -8 dB for experimental study.

Although there is a minor difference between numerical and experimental results, they are in a good agreement. This small diversity is originated form the manufacturing errors and soldering effects. The low milling sensitivity of the CNC based PCB manufacturing machine has been caused dimension errors for the resonator parts. This affect to the electric field distribution and transmitted power levels. Besides that, the frequency shifts between measured and simulated result arise from soldering which can manipulate the impedance of the transmission line. In addition, there are many side effects (such as test cable, connectors, adapters etc.) for this slight difference to occur.

There is a difference between the simulation and measurement results for transmitted power at resonance frequencies as illustrated in Figure 3.4. It can be explained as Q-factor deviations between the results. Q-factor for electrical systems includes capacitors and inductors is expressed in Eq. (2.14). Overall stored energy is total of the stored energy in capacitors and inductors and the overall energy loss is observed in resistors. In the experimental studies, Q-factor value is lower than the numerical studies as shown in Figure 3.4. This difference is originated from non-perfect laboratory conditions, calibration errors and especially production and soldering process. Since the circuit elements such as capacitor, inductor, and resistor in the equivalent circuit diagram in Figure 3.1(b) has been determined by the geometry of the resonator, even minimum errors and low sensitivity in the production process can affect to Q factor dramatically.

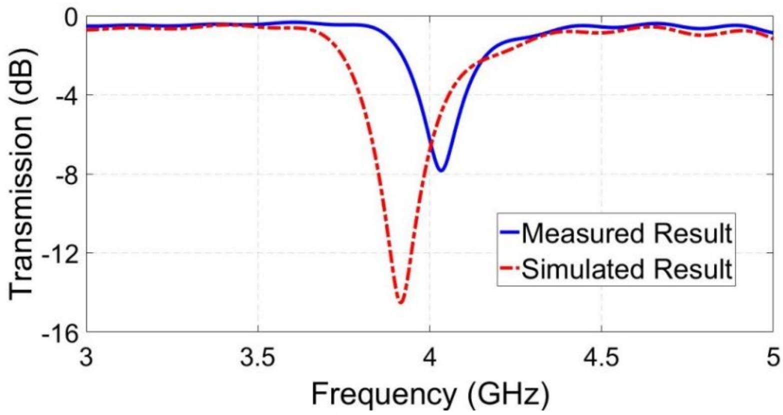

Figure 3.4. Simulated and measured transmission coefficient results for sensor structure without any sample

3.1.2. Fluid Sensing Application

In this section, the CSRR based sensor structure has been tested for detection ethanol water ratio as a fluid sensing application.

In first step, the electrical characteristics of ethanol water mixtures have been measured by using the dielectric probe connected to VNA as shown in Figure 3.5. The measurements are performed between 3 GHz and 5 GHz which correspond to operating frequency range of the sensor.

The mixtures have been prepared by increasing ethanol content 10% in each phase. Hence, eleven samples have been obtained and their dielectric constant and dielectric loss factor values are measured. These electrical properties of the mixture samples have been plotted as a function of frequency between 3 GHz – 5 GHz in Figure 3.6.

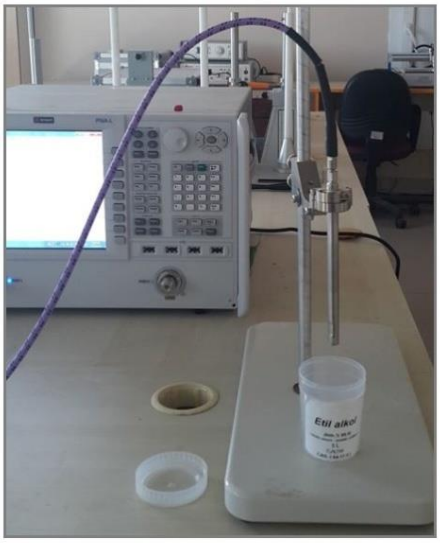

Figure 3.5. The measurement setup for electrical characteristics of ethanol water mixtures

Dielectric constant values decrease almost linearly due to the 10% increase in the ethanol content of the mixture as seen in Figure 3.6(a). The dielectric constant of pure water is approximately level of 80 and the dielectric constant of pure ethanol is 12 at between 3 GHz – 5 GHz of frequency band. In the same manner, The dielectric loss factor values is tend to decrease for each 10 % increment of ethanol content in the ethanol water mixtures as shown in Figure 3.6(a). The measurement results for dielectric constant and dielectric loss factor of ethanol water mixtures are in harmony with literature even though it is observed close values for the dielectric loss factor results of the mixture samples having 70%, 80% and 90% ethanol content (Withayachumnankul et al., 2013; Ebrahimi et al., 2013; Jaruwongrungsee et al., 2012).

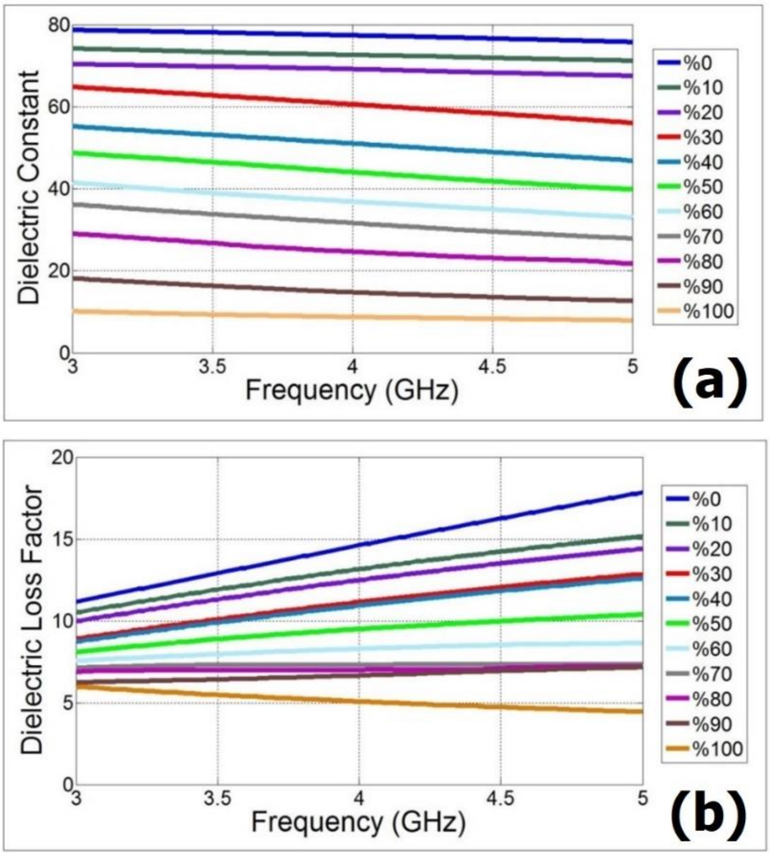

Figure 3.6. (a) Dielectric constant and (b) dielectric loss factor values for ethanol water mixture samples

The dielectric constant (ε'), dielectric loss (ε'') and loss tangent (ε''/ε') values at resonance frequency of sensor structure (4.078 GHz) have been tabulated in Table 3.2. The results are obtained at room temperature and the pure water and ethanol (98.9%) are used in the mixture samples. Dielectric constant and loss values have been linearly decreased when the ethanol volume is increased. The other important parameter loss tangent value which effect the energy loss in applications is also shown in Table 3.2. This value has been ascend due to increase ethanol content. Hence, It can be said that the ethanol content in mixtures have a huge impact on the energy loss in the application.

Table 3.2. Dielectric and loss tangent values depending on the ethanol content at resonance frequency of sensor (4.078 GHz)

Ethanol Content (%)	**ε'**	**ε''**	**Loss Tangent**
0	78,64	11,34	0,144
10	73,15	11,17	0,153
20	69,42	11,03	0,159
30	63,44	10,74	0,169
40	52,85	10,03	0,190
50	45,03	9,27	0,206
60	37,66	8,16	0,217
70	32,49	7,32	0,225
80	25,35	6,99	0,276
90	15,34	6,56	0,428
100	8,96	5,22	0,583

The fluid sensing application has been achieved for 0%, 20%, 40%, 50%, 60%, 80% and 100% of ethanol content in ethanol water mixture both numerically and experimentally. The results are shown in Figure 3.7 at between the frequencies of 3.8 GHz and 4.2 GHz. In this figure, the transmission coefficients is exhibited in dB. The focus point in the results is how much the resonance frequencies shifts from step by step. In the numerical studies, the resonance frequency for 0% ethanol content is observed at 3.987 GHz as shown in Figure 3.7(a). It is observed at 4.052 GHz for 100% of ethanol volume. 20% increment of ethanol volume in the ethanol water mixture is shifted the resonance frequency to 3.911 GHz. The resonance frequency points is increasingly reach from 3.987 GHz to 4.052 GHz. The increment ratio at the resonance frequency values is almost linear in numerical. The experimental studies have been realized for the same ethanol content in the mixture samples at between the 3.8 GHz and 4.2 GHz as plotted in Figure 3.7(b). The resonance frequency points are monitored as 4.024 GHz, 4.029 GHz, 4.033 GHz, 4.035 GHz, 4.038 GHz, 4.043 GHz and 4.048 GHz for 0 %, 20 %, 40 %, 50 %, 60 %, 80 % and 100 % of ethanol in the mixture, respectively. The transmission coefficient ratios for numerical and experimental studies have been observed at the same level as shown in Figure 3.7. When comparing the experimental and numerical studies, the results validate linear changes at the resonance frequency. Hence, it can be concluded that the CSRR based sensor structure can be efficiently used as liquid ratio detection sensor in the mixtures.

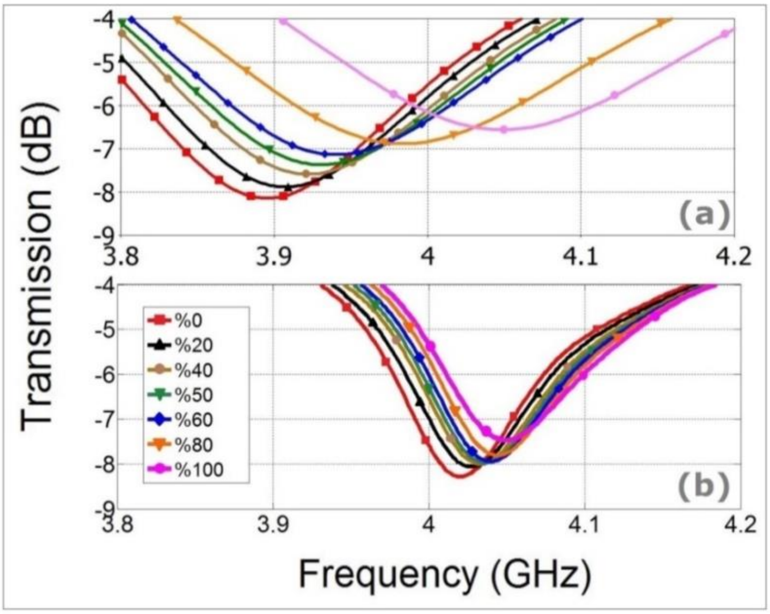

Figure 3.7. Transmission coefficient results for liquid sensing application; (a) numerical and (b) experimental studies

The changes in resonance frequency against dielectric constant have been plotted in Figure 3.8 by using numerical transmission coefficient results. This figure shows while the dielectric constant of the sample is decreasing, resonance frequency of the sensor is increasing. It can be concluded that resonance frequency of the sensor structure inversely proportional to the dielectric constant of the samples. The variation in both curves seen in the figure is adequate to determine the ethanol content in the mixture.

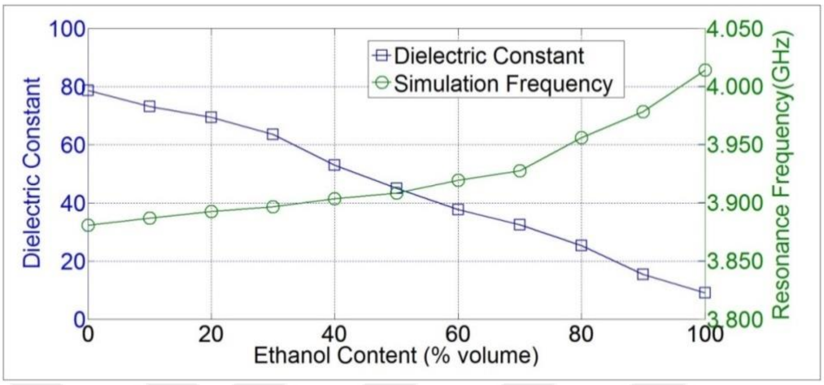

Figure 3.8. Experimental resonance frequency and dielectric constant results depending on ethanol content

3.1.3. Strain Sensing Application

The ability of the strain sensing of the CSRR based sensor structure is investigated in this section. The used method for this application is non-destructive. Hence, it can be effectively used in many industrial applications. The iron rods with different thicknesses have been used as samples. Metallic samples placed to the sensing layer will be interacted with the CSRR part of the sensor structure. The coupling will be occurred between these metallic parts. The electrical coupling is caused by capacitive gap between these parts. The capacitive effect is depends on the thickness of the metallic rod samples in this application. Hence, the changes in the resonance frequency of the sensor structure can be easily observed by applying Eq. (2.6).

The numerical and experimental studies have been realized for the sample thicknesses of 1.83 mm, 2.51 mm, 3.47 mm, 4.05 mm and 4.90 mm, respectively as shown in Figure 3.9. The transmission ratios in dB is observed as about -15 dB for numerical studies and -8 dB for experimental studies. The resonance frequency point has been obtained 4.006 GHz for 1.83 mm thickness of sample in numerical studies as illustrated in Figure 3.9(a). The resonance frequency points have regularly increased by the increment of the thickness of the rod samples. In the same manner, the experimental results show the same behavior as shown in Figure 3.9(b). The same relation between the resonance frequency and sample thickness has been observed at between 3.9 GHz and 4.3 GHz in experimental.

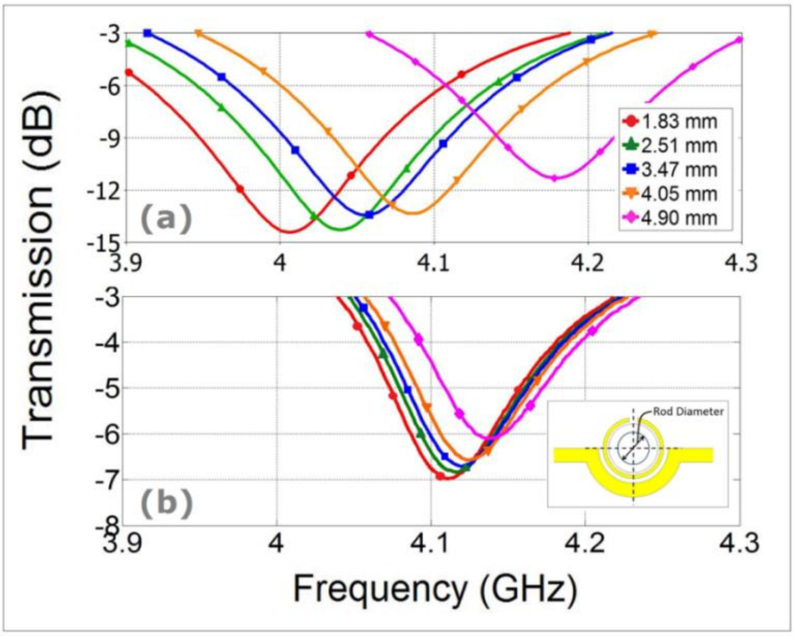

Figure 3.9. Transmission coefficient results for strain sensing application; (a) numerical and (b) experimental studies

To observe the resonance frequency relation with rod sample diameter, the experimental and numerical resonance frequency point results have been tabulated in Table 3.3. As can be seen in Table 3.3, increment coefficient is the same for both simulation and measurement results although the measurement results have obtained in a narrow frequency band than the simulation results.

Table 3.3. Rod sample thicknesses and corresponding simulated and measured resonance frequencies

Thickness (mm)	Simulated Resonance Frequency (GHz)	Measured Resonance Frequency (GHz)
1.83	4.006	4.111
2.51	4.039	4.117
3.47	4.056	4.122
4.05	4.087	4.129
4.90	4.181	4.141

The linearity graphs both simulation and measurement have been given in Figure 3.10 by using in Table 3.3. The slopes of the measurement and simulation resonance frequency vs. rod diameter are close each other and they have approximately linear characteristics. This linear response provides the sensitive and high precision results for strain sensing applications. Therefore, it is concluded that the CSRR based sensor structure is capable for sensing diameter or thickness of iron or any metallic rod. Besides, it can also be used to measure the thickness of hot metals in the fabrication stage of iron-steel industry.

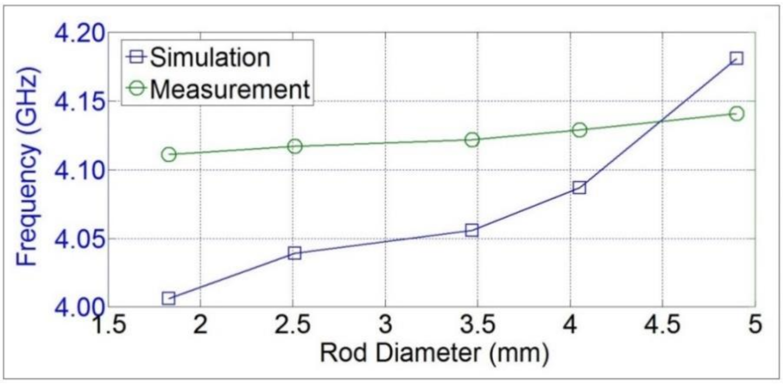

Figure 3.10. Linearity graphs for measurement and simulation resonance frequency vs. rod diameter in strain sensing application

3.1.4. Rotation Sensing Application

In this part, the rotation sensing ability has been investigated for some applications such as metallic rod position and rotation direction sensing, flow rate sensing and vorticity. The angular position has been determined for rod position application as illustrated in Figure 3.11. The positions have been set up between -90° and 90° by increasing 45° for each phase. The rod diameter has been chosen as 0.8 mm in this application.

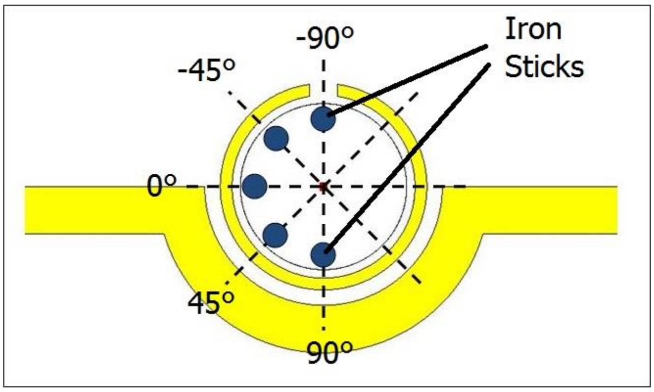

Figure 3.11. Test positions of rod sample placed inside the sensor layer for rotation sensing application

The purpose of this study is to determine the angular position and rotation direction of the metallic rod sample which have angular movement inside sensing layer. The numerical and experimental studies have been conducted by using preset test positions given in Figure 3.11. The results has been observed at the frequencies between 3.8 GHz and 4.3 GHz as illustrated in Figure 3.12. They shows that the resonance frequency of the sensor structure is depend on the rod position placed in the sensing layer.

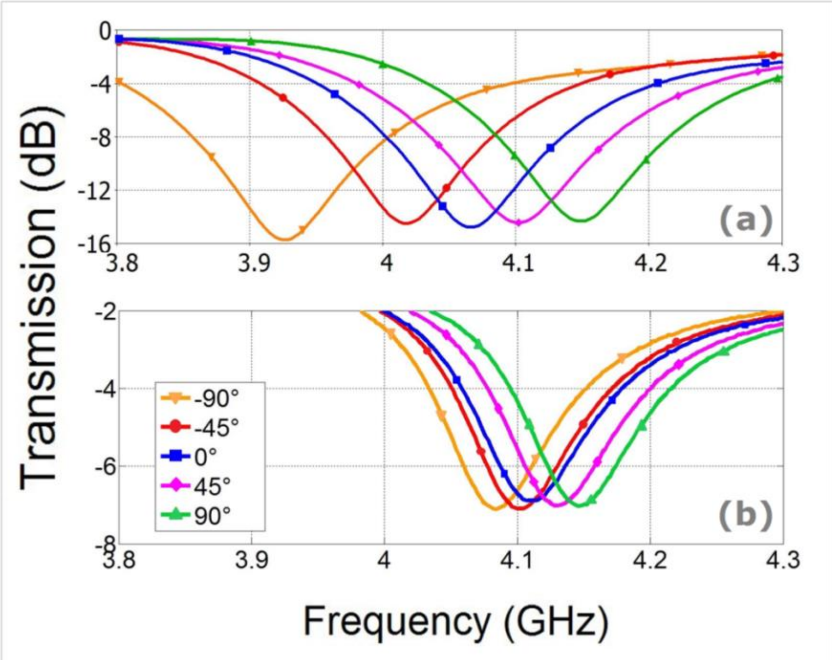

Figure 3.12. Transmission coefficient results for rotation sensing application; (a) numerical and (b) experimental studies

The transmission coefficient in resonance frequency has been obtained as about -16 dB for numerical studies and -7 dB for experimental studies. The simulated and measured resonance frequency points of the sensor is monitored as 3.929 GHz and 4.086 GHz for -90° of angular position, respectively. After that, the resonance frequencies are shifted upwards by 50 MHz for numerical study and 15 MHz for experimental study. Even though the increment in the experimental is study is smaller than the numerical studies, the sensor structure can be detect the rotation detection of the rod sample with high precision even small angle variations. The CSRR based sensor is not only to determine the angular position of the rod sample, it can also detect the rotation direction of the rod by monitoring slide direction of the resonance frequency.

Table 3.4. Rotation angles and corresponding simulated and measured resonance frequencies

Rotation (degree)	Simulated Resonance Frequency (GHz)	Measured Resonance Frequency (GHz)
-90°	3,929	4.086
-45°	4,019	4.102
0°	4,067	4.117
45°	4,102	4.132
90°	4,150	4.146

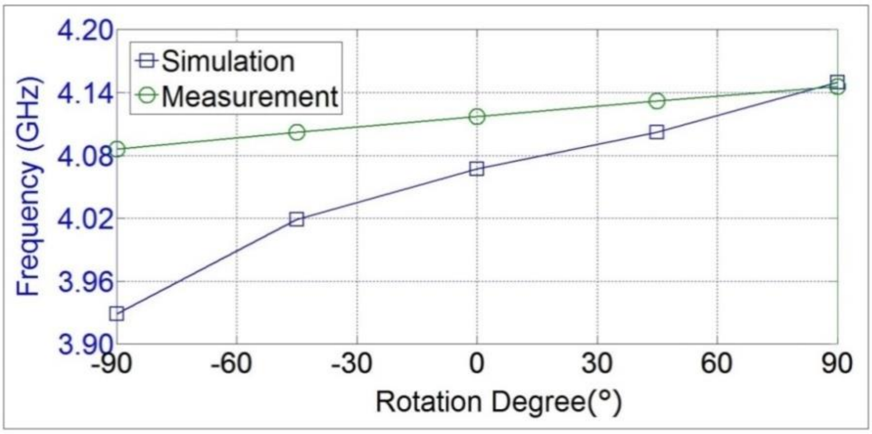

Figure 3.13. Linearity graphs for measurement and simulation resonance frequency vs. rotation degree in rotation sensing application

The resonance frequencies corresponding the rotation angle points are tabulated in Table 3.4. The lowest resonance frequency point has been observed at -90° of rotation angle. It should be noted that the resonance frequency tends to reduce as the rotation angle value increases. Therefore, the highest resonance frequency point is reached at 90° rotation angle. It is concluded that the CSRR based sensor structure can provide to detect the negative or positive rotation direction of the metallic rod samples by monitoring increments or decrements in the resonance frequency.

The linearity graphs for simulation and measurement results have been illustrated in Figure 3.13. It is plotted in 60 MHz frequency range and 220 MHz frequency range for experimental and numerical studies, respectively. The average slope angle of the linearity curves in Figure 3.13 can be calculated as $(tan^{-1}(\Delta f/\Delta\theta))$. This value is obtained as 50.85° for simulation study and 18.45° for experimental study. The difference between these angles results from the overall bandwidth in the frequency axis. As it can be seen in figure, the proposed sensor structure gives linear and precise results for both simulation and experimental studies. These linear responses or constant slopes prove that the CSRR based sensor structure determine the any angular changes in sensing layer. This proposed sensor can also be used as a flow rate sensor, since the angular position changes with respect to the flow velocity of liquids.

This section of the thesis study has been published in Journal of The Electrochemical Society. (doi.org/10.1149/2.1971712jes)

3.2. Chemical Liquid and Transformer Oil Quality Sensing Applications

In this section, another MTM based sensor structure which consist of a labyrinth type resonator (LTR) integrated on a transmission line has been used to detect chemical liquid type and transformer oil quality. The studies have been performed both numerically and experimentally at a microwave frequency band between 4 GHz and 5 GHz. The sensor structure have been firstly examined by numerically and theoretically. The equivalent circuit diagram of the sensor has been extracted and the circuit parameters are calculated. Parametric studies of the LTR dimensions and the electric field distribution have been realized to understand working mechanism of the sensor structure. After that, the electrical characteristics of the different chemical liquids have been measured for chemical liquid sensing study. This process has been also carried out for transformer oil quality sensing study by measuring dielectric properties of waste and clean transformer oil. Finally, both chemical liquid and transformer oil quality sensing studies have conducted both numerically and experimentally. The proposed sensing structure has potential to use in many industrial application areas such as energy, chemical and medicine to detect fuel adulteration and dielectric characterization of fluidics.

3.2.1. Design and Theory of the LTR based Chemical Sensor

The proposed MTM based sensor structure has a unique resonator design inserted a transmission line as shown in Figure 3.14. The resonator part of the sensor is called labyrinth type resonator which consist of five nested double split ring resonator as illustrated in Figure 3.14(a). This type of resonators is defined in the literature as a kind of MTM based resonator (Bilotti et al, 2007). The dimension parameters of the resonator have been named as outermost square ring (*Sline*), the dimension of the square sensing layer (*Gline*), the capacitive gap size (*gap*) and the resonator line and two adjacent rings width (*w*) and their values are listed in Table 3.5. The FR4 type substrate has been used as dielectric layer.

The working frequency band of the LTR based sensor has been arranged between 4 GHz and 5 GHz since the permittivity difference for samples such as waste and clean transformer oil samples is monitored at this frequency range. The dimensions of the resonator given in Table 3.5 have been obtained by considering the quarter wavelength of the center frequency.

Table 3.5. Dimensions of LTR

Sline	***Gline***	***gap***	***w***
24 mm	14.4 mm	8 mm	0.4 mm

The general view of the sensor structure has been demonstrated in Figure 3.14 (b). The back of the structure is covered by copper type metal. A transmission line is integrated to LTR with two discrete ports both endings to apply and observe the signals at certain frequencies. The sensing layer is created in the middle gap of the LTR. The samples placed in this layer with the help of the sample holder which fit sensing layer.

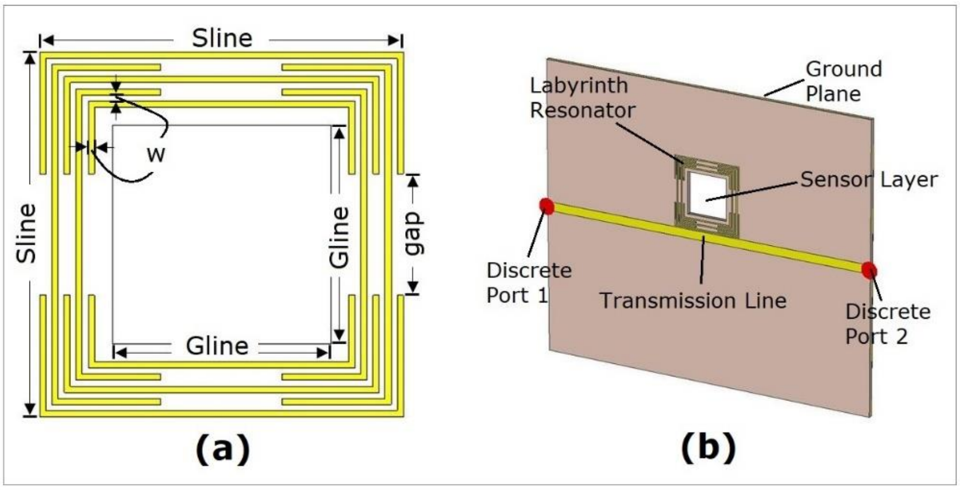

Figure 3.14. (a) The dimensions of the LTR and (b) Perspective view of the sensor structure

To understand working mechanism of the sensor structure, the equivalent circuit diagram has been extracted and analysis in Figure 3.15. Quasi-TEM mode of wave propagation is applied to the end of the microstrip transmission line. The magnetic coupling has been occurred between the equivalent resonator inductance (L_{eq}) and transmission line inductance (L_s) during the sensing process. There is a mutual inductance between these inductance (M) and it can be estimated by using Eq. (2.5). The total inductance of the structure (L_t) can be calculated in Eq. (2.4). In addition, it can be occur negligible mutual couplings between adjacent rings in the LTR as can be seen in Figure 3.15.

The equivalent circuit diagram of the sensor structure has been illustrated in Figure 3.15(b). The transmission line integrated sensor has a RLC circuit model. It means that any changes in inductive or capacitive part of the sensor has an effect on the resonant frequency.

The overall capacitance of the system C_t can be affected by the electrical changes in the vacuum, dielectric substrates and sample. The dimension parameters of the LTR plays key role to identify the total capacitance. All parameters which determine the total capacitance C_t is static parameters. The only one is the capacitance of the sample with respect to relative permittivity of the sample which can be expressed in Eq. (2.1). Therefore, the total capacitance of the sensor structure is associated with the real and imaginary part of the sample permittivity which is placed on the sensing layer. It can be written as Eq. (2.2).

Total capacitance (C_t) of the resonator is consists of the three parts demonstrated in Figure 3.15(b). They are (i) the cuts namely capacitive gaps placed in the double split ring resonators (C_{gap}), (ii) capacitive spaces between two adjacent ring (C_{adj}) and (iii) the capacitance of the sensing layer placed in the middle of the LTR (C_{samp}). Therefore, the overall capacitance can be written as;

$$C_t = C_{adj} + C_{gap} + \varepsilon_{samp} C_{samp} \tag{3.1}$$

The total of the distributed capacitances between adjacent rings is (Bilotti et al, 2007);

$$C_{adj} = \frac{C_0}{16}\left\{(N-1)\left[4(S_{line} - gap) - \frac{N}{2}(s + 2w)\right]\right\} \tag{3.2}$$

where N represents the number of double split ring resonator, *Sline* is the length of the outermost resonator, *w* is the width of the inductive line, *s* is the width of the gap between two adjacent rings (i.e. it is equal to the width of the line), *gap* is the length of the cut. (C_0) can be expressed as;

$$C_0 = \varepsilon_0 \varepsilon_r \frac{K\left(\sqrt{1-k^2}\right)}{K(k)} \tag{3.3}$$

where ε_0 is the vacuum permittivity, ε_r is the relative permittivity of the dielectric substrate, K is the complete elliptic integral of the first kind and $k = s/(s+2w)$.

The total of the capacitance associated with the *2N* cuts as (Bilotti et al., 2007);

$$C_{gap} = 2N\varepsilon_0 \varepsilon_r \frac{2w + \sqrt{2}gap}{\pi} \operatorname{arccos}h\left[\frac{2w + gap}{gap}\right] \tag{3.4}$$

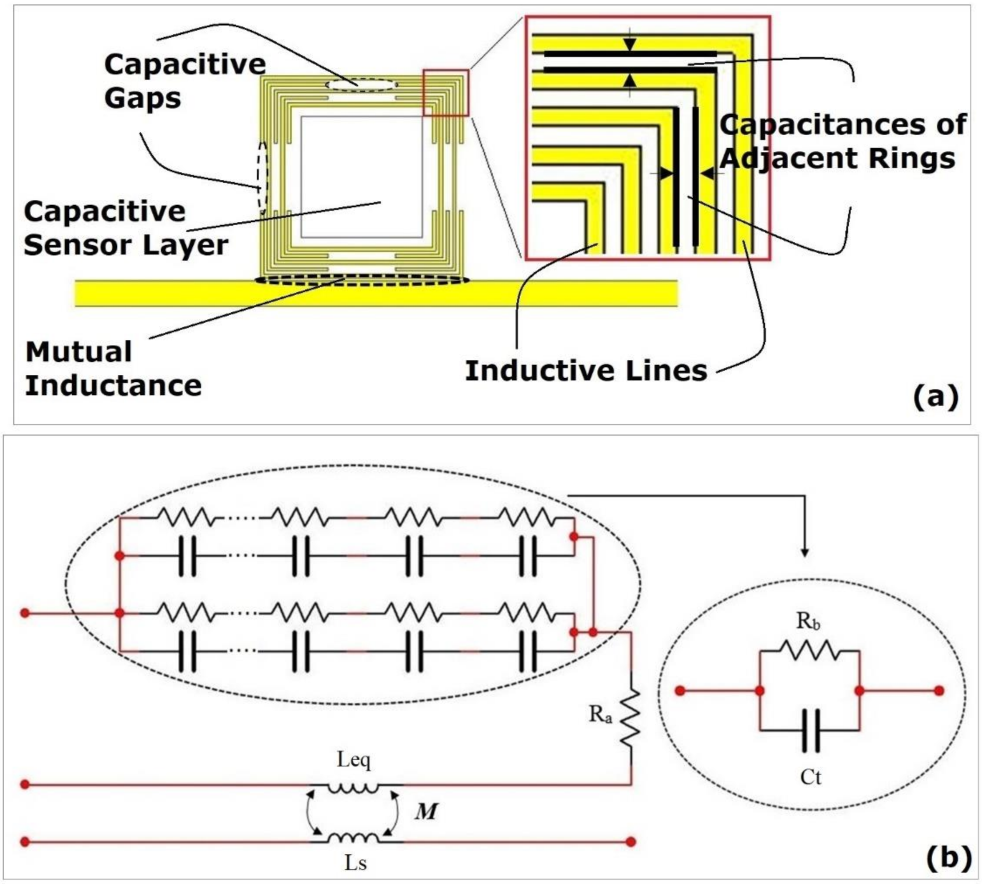

Figure 3.15. (a) Capacitive and inductive parts and (b) the equivalent circuit diagram of the LTR based sensor

The resonance frequency of the proposed structure can be calculated by the RLC equivalent circuit diagram in Eq. (2.6).

The inverse relation between the overall capacitance and resonance frequency can be seen in Eq (2.6). Therefore, while the capacitance of the sensor decreases or increases by the environmental causes, the resonance frequency of the sensor increases or decreases inversely. The parametric study is numerically performed to understand how the resonator parameters effect on the resonance frequency in Figure 3.16 (a) and (b).

The two parameters (dimension of the square ring (*Sline*) and the cut in resonator (*gap*)) affecting overall capacitance of the sensor have been investigated in Figure 3.16(a) and (b). The *Sline* parameter is varied from 23 mm to 26 mm by increasing 1 mm in each step at constant *gap* value of 8 mm. It can be seen in Figure 3.16 (a) that there is an inverse relation between the *Sline* parameter and resonance frequency of the sensor. While the *Sline* value increases, the resonance frequency value is decreases. As shown in Figure 316(a), frequency shifts of 200 MHz have been observed for each 1 mm increment. Hence, it can be noted that increasing of this parameter value is positively effect on the total capacitance of the sensor. In addition, the transmission magnitude does not changed by increasing or decreasing of *Sline* value, it remains constant at level of 40 %.

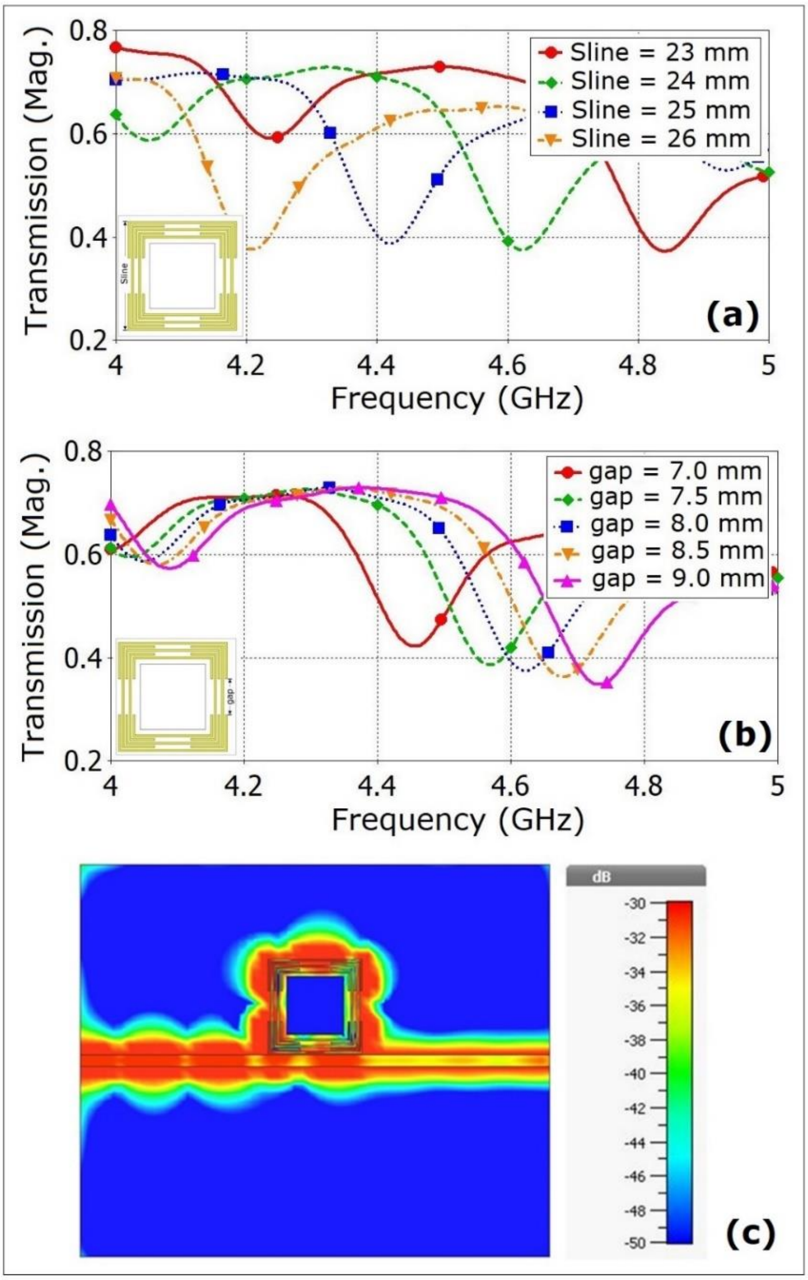

Figure 3.16. Parametric studies for (a) *Sline*, (b) *gap* and (c) electric field distribution of the sensor structure

The other parametric study is realized by cut dimension value namely *gap* in double split ring resonators as shown in Figure 3.16(b). The *gap* value is varied from 7 mm to 9 mm by increasing 0.5 mm in each step at constant *Sline* value of 24 mm. There is a direct relation between the *gap* dimension and resonance frequency. When the *gap* value increases, the capacitance between adjacent rings in Eq. (3.2) decreases and the resonance frequency value increases in Eq. (2.6). The increment in resonance frequency is almost constant (60 MHz) in every 0.5 mm increases of *gap* value. It can be noted that the *gap* value has negative impact on total capacitance of the sensor. Moreover, the transmission magnitude does not effect from the variation of *gap* parameter and it remains almost constants at 40%.

To understand sensing mechanism and observation transmitted power, the electric field distribution has been examined in Figure 3.16(c). The electric field distribution is monitored at the resonance frequency of 4.62 GHz and while the sensing layer is null. It is seen from the figure that the transmitted power from one port to another is dissipated. Lower than half of power is transmitted to receiver side of the transmission line. It proves that the transmitted power is at level of 40% in resonance frequencies as illustrated in Figure 3.16(a) and (b). In addition, the electric field is focused and highly concentrated especially on the resonator part of the sensor and sensing layer. This means that the sensor can perceive any electrical changes occurred in sensing layer precisely.

3.2.2. Chemical Liquid Detection Application with LTR based Sensor

In this part of the study, chemical liquid sensing study has been conducted by using electrical properties of ethanol, methanol, ammonia, isopropyl alcohol, polyethylene glycol 400 (PEG 400), polyethylene glycol 1500 (PEG 1500) and distilled water. The dielectric properties of these chemical fluidics have been measured by Agilent 85070E dielectric probe integrated to Agilent PNA-L series VNA as demonstrated in Figure 3.17. After that, these dielectric properties have been transferred to simulation program CST Microwave Studio. Finally, the numerical studies have been realized by observing transmission coefficient results for the chemical liquid samples placed to the sensing layer of sensor. Both studies have been performed at the frequency range between 4 GHz and 5 GHz.

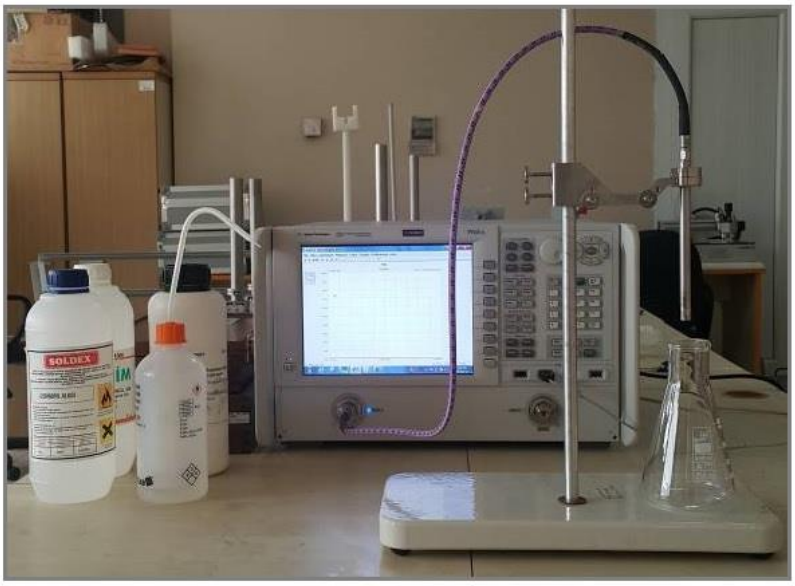

Figure 3.17. Experimental setup for dielectric measurements of the chemical liquid samples

Firstly, ethanol water mixture samples by increasing the ethanol volume from 0% to %40 have been used to detect ethanol ratio in the mixture. The dielectric constant and dielectric loss factor values have been monitored at between 4 GHz and 5 GHz as illustrated in Figure 3.18. When the frequency increases, the dielectric constant value is tend to decrease and dielectric loss value is tend to increase in the mixture samples. It means that the electrical characteristic of the samples is frequency dependent. The electrical characteristic is also changed with the ethanol ratio in the mixture. While the ethanol ratio is increasing, the dielectric constant is decreasing and the dielectric loss value is increasing. It seems that there is an unstable situation occurred in 40% ethanol ratio in mixture. Hence, the dielectric loss factor values have been observed in a wide range frequency band between 1 GHz and 20 GHz as shown in Figure 3.18(c). It can be seen from the Figure that the dielectric loss factor value is tend to decrease while the frequency is increases at the frequency range between 12-20 GHz. This can be explained as irregularity stem from the molecular response of the sample liquids. The other factor is the material of the sample holder which have a frequency dependent dielectric properties.

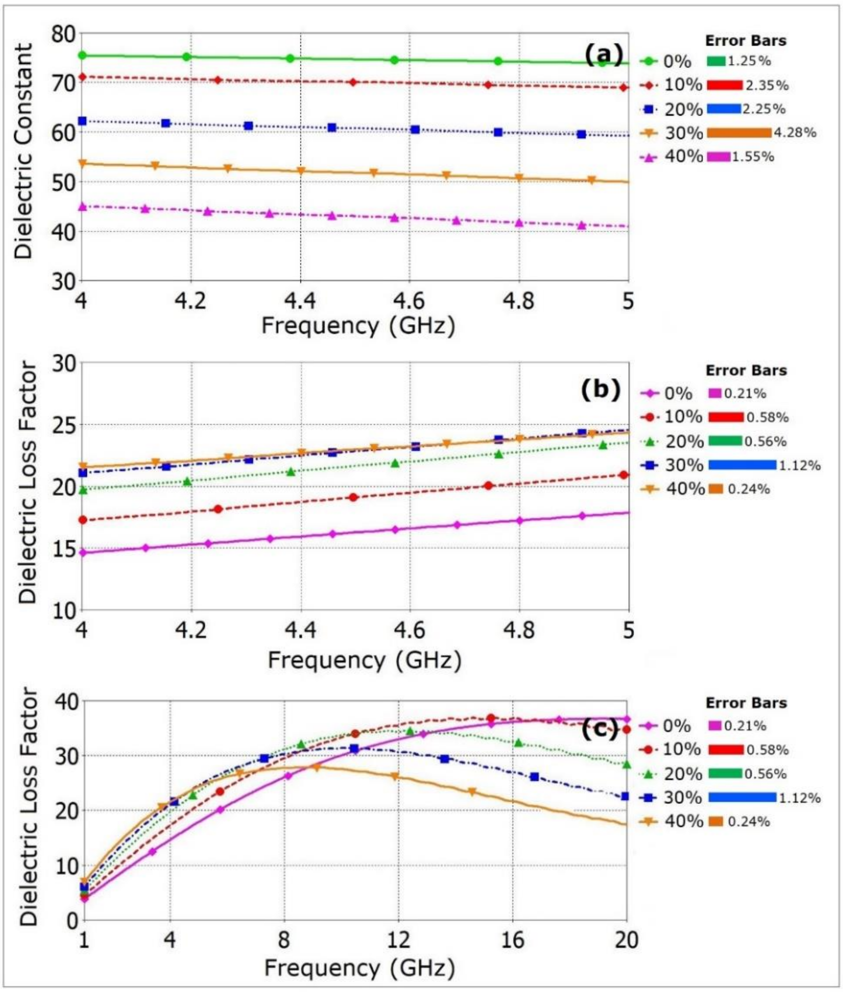

Figure 3.18. (a) The dielectric constant and (b) dielectric loss factor results for ethanol water mixture at (b) 4-5 GHz and (c) 1-20 GHz frequency band

After the measurement of the dielectric properties of the ethanol water mixtures, the obtained data is transfer to the simulation program. The transmission results of the ethanol water mixture samples are numerically plotted in Figure 3.19. The focused frequency range is between 4.2 GHz and 4.6 GHz as shown in Figure 3.19(a). While the ethanol content in the mixture is increasing, the resonance frequency is also increasing. Transmitted power ratio is reduced from the 60% to 50%, when the ethanol ratio is increased from 0% to 40%. Moreover, the linearity graph has been plotted in Figure 3.19(b). The resonance frequency due to ethanol ratio in the mixture sample almost gives linear response. It can be noted that the proposed sensor structure can detect the ethanol volume in the ethanol water mixture sensitively.

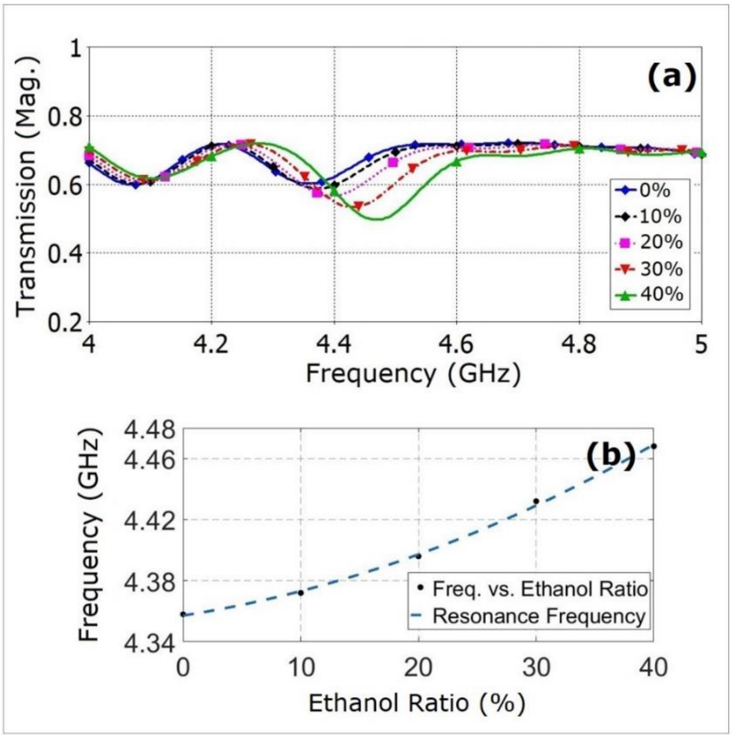

Figure 3.19. (a) Ethanol ratio sensing study and (b) linearity graph for frequency vs. ethanol ratio

The other chemical liquid sensing study has been realized by methanol water mixture samples at between 4 GHz and 5 GHz. The dielectric values for the methanol water mixtures due to methanol content have been illustrated in Figure 3.20. While the frequency increases, the dielectric constant is tend to decrease and the dielectric loss factor is tend to increase. The dielectric constant values are decreasing as the methanol volume in the mixture samples is increasing in Figure 3.20(a). Inversely, the dielectric loss factor values are increasing while the methanol ratio is increasing at between 4 GHz and 5 GHz as shown in Figure 3.20(b). The dielectric loss factor values for the methanol water mixture samples have been also investigated at between 1 GHz – 20 GHz to understand unstable behavior in some mixture ratios of methanol. For the methanol water mixture samples, the same relationship with the ethanol water mixture samples has been observed in Figure 3.20 (c). When the frequency increases between 12 GHz – 20 GHz, the dielectric loss factor of the methanol water mixture samples decreases.

The methanol ratio sensing study is numerically performed as demonstrated in Figure 3.21. The electrical characteristic results for the methanol water mixture samples have been imported and the transmission coefficient results have been observed at between 4 GHz – 5 GHz in Figure 3.21(a). The resonance frequency changes is observed especially 4.2 GHz and 4.6 GHz as ethanol water mixture results. The resonance frequency shifts by 15 MHz for each 10 % increment of methanol content in the mixture. The transmitted power reduces from 60% to 55 % due to increment of methanol ratio from 0 % to 40 %. In addition, the linearity graph for resonance frequency with respect to methanol content has been plotted in Figure 3.21(b). The graph shows that there is a linear relationship between these parameters. Hence, it can be concluded that the sensor structure is capable of determining the methanol volume content in the methanol water mixtures.

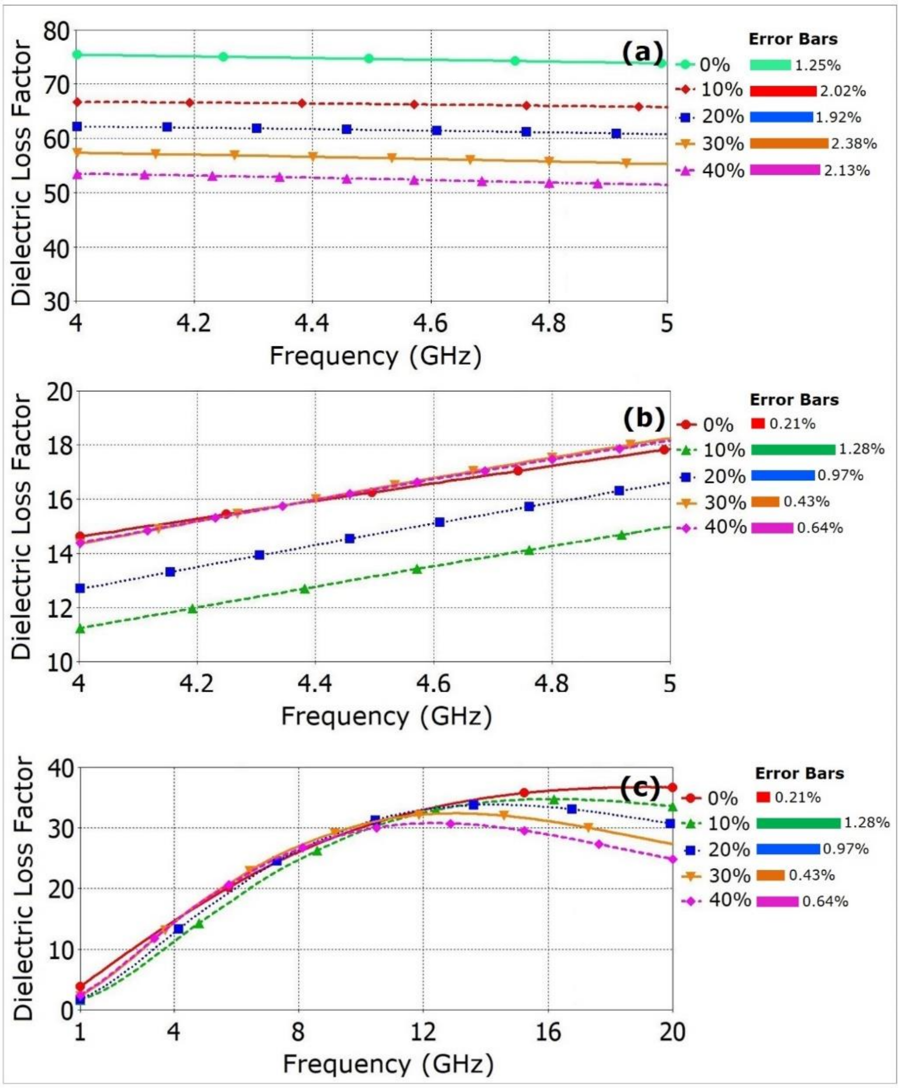

Figure 3.20. (a) The dielectric constant and (b) dielectric loss factor results for methanol water mixture at (b) 4-5 GHz and (c) 1-20 GHz frequency band

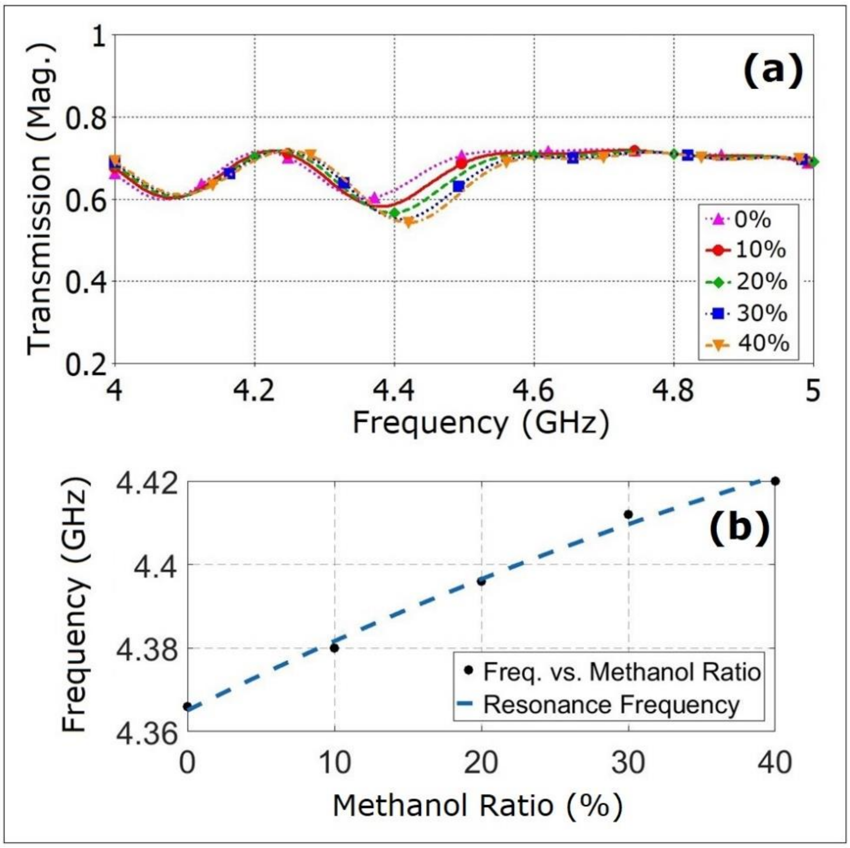

Figure 3.21. (a) Methanol ratio sensing study and (b) linearity graph for frequency vs. ethanol ratio

Finally, some chemical liquids such as ammonia, isopropyl alcohol, polyethylene glycol 400 (PEG 400) and polyethylene glycol 1500 (PEG 1500) have been used for testing sensing ability of the sensor against different fluidics. The common ways for these chosen liquids is that they are colorless and odorless except ammonia and isopropyl alcohol. Hence the proposed sensor can be used effectively to discriminate such chemicals which are very similar each other. The dielectric properties have been measured for these chemical liquids as shown in Figure 3.22. It can be seen from the figure that the all samples have frequency dependent characteristics. The PEG 1500 has electrical properties similar to air. In addition, the

PEG 1500, PEG 400 and Isopropyl Alcohol samples have similar electrical properties. Hence, these are the suitable chemicals to testing precision of the sensor.

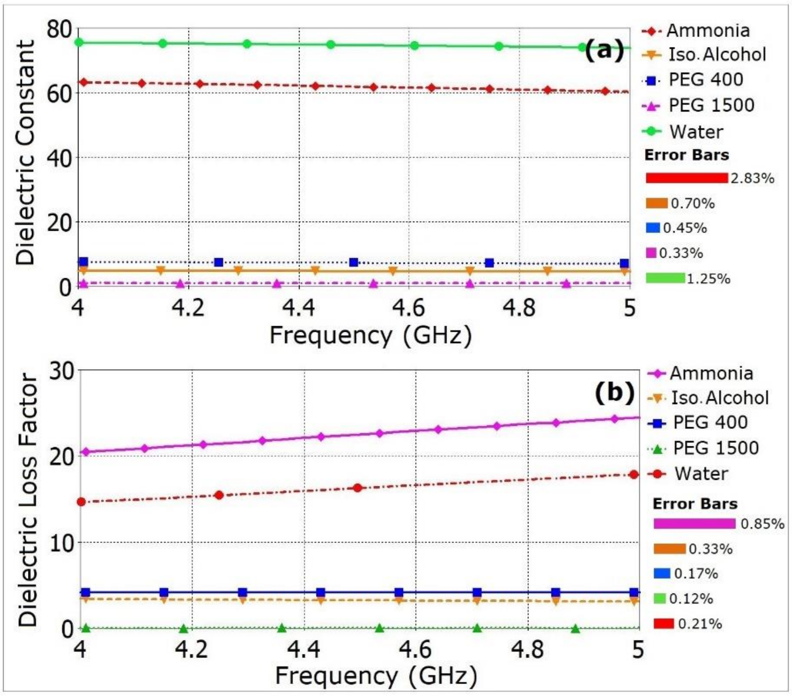

Figure 3.22. (a) The dielectric constant and (b) dielectric loss factor results for water, ammonia, isopropyl alcohol, polyethylene glycol 400 (PEG 400) and polyethylene glycol 1500 (PEG 1500) at 4 GHz-5 GHz

The electrical properties data files of the chemical liquid samples have been imported the CST simulation software to test the sensor structure with respect to transmission coefficient results as illustrated in Figure 3.23. The resonance frequency points have been obtained directly proportional with dielectric constant at between 4.2 GHz and 4.8 GHz. The resonance frequency for the PEG 1500 sample which has lowest dielectric constant is observed at 4.66 GHz. Resonance frequency was observed as 4.37 GHz for the water sample with the highest dielectric constant. The same relationship is observed for the results of the transmission coefficient. The transmission ratio for the PEG 1500 sample which has lowest dielectric constant is observed at the level of 39%. The transmission ratio for the water sample which has highest dielectric constant is observed at the level of 60%. The sensor structure also precisely discriminates the samples having close electrical properties (PEG 1500, PEG 400 and Isopropyl Alcohol) with the resonance frequency difference as 15 MHz in Figure 3.23.

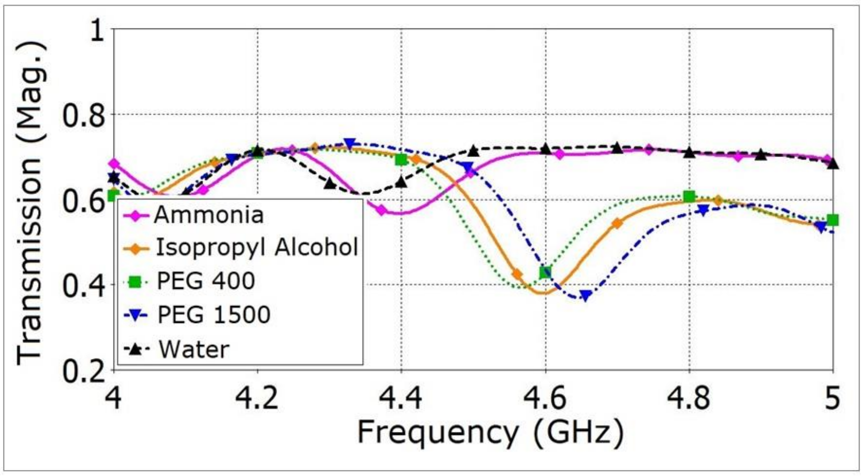

Figure 3.23. Different pure chemical liquid sensing study

3.2.3. Transformer Oil Quality Sensing Application with LTR based Sensor

In this part, the transformer oil quality sensing study has been conducted by using clean and waste transformer oil both numerically and experimentally. The transformer oils lose their functionality when exposed the high electrical energy at a long time. Hence, it is critical to determine the dysfunctionality time of the transformer oil to prevent failures and accidents. The proposed sensor is fabricated to distinguish the clean and waste transformer oil from each other as shown in Figure 3.24(a). LPKF ProtoMAT E33 prototyping machine has been used in manufacturing process and two SMA connector have been soldered both ends of the transmission line. A sample holder which is fit to the sensing layer and has been designed and producted by using 3D printing technology and it has been made by polycutic acid

(PLA) based material. In this way, the liquid samples safely have been placed in the sensing layer and the working mechanism of the sensor is not affected by the liquids with this non-destructive method.

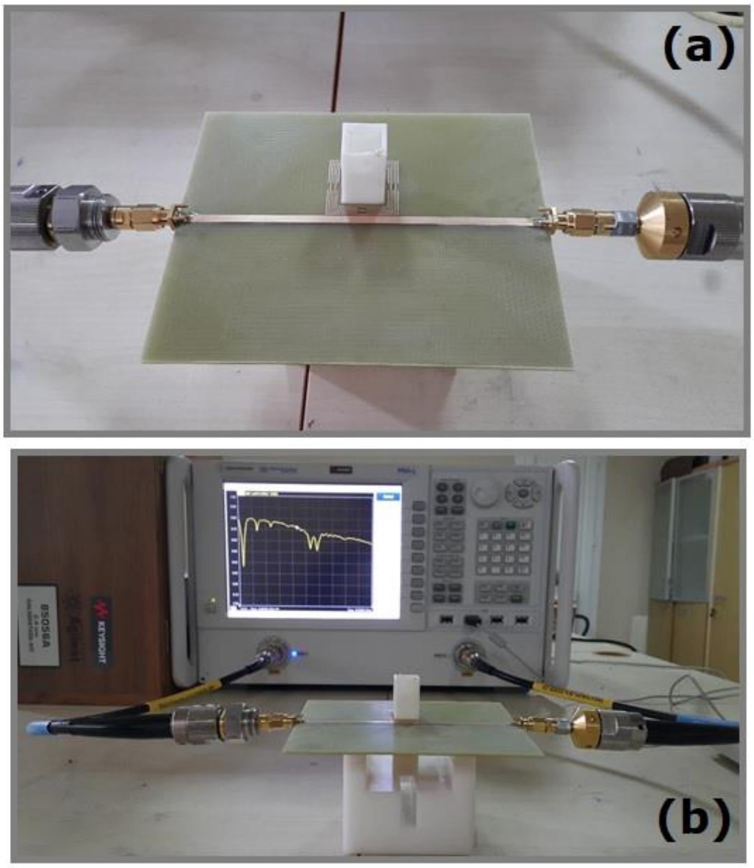

Figure 3.24. Manufactured sensor structure with the sample holder and (b) experimental setup

Measurement of transformer oil quality detection study is carried out by the dielectric probe kit and VNA in the frequency range between 4 GHz and 5 GHz. As the first step, the electrical properties of the clean oil samples, waste oil samples and sample holder have been measured as shown in Figure 3.25. The dielectric constant values for the clean and waste transformer oil samples have been monitored as about

2.7 and 2.9, respectively in Figure 3.25(a). The dielectric loss factors for these two oil samples have been observed at almost same level of 0.2 as shown in Figure 3.25(b). Besides these, the electrical properties of the sample holder are important with respect to sensitivity of the sensor. It can create extra capacitive effect in sensing layer. Hence the dielectric properties of sample holder have been investigated in Figure 3.25. The dielectric constant of the PLA based sample holder is about 1.9 and the dielectric loss factor of it is almost the similar level with oil samples. It should be noted that the electrical properties of the sample holder cannot create huge capacitance difference in sensing layer and it cannot prevent to monitor difference between the oil samples.

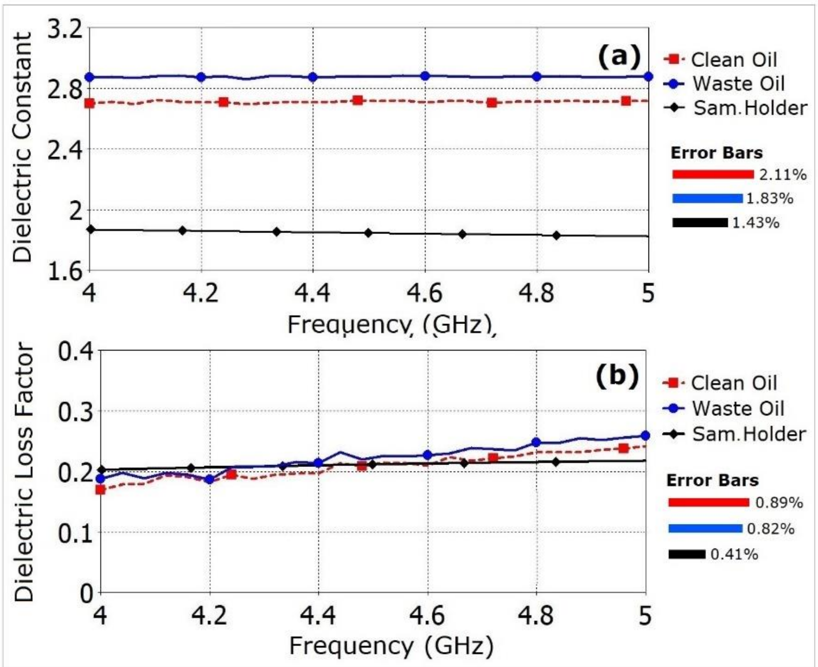

Figure 3.25. (a) The dielectric constant and (b) dielectric loss factor results for clean oil, waste oil and sample holder at 4-5 GHz frequency band

Transmission coefficient results for the transformer oil quality sensing study have been conducted both numerically and experimentally as shown in Figure 3.26.

The study has been realized at between 4 GHz and 5 GHz. The resonance frequency difference between the clean and waste oil samples is numerically observed as 40 MHz in Figure 3.26(a). This difference can be observed along with the operating frequency range between 4 GHz and 5 GHz. The transmission magnitude difference is almost not observed for oil samples at this frequency range. The experimental studies have been achieved at the same frequency range in Figure 3.26(b). The frequency shift is also observed as 40 MHz for the oil samples. Even though there is a mismatch (originated from manufacturing defects, soldering effects and non-perfect testing equipment) between the numerical and experimental results at the operating frequency range, the same frequency difference has been obtained for both studies. Besides this, 40 MHz of frequency difference for both results have been monitored at the working frequency range of the sensor (at between 4 GHz - 5 GHz). Hence, it can be concluded that the proposed sensor is able to determine the lifetime of the transformer oil.

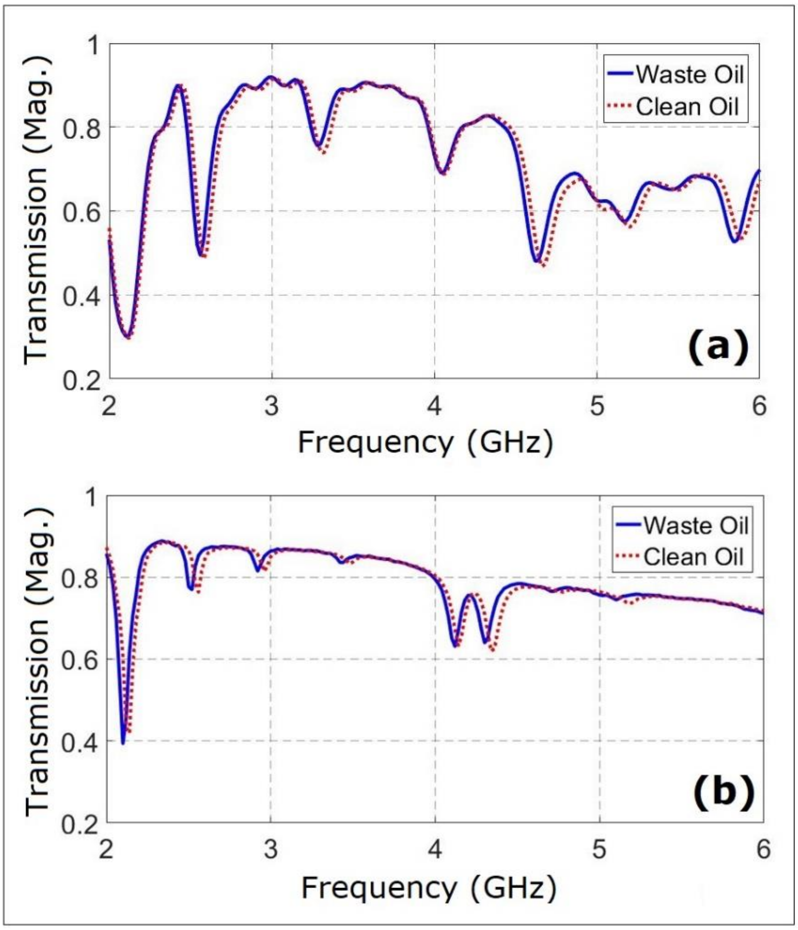

Figure 3.26. (a) Numerical and (b) experimental transmission coefficient for clean and waste oil at 2 GHz -6 GHz frequency band

This section of the thesis study has been published in Journal of The Electrochemical Society. (doi.org/10.1149/2.1101906jes)

3.3. Operating Frequency Configuration Application of the SRR based Sensor

In this study, the configuration of the operating frequency has been conducted by designing a SRR based transmission line integrated microwave sensor structure both numerically and experimentally design and theoretical process of the sensor structure has been firstly investigated and proved. The ethanol water mixtures with different ethanol content have been used to test the sensing ability of the SRR based sensor structure. Five different sensor structure have been produced and performed to observe how the sensor works in different operating frequency ranges. When the sensor structures have been designed, a dimension coefficient of '*k*' has been set as 0.8, 0.6, 1, 1.2 and 1.4. These five different sensor structures have been obtained by using the dimension coefficient of 'k'. The proposed sensor can be used in many applications requiring different operating microwave frequency ranges by configuring the dimension parameters. The study has also aimed to detect different types of samples having frequency depending characteristics.

3.3.1. Design and Theory of the SRR based Sensor

A SRR based sensor structure have been designed for operating frequency configuration study as shown in Figure 3.27(a). Since the split ring resonator type sensor structures have the strong electrical coupling with samples placed in capacitive sensing layer, SRR based sensor structure has been chosen to observe small electrical variations in the sensing layer (Ebrahimi et al, 2013; Withayachumnankul et al, 2013). FR4 type dielectric layer is chosen as dielectric layer. The dimension parameters which are height of the SRR (l), width of the SRR (s), gap of the split part (g), width of the SRR line (w), thickness of the transmission line (t) and the gap between SRR and transmission line (h) have been tabulated in Table 3.6.

The working frequency band for the SRR based configuration study has been adjusted from 1.6 GHz to 2.4 GHz since many microwave applications such as wireless communication, antennas and sensors has been improved at this frequency range. The dimensions of the resonator given in Table 3.6 have been estimated by considering the quarter wavelength of the center frequency.

Table 3.6 Dimension values of the SRR based sensor structure

l	**s**	**t**	**h**	**g**	**w**
22 mm	18 mm	2 mm	0.2 mm	3 mm	2 mm

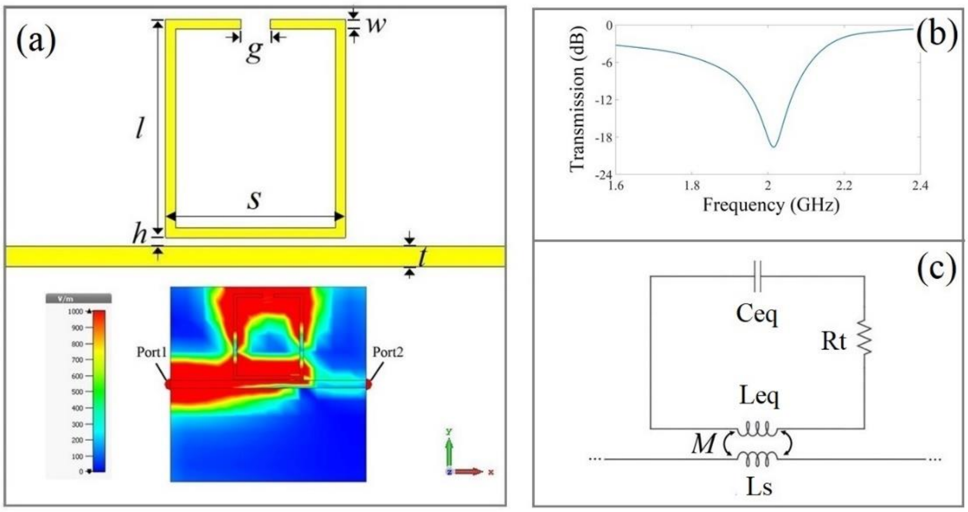

Figure 3.27. (a) Parametric dimensions and electric field distribution, (b) transmission graph and (c) equivalent circuit diagram for the proposed SRR based microfluidic sensor

The sensing layer of the sensor structure has been obtained by drilling split gap of the SRR. Thus, it is provided transferring liquid samples by through this channel. The transmission coefficient results and frequency shifts have been monitored in this study. The numerical transmission coefficient results for designed sensor structure with empty sensing layer have been obtained in Figure 3.27(b). The resonance frequency at minimum transmitted power has been observed at around 2 GHz. The resonance frequency of the sensor structure is depend on the electrical variations occurred in capacitive layers especially in the sensing layer. The equivalent circuit diagram has been investigated to present working principle of the sensor as shown in Figure 3.27(c). The SRR has series type of RLC circuit behavior and it has magnetic coupling with the transmission line. The mutual inductance

(M) has been occurred between the inductive parts of the transmission line (L_s) and SRR (L_{eq}). The total inductance of the sensor (L_t) can be calculated in Eq. (2.4) and the mutual inductance (M) is estimated in Eq. (2.5).

To determine the resonance frequency, the inductive parts (L_{eq}, L_s) and capacitive part (C_{eq}) of the sensor have been play the most important roles. There also exist some external capacitive parts (such as capacitive effect stem from the sample placed on sensor layer ($\varepsilon_{samp}C_{sens}$) and capacitance of the surrounding space (C_0) to effect total capacitance of the system. The overall capacitance (C_t) can be presented in Eq. (2.3).

The variable capacitive effect is occurred in the changes of electrical properties of the sample. The permittivity of a sample can be described as Eq. (2.1). This permittivity equation is consist of the dielectric constant and dielectric loss. Hence, the total capacitance is a function of permittivity of the sample as seen in Eq. (2.2).

The resonance frequency of the sensor structure can be written as Eq. (2.6). It depends on the total inductance (L_t) and overall capacitance (C_t) of the sensor. The resonance frequency is also a function of the permittivity of the sample placed in the sensing layer as the total capacitance (C_t) depends on the electrical characteristic of the sample. Hence, the samples can be detected with respect to their dielectric properties by monitoring variations in resonance frequency of the sensor.

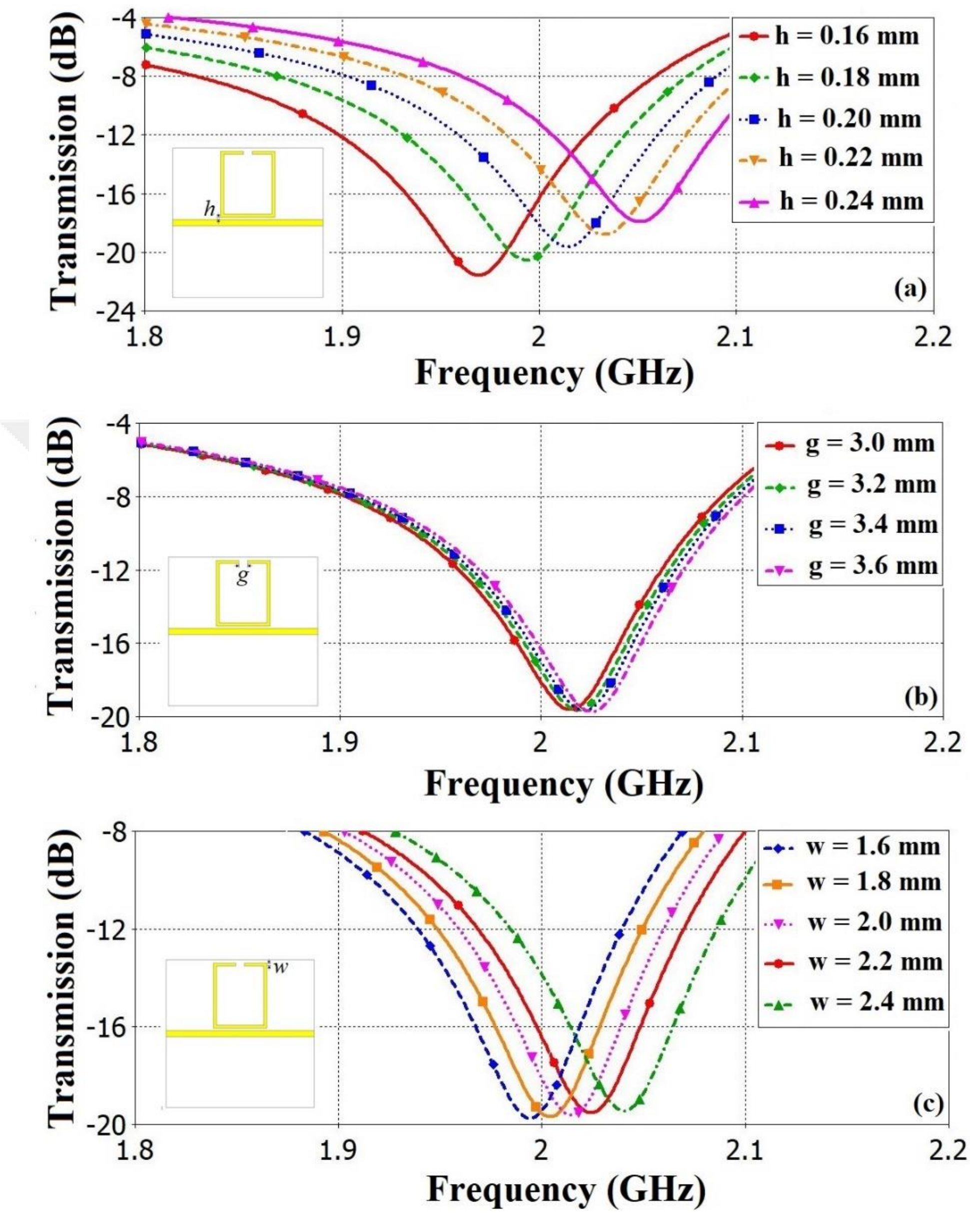

Figure 3.28. Parametric study on transmission coefficient and resonance frequency for the parameters (a) *h*, (b) *g* and (c) *w*

The parametric studies have been realized to how the dimension parameters effect transmission magnitude and resonance frequency. The gap between SRR and transmission line (*h*), gap of the split part (*g*) and width of the SRR line (*w*), have been studied in Figure 3.28. While the *h* parameter is increasing from 0.16 mm to 0.24 mm, the resonance frequency is also increasing from 1.98 GHz to 2.07 GHz as illustrated in Figure 3.28(a). In the same manner, the transmission magnitude also increases with the increments of the *h* value. The transmission magnitude and resonance frequency does not almost effect from the increments of the *g* value as shown in Figure 3.28 (b). While the SRR line width *w* is increasing from 1.6 mm to 2.4 mm, the resonance frequency is also increasing from 1.99 GHz to 2.05 GHz as shown in Figure 3.28(c). The transmission line coefficient is not effected from the variation of *w*. It should be noted that these dimension parameters have an effect on the total inductance or capacitance of the sensor as the resonant frequency of the sensor changes from any variation of its values. The optimal values for *h*, *g* and *w* have been determined as 0.2 mm, 3 mm and 2 mm, respectively.

3.3.2. Experimental Studies for the SRR based Sensor

The proposed sensor structures have been produced by using the PCB prototyping machine with milling technique as shown Figure 3.29. Five sensor structures with different dimension coefficient *k* have been manufactured and examined for configuration operating frequency study. All sensor structure have the same sensing layer dimensions by drilling a channel in split gap part of them.

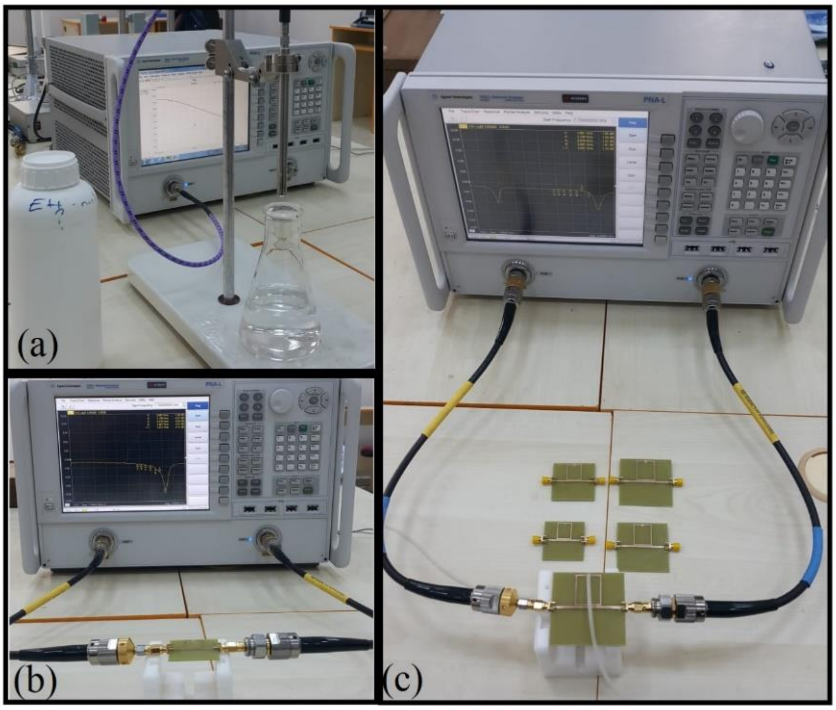

Figure 3.29. (a) Permittivity measurement setup, (b) transmission coefficient measurement setup with VNA and (c) manufactured sensor structures

Agilent PNA-L VNA with two 50 ohm coaxial cables has been used in the experimental works as demonstrated in Figure 3.29(b). An open ended dielectric probe has measured the dielectric properties of the liquid samples as shown in Figure 3.29(a). After measuring electrical properties of liquid samples, the sensor structures respectively connected to VNA and the transmission coefficients in dB has been observed. The VNA has been calibrated for each different sensor structure with respect to numerically observed operating frequency ranges of them.

The sensor structures are firstly scaled with the dimensions coefficient *k*. After that the numerical studies have been realized and operating frequency ranges determined. Finally, the sensors are produced as shown in Figure 3.29(c). The experimental studies have been achieved and the results have been compared with the numerical results.

The five sensor structures have been obtained by multiplying the dimension parameters with these k number. The dimensions coefficient *k* is selected as 0.6, 0.8, 1, 1.2 and 1.4. These coefficients have been chosen as linearly to observe whether or not the operating frequency ranges for the sensor structures have been changes linearly too.

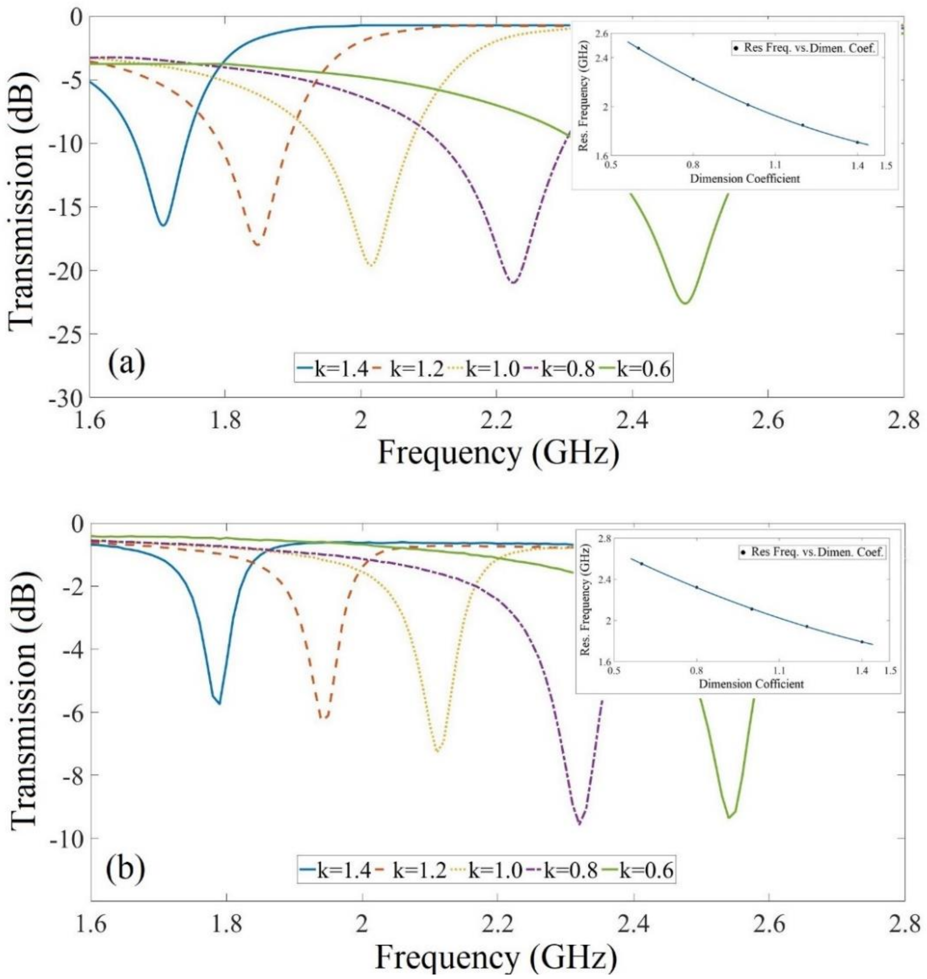

Figure 3.30. (a) Numerical and (b) experimental resonance frequency results for sensor structures with a dimension coefficient of 1.4, 1.2, 1, 0.8 and 0.6

Transmission coefficient results for both numerically and experimentally have been obtained in Figure 3.30. The results have been observed at the frequency range between 1.6 GHz and 2.8 GHz while the sensing layer is empty. The resonance frequency at the lowest transmission magnitude is inversely proportional to the dimension coefficient as illustrated in Figure 3.30. The resonance frequencies have increased due to decrease in the dimension coefficient *k*. The linearity graphs which show the relation between the resonance frequency points and the dimension coefficient *k* have been added both figures. It can be concluded that the decrease linear relation between the resonance frequency and dimension coefficient has been monitored both numerically and experimentally. Moreover, numerical and experimental results are in a good agreement. There is only a small frequency difference between both results, which is stem from the non-perfect sensitivity of milling process and soldering.

3.3.3. Configuration Study for the SRR based Sensor

In this section, the operating configuration study has been conducted by using ethanol water mixture samples both numerically and experimentally. The samples have been prepared as 0%, 20%, 40%, 60%, 80% and 100% of ethanol content in the ethanol water mixtures. Their electrical characteristics have been firstly measured at between 1 GHz and 2.8 GHz of frequency range via the coaxial dielectric probe kit. The dielectric constant and dielectric loss factor results have been plotted in Figure 3.31.

The dielectric constant values for all prepared samples are tend to decrease while the frequency is increasing as shown in Figure 3.31(a). The dielectric constant values are increasing with the decrements of the ethanol content in the mixture. The dielectric loss factor value is increasing while the ethanol content in the mixture is increasing as demonstrated in Figure 3.31(b). The unstable behavior of the dielectric loss is influenced from the used sample holder type and shape during the electrical characteristics measurement process. Besides the calibration error of the coaxial probe and frequency-dependent characteristics of the samples have been caused to this nonlinear behavior. The resonance frequency shifts have been observed linearly for all sensor structures although the nonlinear variations in the dielectric loss results. It can be seen from the sensing results that only the transmission coefficients are affected by the dielectric loss results of the mixture samples. Besides this, the dielectric measurement results in a good agreement with the literature (Withayachumnankul et al., 2013; Ebrahimi et al., 2013; Abduljabar et al. 2014).

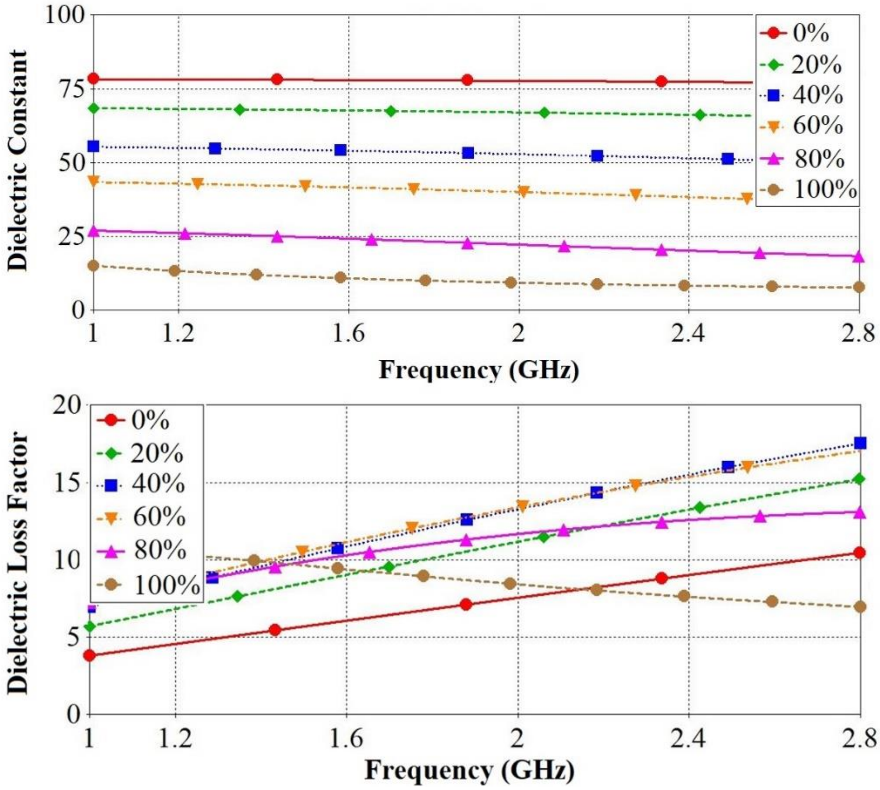

Figure 3.31. Dielectric constant and dielectric loss values for ethanol-water mixtures having ethanol content of 0%, 20%, 40%, 60%, 80% and 100%

The resonance frequency results for the sensor structures which have the dimension coefficient of 1.4, 1.2, 1, 0.8 and 0.6 have been illustrated in Figure 3.32, 3.33, 3.34, 3.35 and 3.36, respectively. Each figure has been also included the linearity graph between resonance frequency and ethanol volume content in the mixture samples. The linear relations have been observed for all scaled sensor structure. Moreover, there is a good agreement between simulated and measured results for all sensor structures. The resonance frequency points both numerically and experimentally are tabulated in Table 3.7, 3.8, 3.9, 3.10 and 3.11 for the sensor structures which have the dimension coefficient of 1.4, 1.2, 1, 0.8 and 0.6, respectively.

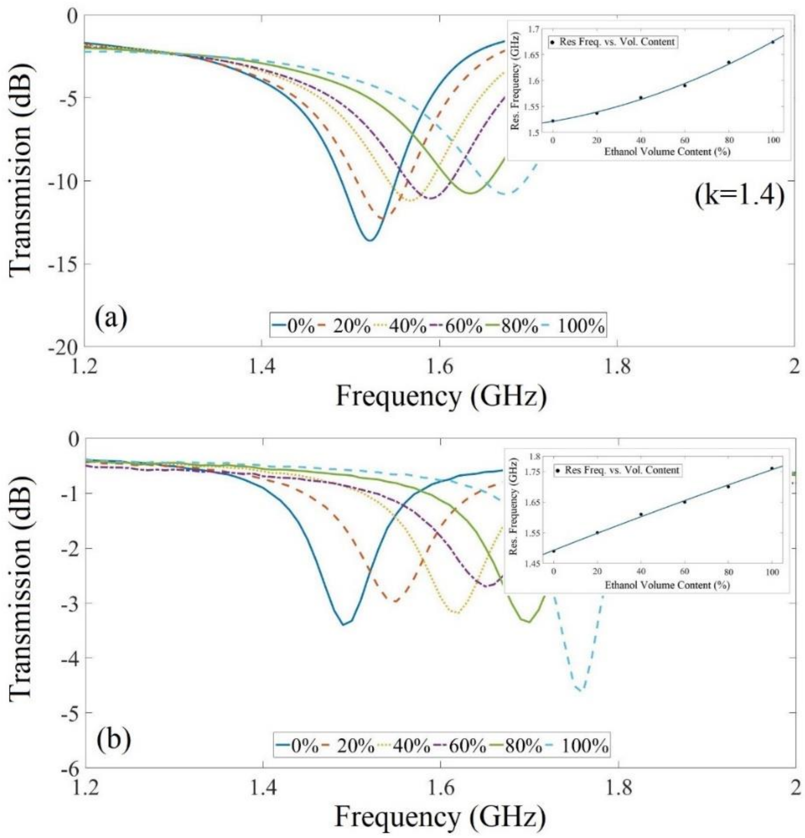

Figure 3.32. (a) Numerical and (b) experimental transmission coefficient and resonance frequency results for the sensor structure having dimension coefficient *k*=1.4.

The operating frequency range for the sensor structure which has the dimension coefficient of 1.4 is obtained at between 1.2 GHz and 2 GHz as illustrated in Figure 3.32. The resonance frequency points are tabulated in Table 3.7. The numerical and experimental resonance frequencies for the mixture sample of 0% ethanol content has been observed as 1.522 GHz and 1.490 GHz, respectively. The frequency difference has been obtained as 32 MHz. The numerical and experimental resonance frequencies for the mixture sample of 100% ethanol content have been observed as 1.674 GHz and 1.760 GHz, respectively. The frequency difference has been obtained as 86 MHz. Hence, the experimental study for *k*=1.4 is monitored wider frequency range than numerical study.

Table 3.7. Numerical and experimental resonance frequency points for *k*=1.4

Ethanol Content (%)	**0%**	**20%**	**40%**	**60%**	**80%**	**100%**
Simulated Resonance Frequency (GHz)	1.522	1.537	1.567	1.590	1.635	1.674
Measured Resonance Frequency (GHz)	1.490	1.550	1.610	1.650	1.700	1.760

The operating frequency range for the sensor structure which has the dimension coefficient of 1.2 is obtained at between 1.4 GHz and 2.2 GHz as illustrated in Figure 3.33. The resonance frequency points are tabulated in Table 3.8. The numerical and experimental resonance frequencies for the mixture sample of 0% ethanol content have been observed as 1.644 GHz and 1.630 GHz, respectively. The difference in resonance frequencies obtained in the numerical and experimental studies is 14 MHz. The numerical and experimental resonance frequencies for the mixture sample of 100% ethanol content has been observed as 1.812 GHz and 1.900 GHz, respectively. The frequency difference has been obtained as 88 MHz. Hence, the experimental study for *k*=1.2 is monitored wider frequency range than numerical study.

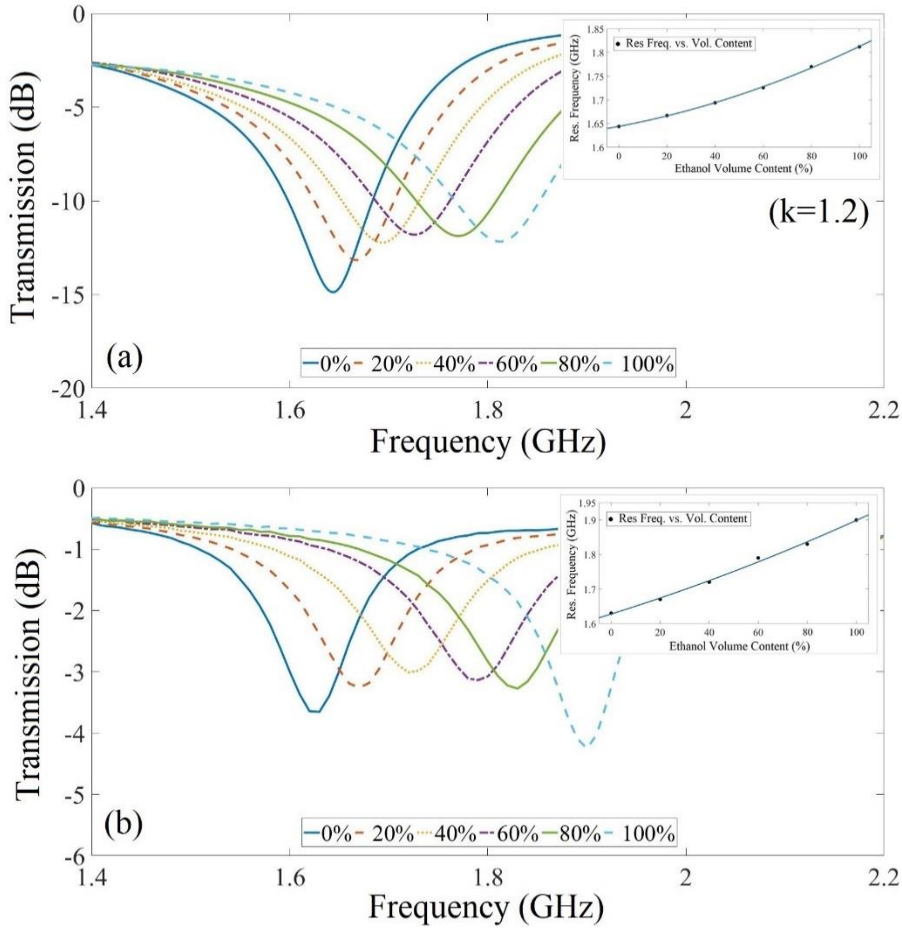

Figure 3.33. (a) Numerical and (b) experimental transmission coefficient and resonance frequency results for the sensor structure having dimension coefficient *k*=1.2.

Table 3.8 Numerical and experimental resonance frequency points for *k*=1.2

Ethanol Content (%)	0%	20%	40%	60%	80%	100%
Simulated Resonance Frequency (GHz)	1.644	1.667	1.694	1.726	1.770	1.812
Measured Resonance Frequency (GHz)	1.630	1.670	1.720	1.790	1.830	1.900

The operating frequency range for the sensor structure which has the dimension coefficient of 1 is obtained at between 1.6 GHz and 2.4 GHz as illustrated in Figure 3.34. The resonance frequency points are tabulated in Table 3.9. The numerical and experimental resonance frequencies for the mixture sample of 0% ethanol content have been observed as 1.798 GHz and 1.780 GHz, respectively. The frequency difference has been obtained as 18 MHz. The numerical and experimental resonance frequencies for the mixture sample of 100% ethanol content have been observed as 1.979 GHz and 2.050 GHz, respectively. The frequency difference has been obtained as 71 MHz. Hence, the experimental study for *k*=1 is monitored wider frequency range than numerical study.

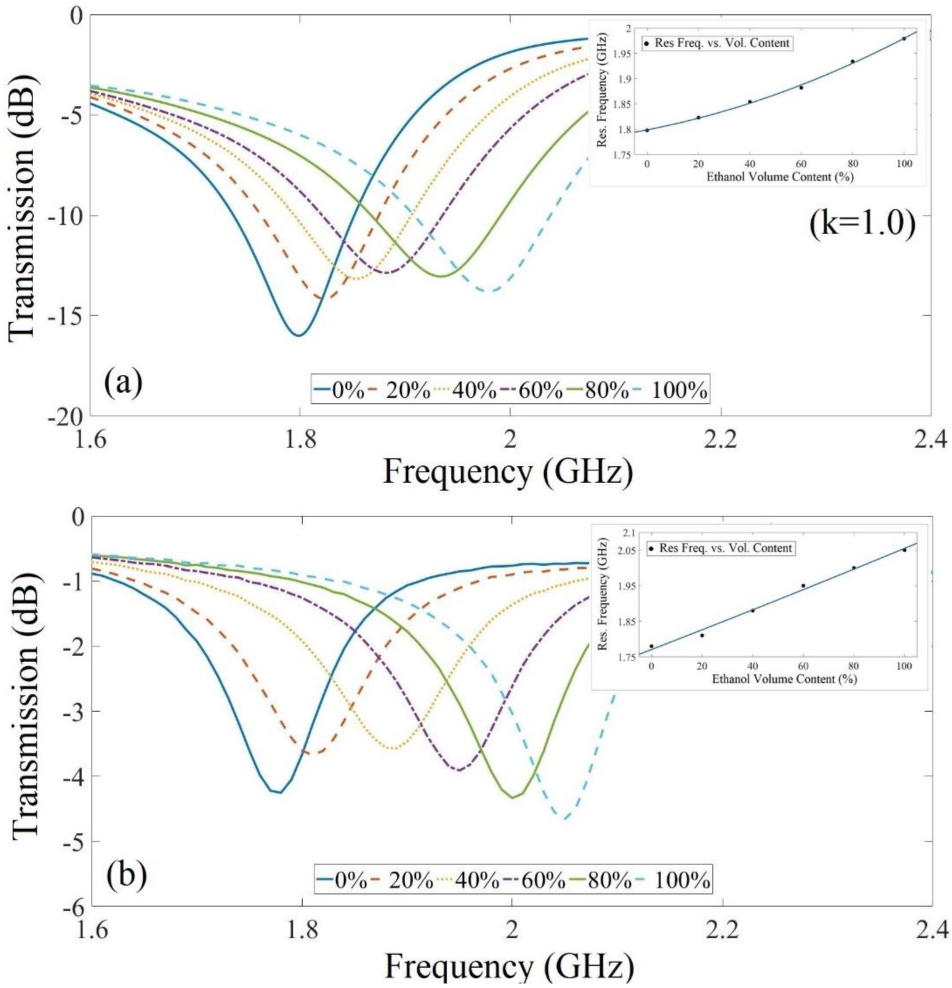

Figure 3.34. (a) Numerical and (b) experimental transmission coefficient and resonance frequency results for the sensor structure having dimension coefficient *k*=1

Table 3.9 Numerical and experimental resonance frequency points for *k*=1

Ethanol Content (%)	**0%**	**20%**	**40%**	**60%**	**80%**	**100%**
Simulated Resonance Frequency (GHz)	1.798	1.823	1.854	1.882	1.934	1.979
Measured Resonance Frequency (GHz)	1.780	1.810	1.880	1.950	2.000	2.050

The operating frequency range for the sensor structure which has the dimension coefficient of 0.8 is obtained at between 1.8 GHz and 2.6 GHz as illustrated in Figure 3.35. The resonance frequency points are tabulated in Table 3.10. The numerical and experimental resonance frequencies for the mixture sample of 0% ethanol content have been observed as 1.992 GHz and 1.940 GHz, respectively. The frequency difference has been obtained as 52 MHz. The numerical and experimental resonance frequencies for the mixture sample of 100% ethanol content have been observed as 2.189 GHz and 2.250 GHz, respectively. The frequency difference has been obtained as 61 MHz. Hence, the experimental study for *k*=0.8 is monitored wider frequency range than numerical study.

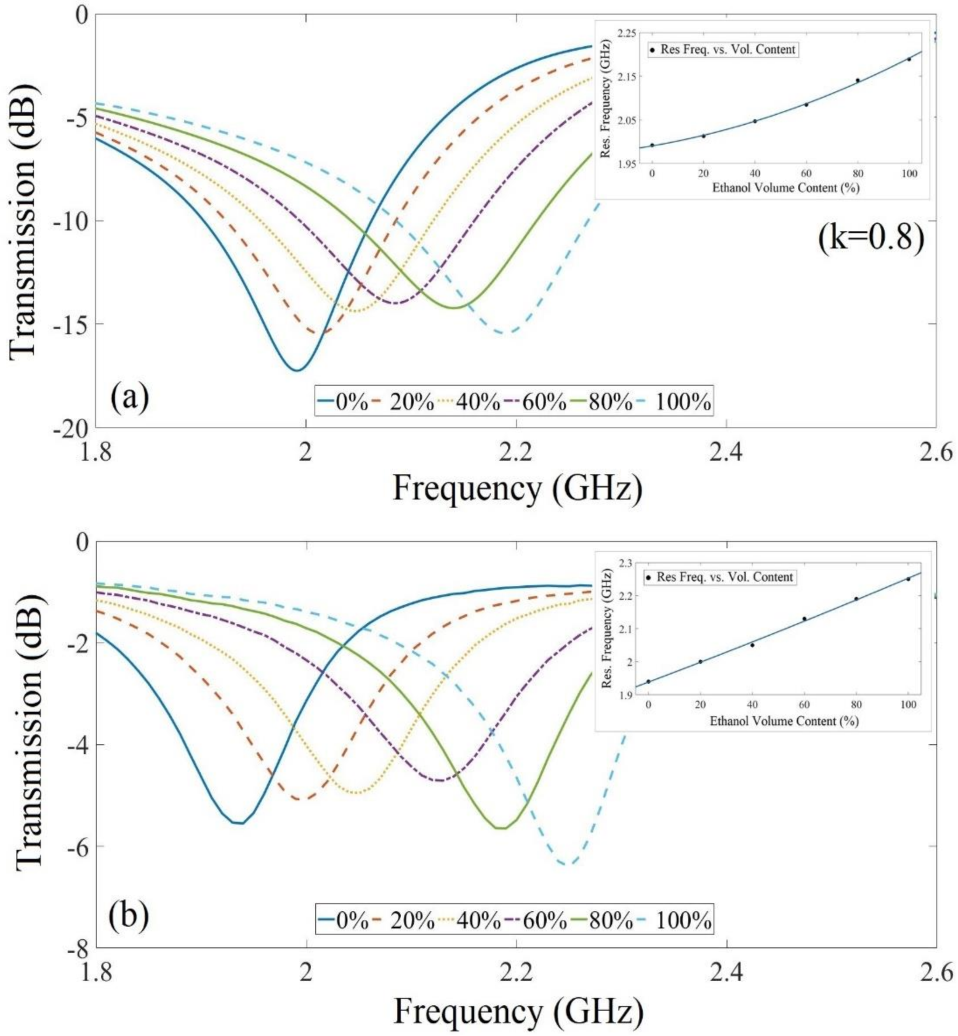

Figure 3.35 (a) Numerical and (b) experimental transmission coefficient and resonance frequency results for the sensor structure having dimension coefficient *k*=0.8

Table 3.10 Numerical and experimental resonance frequency points for *k*=0.8

Ethanol Content (%)	0%	20%	40%	60%	80%	100%
Simulated Resonance Frequency (GHz)	1.992	2.013	2.047	2.085	2.141	2.189
Measured Resonance Frequency (GHz)	1.940	2.000	2.050	2.130	2.190	2.250

The operating frequency range for the sensor structure which has the dimension coefficient of 0.6 is obtained at between 2 GHz and 2.8 GHz as illustrated in Figure 3.36. The resonance frequency points are tabulated in Table 3.11. The numerical and experimental resonance frequencies for the mixture sample of 0% ethanol content have been observed as 2.222 GHz and 2.150 GHz, respectively. The frequency difference has been obtained as 72 MHz. The numerical and experimental resonance frequencies for the mixture sample of 100% ethanol content have been observed as 2.443 GHz and 2.495 GHz, respectively. The frequency difference has been obtained as 52 MHz. Hence, the numerical study for *k*=0.6 is monitored wider frequency range than experimental study.

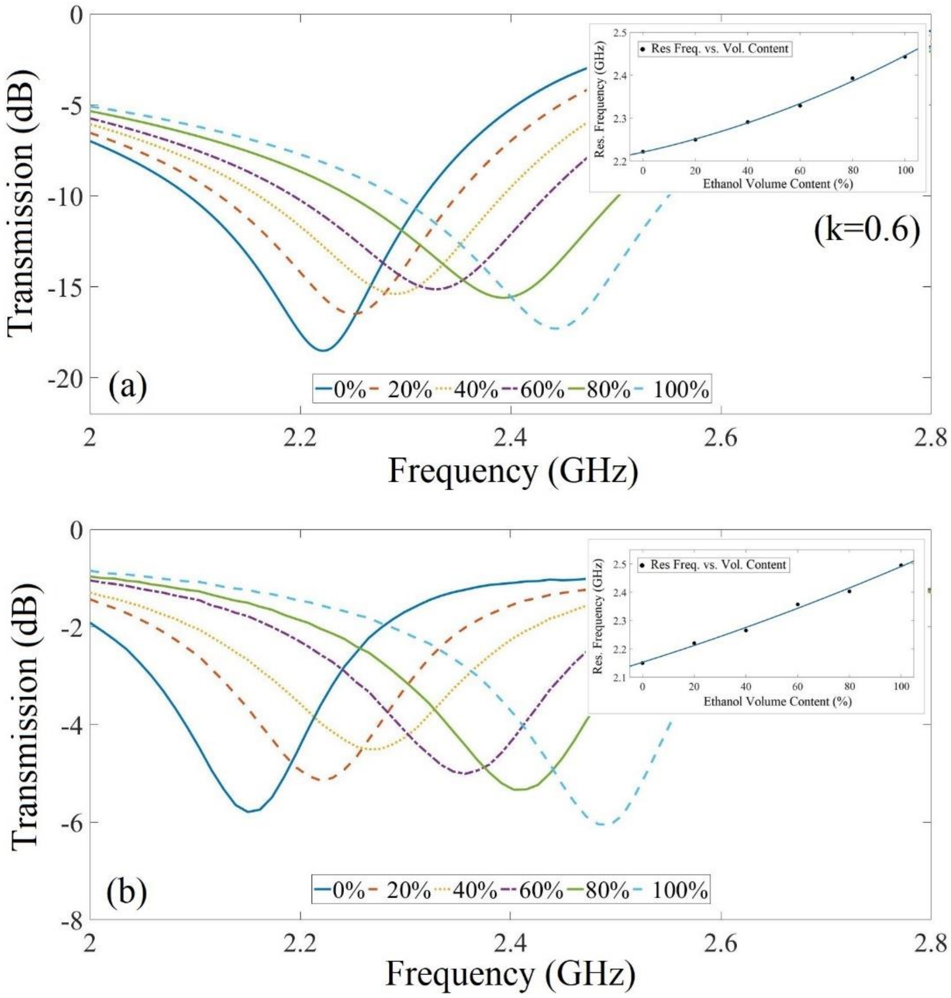

Figure 3.36. (a) Numerical and (b) experimental transmission coefficient and resonance frequency results for the sensor structure having dimension coefficient *k*=0.6

Table 3.11 Numerical and experimental resonance frequency points for *k*=0.6

Ethanol Content (%)	**0%**	**20%**	**40%**	**60%**	**80%**	**100%**
Simulated Resonance Frequency (GHz)	2.222	2.250	2.291	2.329	2.393	2.443
Measured Resonance Frequency (GHz)	2.150	2.220	2.265	2.357	2.403	2.495

3.4. Wastewater Quality Sensing Application with DSRR based Sensor

In this section, a DSRR based sensor structure has been design numerically to sense wastewater quality in there phases which are output, ventilation and backreturn. The wastewater samples in three phases have been chemically examined and the amount of suspended solid mixture them is measured in mg. The quality of the water is then determined. The electrical characteristics of these three samples have been measured at the frequency between 1.5 GHz and 2 GHz. Finally, the samples have been successfully tested by using a DSRR based transmission line integrated sensor structure. The proposed method is a nondestructive, novel and alternative method to sense wastewater quality by benefiting their electrical characteristics diversity.

3.4.1. Design of the DSRR based Sensor

The proposed sensor structure has been designed with respect to DSRR type MTM as shown in Figure 3.37. The DSRR based sensor structure has a transmission line to observe transmitted power at resonance frequency. The sensor structure has an equivalent RLC circuit diagram. A mutual coupling have occurred between inductive parts of DSRR and transmission line. Hence, applied signal via the transmission line interact with the DSRR. Variations in the capacitive parts especially in the sensing layer created in the split gaps of the DSRR manipulates the signal power and resonance frequency. The samples placed to the sensing layer directly affect the overall capacitance due to electrical characteristics. Hereby, the resonance frequency at minimum transmission coefficient changes from these capacitive diversity.

The FR4 type dielectric material has been used as substrate. The copper type metal has been chosen for resonator and transmission line parts. Back of the structure is also covered by the copper metal. Two discrete ports have been added both ends of the transmission line to monitor transmitted power and resonance frequency as shown in Figure 3.37(b). The sensing layers have been created in the split gaps of the DSRR. The study is numerically achieved by using CST Microwave Studio software.

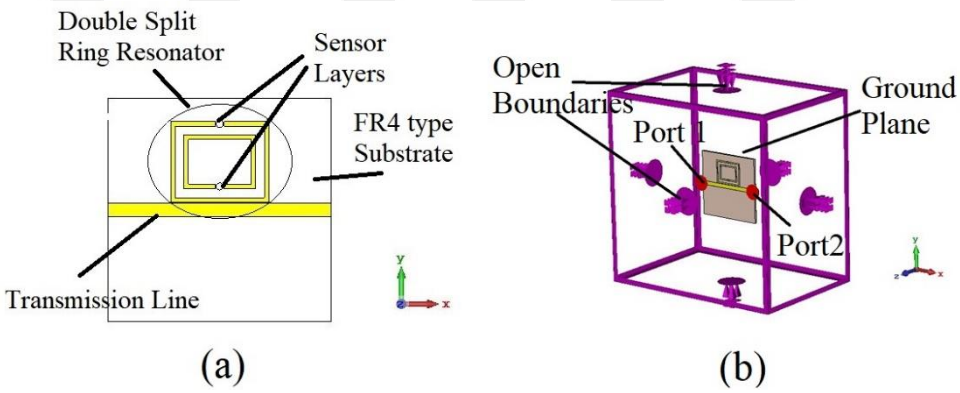

Figure 3.37. (a) Design and (b) simulation setup view of the sensor

3.4.2. Wastewater Quality Sensing Application of the DSRR based Sensor

The sensing application has been performed with three samples in different phase of the wastewater treatment facility. These phases are output, ventilation and backreturn. The electrical properties of them have been measured at between the 1.5 GHz and 2 GHz by using a dielectric probe kit as shown in Figure 3.38. Dielectric constant values for the output, back return and ventilation phases have monitored around 79, 77 and 43, respectively as illustrated in Figure 3.38(a). The dielectric loss values are observed around 10.5, 10.2 and 6 for the output, back return and ventilation phases, respectively as demonstrated in Figure 3.38(b). In the output phases, the sample has a dielectric characteristic like clean water as expected.

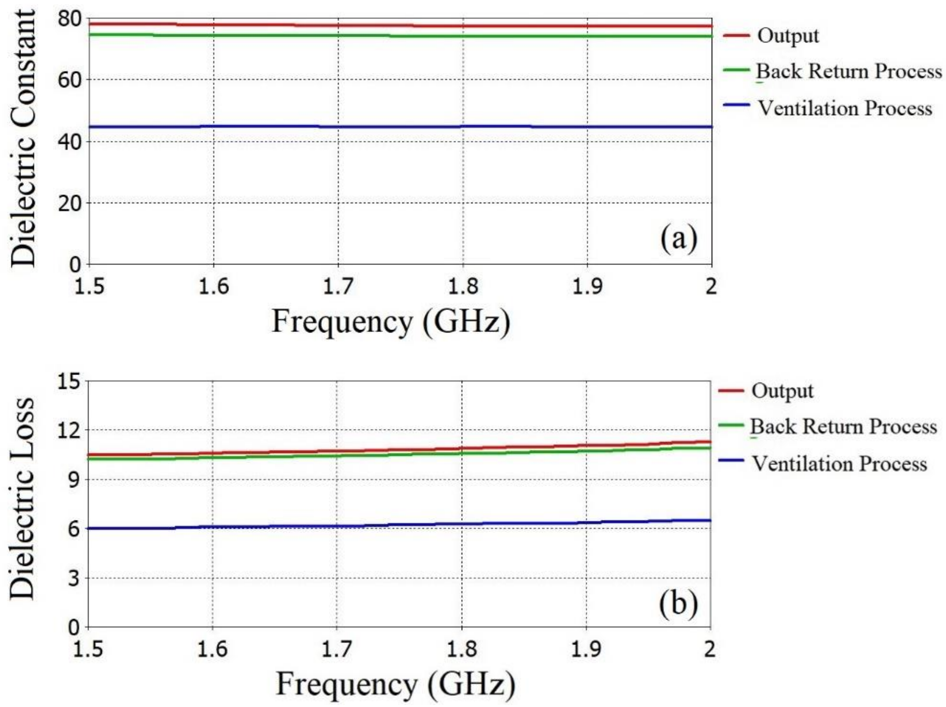

Figure 3.38. (a) Dielectric constant and (b) dielectric loss values for the output, back return and ventilation phases

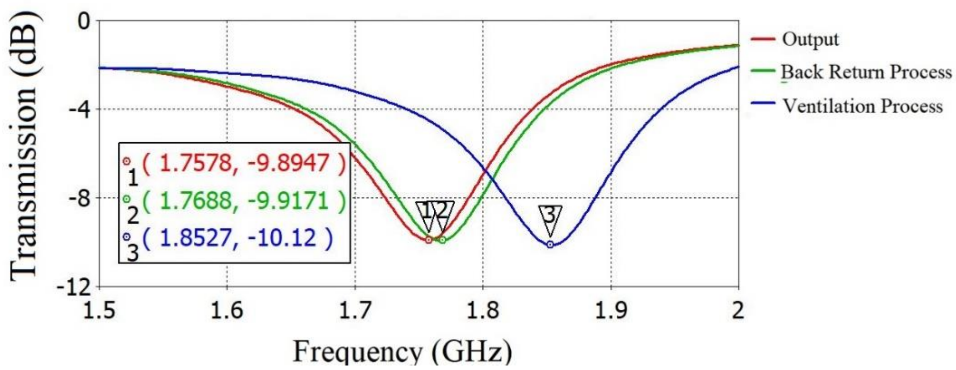

Figure 3.39. Numerical transmission coefficient results in output, back return and ventilation phases for proposed sensor structure

After the measurement of the electrical characteristics of the samples, the data files have been imported to simulation medium. The wastewater quality sensing study has been then realized by varying sensing layer of the DSRR based structure with respect to these electrical characteristics in numerical. Transmission coefficient results have been calculated as illustrated in Figure 3.39. The transmission coefficient values are obtained for all samples as around-10 dB. The resonance frequencies at minimum transmitted power level have been monitored as 1.758 GHz, 1.769 GHz and 1.853 GHz for output, back return and ventilation process, respectively. It can be seen from the results that there is a linearity between the resonance frequency and permittivity values of the samples. Hence, the proposed DSRR based sensor structure is a strong candidate to detect the wastewater quality. In addition, the sensor structure has many advantages such as having non-destructive technique, safer and cheaper comparing the existing methods.

This section of the thesis study has been published in AIP Conference Proceedings. (doi.org/10.1063/1.5135409)

4. APPLICATIONS WITH WAVEGUIDE TECHNIQUE

In this chapter, three different sensor applications which are (i) permittivity and thickness sensing, (ii) fuel adulteration and lubricant oil quality detection, and (iii) engine lubricant oil quality sensing have been studied with X band waveguide implementation. The proposed sensor structures have been tested with various samples such as different dielectric substrate materials, authentic and inauthentic diesel and gasoline, transformer oil, engine lubricant etc.

4.1. Permittivity and Thickness Sensing Applications with the SMLR based Sensor

In this study, a sensor structure having MTM based split meander line resonator (SMLR) has been designed for permittivity and thickness sensing applications. The study has been applied both numerically and experimentally at X band frequency regime. The proposed sensor is suitable for any dielectric substrate having flat surface to sense electrical characteristic and thickness. Sensing applications have been achieved by observing frequency shifts in X band. The equivalent circuit diagram, real and imaginary impedance, electric field and surface current distribution of the SMLR have been examined for understanding working mechanism of the sensor structure. In addition, the parametric study has been performed to adjust optimum dimension parameters of the SMLR. The CST Microwave Studio and PNA-L Agilent VNA have been used for numerical and experimental studies, respectively. For the experimental studies, the WR90 type of adapters and an X band waveguide is also used to measure sensor ability at X band. The organization of the study includes the design and theory of SMLR, numerical analysis of resonator, experimental investigation, and comparison of both numerical and experimental results of the sensor.

4.1.1. Design and Theory of the SMLR based Sensor

The SMLR based sensor structure has been designed with respect to the exact dimensions of an X band waveguide as shown in Figure 4.1(a). Arlon AD350 type dielectric material has been chosen as substrate layer. AD350 has many advantages such as low loss, high availability, and high mechanical strength to obtain susceptible and durable sensing. The copper type metallic material has been used for the resonator part of the sensor. The backside of the sensor have been arranged as a sensing layer which the samples are placed to as illustrated in Figure 4.1(b). The backside of the sensor have been arranged as sensing layer which the sample is placed to as illustrated in Figure 4.1(b). The dimension parameters are split gap width *g*, resonator line width *w* and horizontal line width *Hline* which have the values of 1.40 mm, 0.525 mm and 10.80 mm, respectively as demonstrated in Figure 4.1 (a).

The operating frequency band for the SMLR based sensor has been arranged X band. The dimensions of the resonator have been estimated by considering the quarter wavelength of the center frequency of X band.

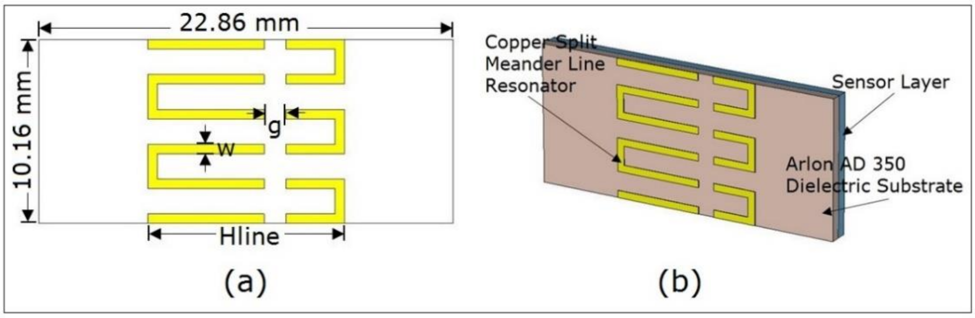

Figure 4.1. (a) Dimensions of the SMLR and (b) general view of the sensor structure

The equivalent circuit diagram of the SMLR based sensor structure has been examined in Figure 4.2. The resonator part of the sensor structure is divided into three parts as illustrated in Figure 4.2(a). These parts are named as arm, bridge and gap. The arm and bridge part of the SMLR creates inductive effects and total inductance stem from total arm and bridge length is equivalent inductance. The bridge parts in between two sequential horizontal lines have also capacitive effect. Gap parts along with split lines create a capacitive effect. Besides this, the sample placed on the sensing layer has a capacitance value according to its variable electrical characteristics. This capacitance value is changed by the electrical variations of the samples which can be represented in Eq. (2.1). Therefore, the total capacitance value of the sensor depends on dielectric constant and dielectric loss factor of the samples given in Eq. (2.2). The total capacitance can be written in Eq. (2.3);

Monitoring of the resonance frequency points was achieved to determine sensing behavior of the proposed structure. Therefore, the resonance frequency can be presented in Eq. (2.6). The resonance frequency only depends on the electrical characteristics of the sample placed on the sensing layer of the sensor structure in Eq. (2.6). Besides this, equivalent impedance of the structure can be expressed as Eq. (2.7).

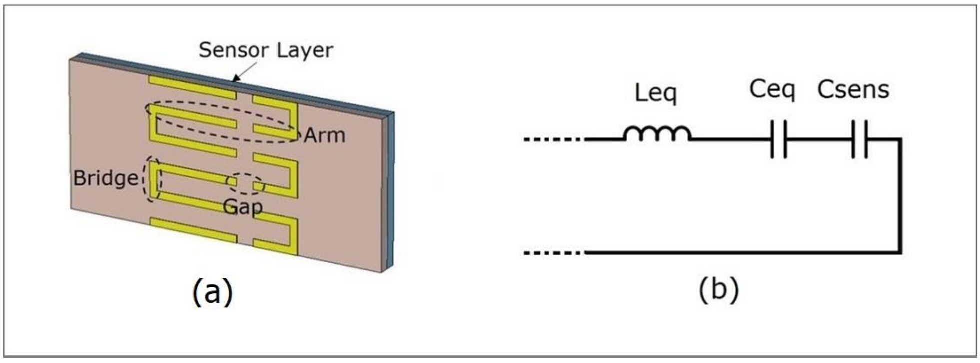

Figure 4.2. (a) Inductive and capacitive parts of the SMLR and (b) simplified equivalent circuit diagram of the sensor

The impedance matching is one of the important parameters for the waveguide technique based applications. It is numerically proved between free space and the proposed structure as shown in Figure 4.3. The impedance of free space is given in Eq. (2.8).

The reflection formulation between these two medium can be written in Eq. (2.9). $R(\omega)$ approaches zero while the impedance of the structure ($Z_{eq}(\omega)$) is almost equal to free space impedance (Z_0). This relation can be seen in Figure 4.3. The reflection magnitude is near zero at 10.20 GHz which is the resonance frequency of the structure while the real impedance value reaches its maximum level. In addition, the imaginary impedance is almost zero at the resonance frequency as shown in Figure 4.3.

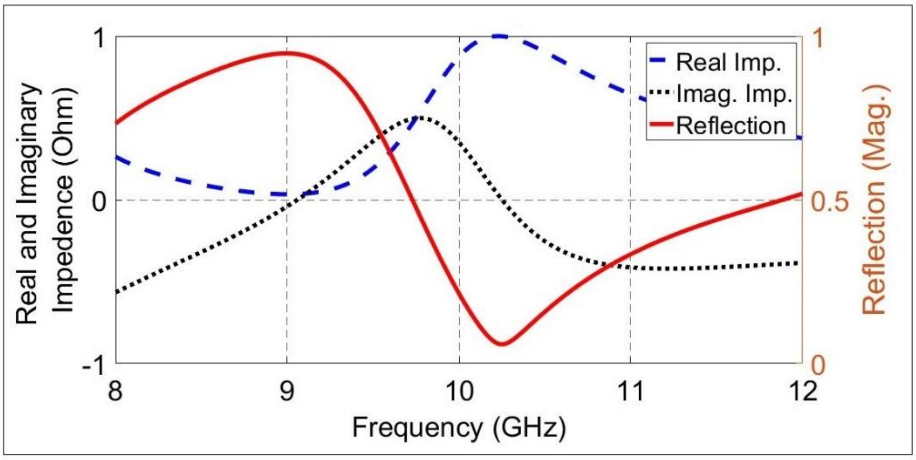

Figure 4.3. Normalized real and imaginary impedance and reflection magnitude of the proposed sensor

The electric field and surface current distributions for the sensor structure have been numerically studied in Figure 4.4. In general, the electric fields and surface currents are distributed in capacitive and inductive parts of the system. The electric fields have concentrated on the split gaps and sequential bridge intervals of the resonator as demonstrated in Figure 4.4(a). These part has also explained as capacitive parts before. The surface currents have focused on inductive parts such as arm and bridge length illustrated in Figure 4.4(b). In addition, the surface current flows in the opposite direction of the incident electric field. It can be concluded that the resonator resists against the electric field by acting as a negative inductance. This means that the proposed SMLR behaves like a left handed material or MTM.

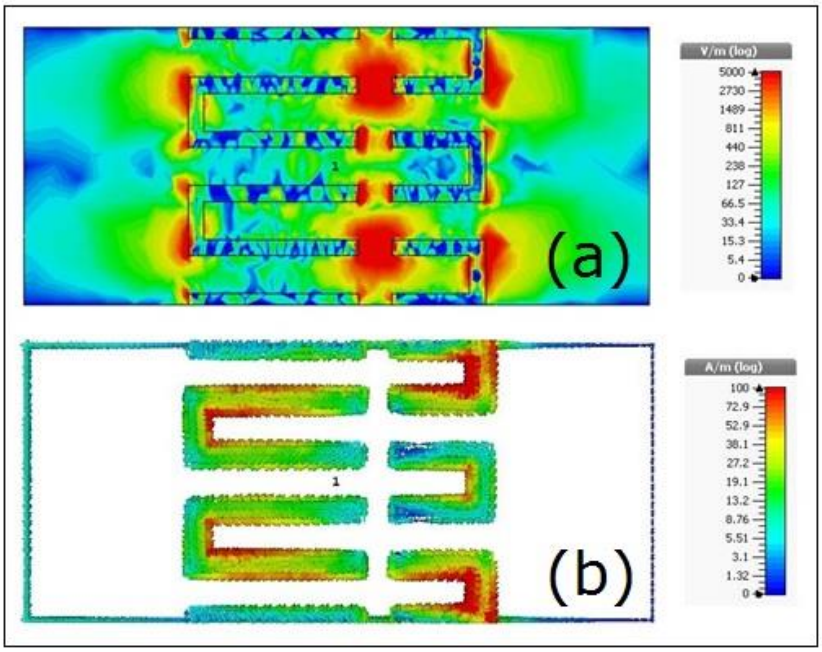

Figure 4.4. (a) Electric field and (b) surface current distributions of the SMLR based sensor structure

4.1.2. Numerical Studies of the SMLR based Sensor

In this part, numerical studies have been conducted by using CST Microwave Studio software program. The numerical setup for proposed sensor structure is illustrated in Figure 4.5. The perfect electric conductor (PEC) conditions have been arranged along with the x- and y- directions as demonstrated in Figure 4.5. The z- direction is setup as open boundary conditions. These boundary conditions have corresponded to the X band waveguide boundary conditions. Hence, the mode of the applied electromagnetic wave is determined as transverse electric (TE). In the numerical studies, only one port which is resonator side has been added since the study is just focused on reflected signal.

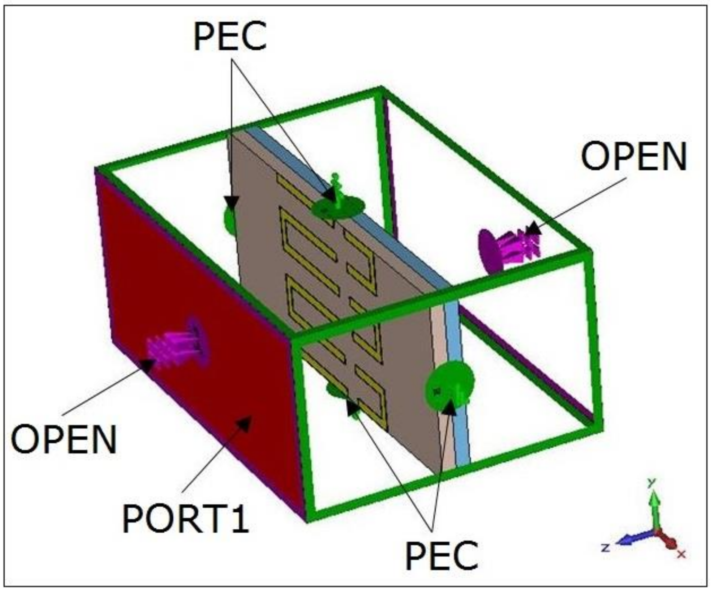

Figure 4.5. Numerical setup for SMLR based sensor structure

The parametric study for dimensions of the SMLR has been numerically conducted as illustrated in Figure 4.6. The split gap width parameter g, horizontal line width parameter Hline and the horizontal positions of the split gaps have been investigated. These parameters have been examined with respect to impact on the resonance frequency, reflection magnitude and equivalent circuit diagram.

Firstly, the split gap width parameter has been examined by increasing the *g* from 0.8 mm to 1.6 mm with 0.2 mm steps in each phases. While the *g* increasing, the resonance frequency point is increasing from 9.75 GHz to 10.25 GHz approximately as demonstrated in Figure 4.6(a). Besides this, the reflection magnitude is also increased with the increment of the split gap width. Hence the optimum value for *g* is chosen as 1.4 mm.

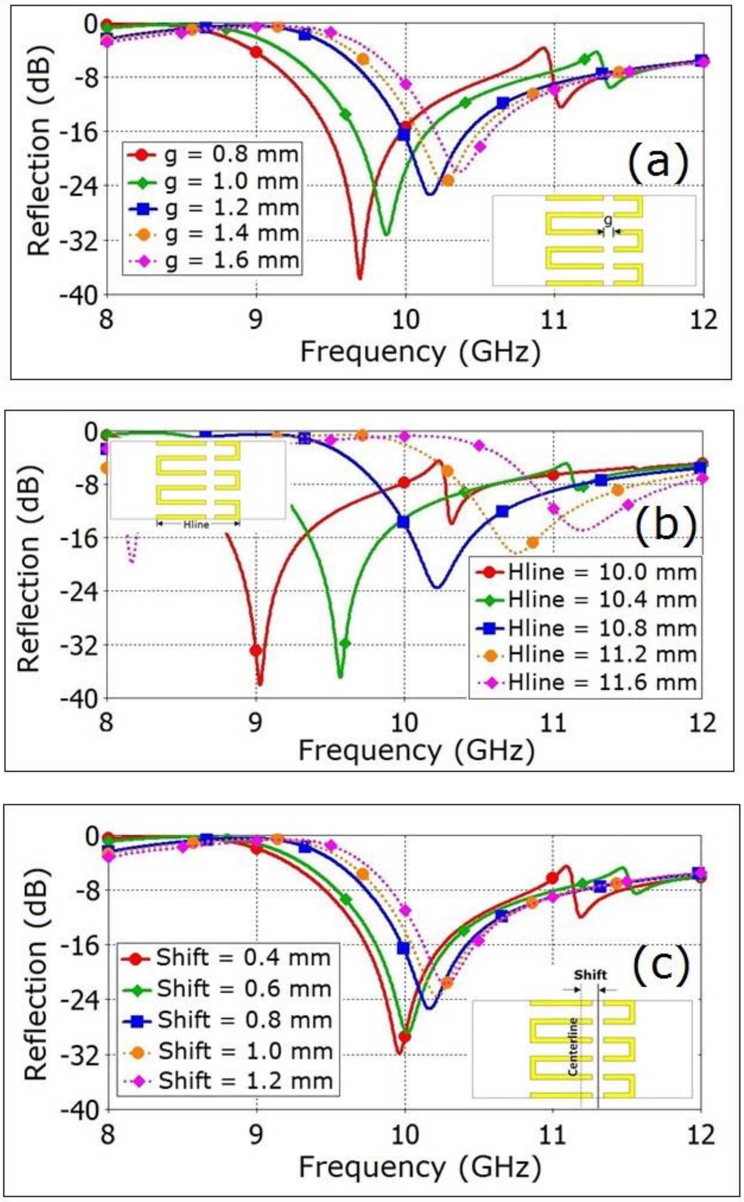

Figure 4.6. The parametric studies of the proposed SMLR; (a) split gap width parameter (*g*), (b) the horizontal line width parameter (*Hline*) and (c) the horizontal positions of the split gaps (*Shift*)

Secondly, horizontal line width parameter has been analyzed by varying the *Hline* value from 10.0 mm to 11.6 with 0.4 mm steps in each phases. While the *Hline* increasing, the resonance frequency point is increasing from 9 GHz to 10.8 GHz approximately as shown in Figure 4.6(b). Moreover, the reflection coefficient is also increased with the increment of the horizontal line width. This behavior of the *Hline* parameter is similar with the split gap width parameter. The horizontal line width parameter value has been chosen as 10.8 mm.

Lastly, the effect of the horizontal position of the split gaps of SMLR has been observed by changing its distance from centerline. The *shift* parameter has been varied from 0.4 mm to 1.2 mm with 0.2 mm steps in each phases as illustrated in Figure 4.6(c).

The resonance frequency of the sensor structure and the reflection coefficient are increasing while the position of the split gaps is moving away from the centerline. These variations in the resonance frequency and reflected power originated from the interaction between the capacitive effects of the split line gap and its position. Therefore, the resonance frequency point f_0 demonstrated in Eq. (2.6) effected from this diversity which causes different C_t values expressed in Eq. (2.3).

Table 4.1 Dielectric characteristics for different Arlon type dielectric substrates

	AD270	**AD300**	**AD320**	**AD350**	**AR450**	**AR600**
Dielectric Constant (ε)	2.70	3.00	3.20	3.50	4.50	6.00
Loss Tangent ($\tan(\delta)$)	0.0023	0.0030	0.0038	0.0030	0.0035	0.0035
Resonance Frequency (GHz)	9.816	9.632	9.544	9.424	9.192	8.868

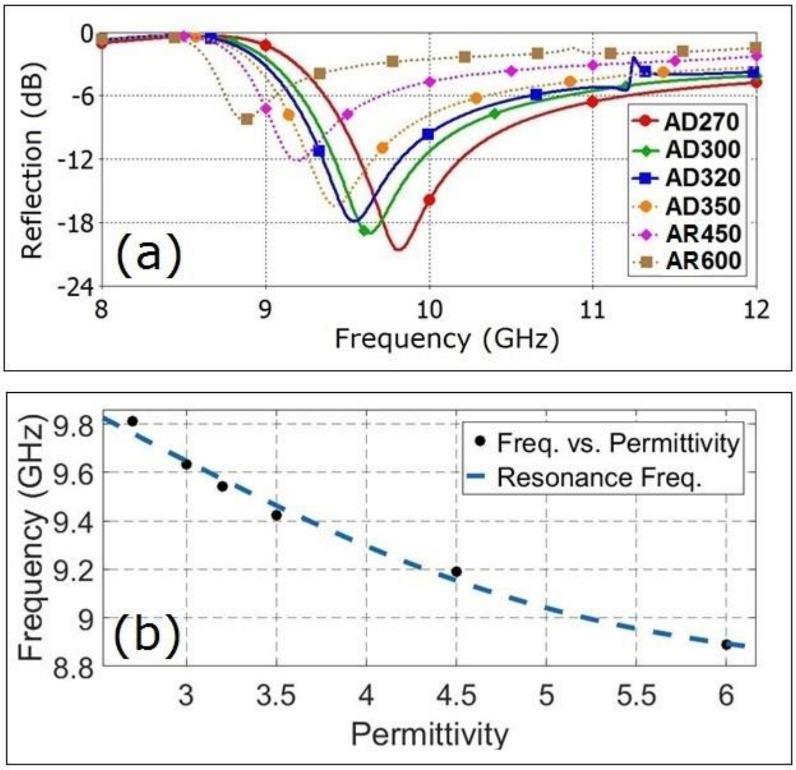

Figure 4.7. (a) The permittivity sensing study and (b) linearity graph for Arlon type dielectric substrates

The first permittivity sensing study has been numerically achieved by using Arlon type dielectric substrates with different electrical characteristics. The dielectric values for AD270, AD300, AD320, AD350, AD450, and AD600 are tabulated in Table 4.1 with respect to dielectric constant and loss tangent. The sensing layer thickness (Lt) has been keep constant as 1.52 mm for all type of numerical samples to monitor only effect of electrical characteristics. The capacitive effect of the sensing layer has been increased with the increment of the dielectric constant of the sample. As it can be seen in Figure 4.7(a), while the capacitive effect is increasing, the resonance frequency point is reducing with respect to Eq. (4.2). The reflected power is affected directly proportional from the increment of capacitance value of the sensing layer. The linearity graph has also examined for

Arlon type samples as demonstrated in Figure 4.7(b). It is concluded that the sensor structure detects the permittivity value of the Arlon type samples which is placed in sensing layer by observing minimum reflection magnitude or resonance frequency point of SMLR.

Table 4.2. Dielectric characteristics for different Rogers type dielectric substrates

	RO3010	**RO3006**	**RO3035**	**RO3003**	**RT5870**	**RT5880**
Dielectric Constant (ε)	10.20	6.15	3.50	3.00	2.33	1.96
Loss Tangent ($\tan(\delta)$)	0.0022	0.0020	0.0015	0.0010	0.0012	0.0019
Resonance Frequency (GHz)	9.240	9.736	10.464	10.584	10.816	10.894

The second permittivity sensing study has been realized for Rogers type dielectric substrates support first sensing study results with Arlon type samples as illustrated in Figure 4.8. The dielectric values for RO3010, RO3006, RO3035, RO3003, RT5870, and RT5880LZ are tabulated in Table 4.2 with respect to dielectric constant and loss tangent. The dielectric constant values of Rogers samples varied between 10.20 and 1.96 are wider than those from the previous permittivity study. The thickness of the Rogers dielectric substrates samples is chosen as 0.5 mm. It can be seen from the Figure 4.8(a) that the resonance frequency point is increasing and reflection magnitude of the sensor is reducing while the dielectric constant of the sensing layer is decreasing. Besides, the linearity graph is also investigated for Rogers type samples as illustrated in Figure 4.8(b). The linearity graph is obtained by applying curve fitting method with a polynomial function. It can be concluded that the results give almost a linear response.

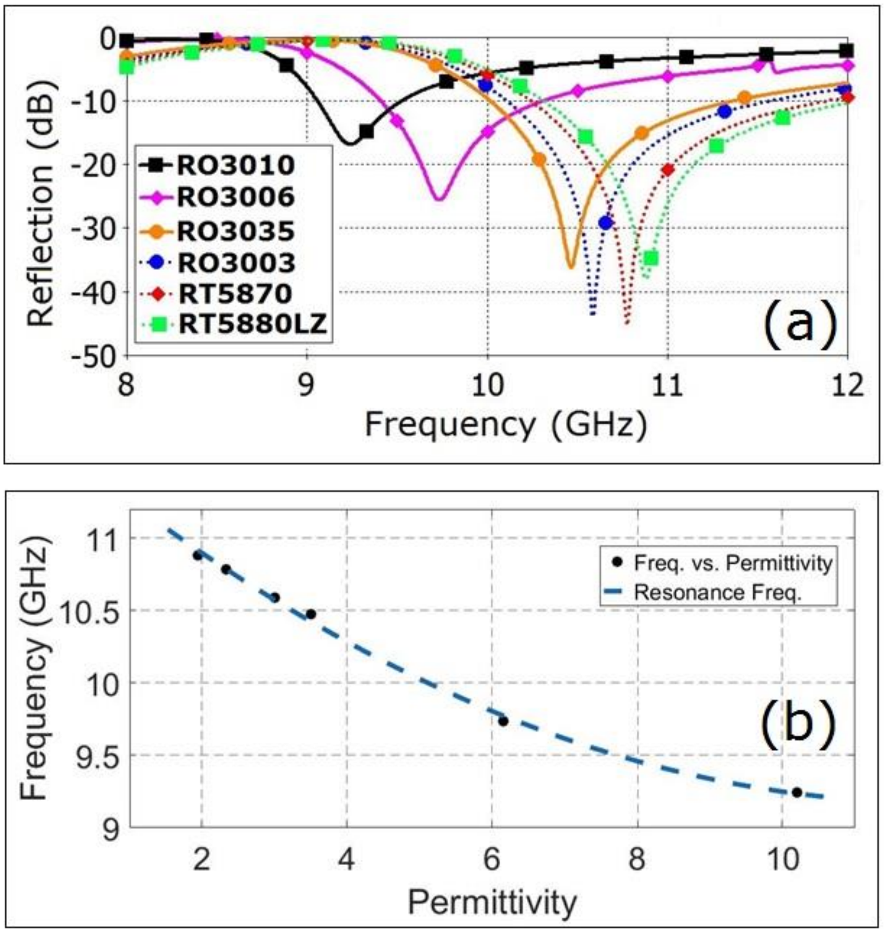

Figure 4.8. (a) The permittivity sensing study and (b) linearity graph for Rogers type dielectric substrates

The third study has been performed to observe effect of the sensing layer thickness as illustrated in Figure 4.9. One of the Arlon AD350 and Rogers RO3035 dielectric substrates which has the same electrical characteristics has been chosen as a sample. The thickness of the substrates which is placed in the sensing layer is varied from 0.4 mm to 1.6 mm. Therefore, the study is only focused on the sensing layer thickness (Lt). The capacitance of the sensing layer is directly proportional the sensing layer thickness. The total capacitance of the sensor structure is inversely proportional with the resonance frequency. Hence the resonance frequency is reducing while the overall capacitance of the sensor structure is increasing or the sensing layer thickness is increasing as illustrated in Figure 4.9(a).

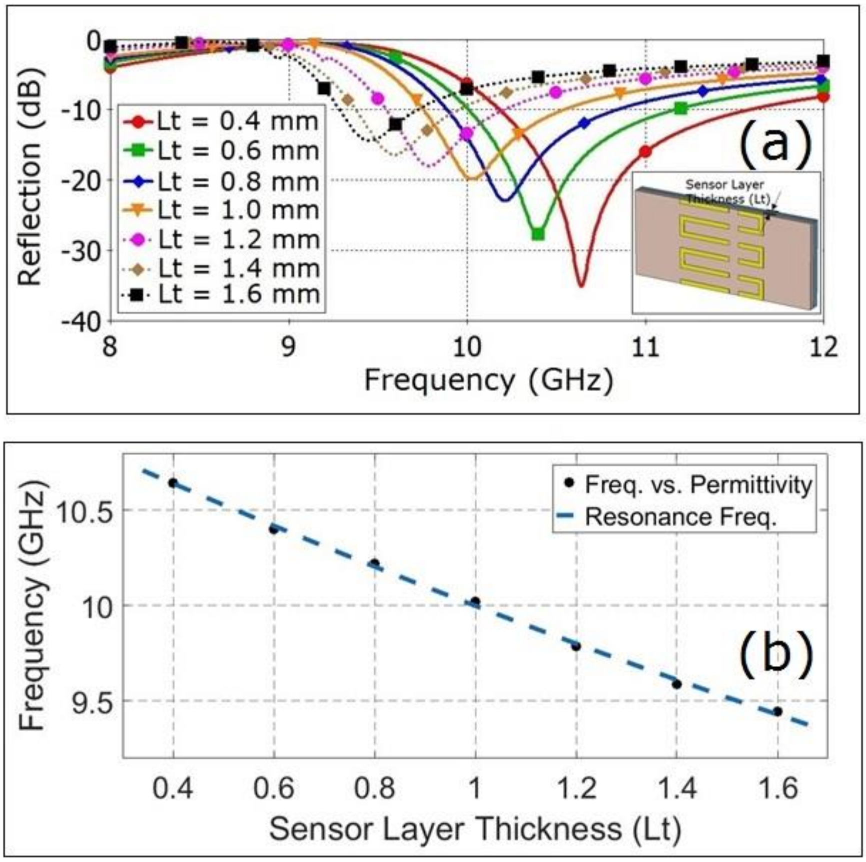

Figure 4.9. (a) The thickness sensing study and (b) linear response graph for both Arlon AD350 and Rogers RO3035 type dielectric substrates

The reflection magnitude is directly proportional with the sensing layer thickness. So, it can be said that the reflected power is increasing when the total capacitance of the sensor structure is increasing. Moreover, the resonance frequency point of the structure is inversely proportional to the sensing layer thickness as demonstrated in Figure 4.9(b). It is concluded that the SMLR based sensor can detect the thickness of any dielectric substrate sample with flat surface. The result shown in Figure 4.9 is achieved exactly the same for both Arlon AD350 and Rogers RO3035 with the same electrical properties. The reason is that the proposed structure is sensitive to the changes in the electrical properties of materials with the same dimensions. It can be concluded that these data are also valid for other substrates with the same dielectric constant characteristics.

Table 4.3 Dielectric characteristics for different type dielectric substrates

	AD350	**AR450**	**FR4**	**Di527**	**CuClad217**
Dielectric Constant (ε)	3.50	4.50	4.30	2.50	2.20
Loss Tangent ($\tan(\delta)$)	0.0030	0.0035	0.0025	0.0022	0.0009
Resonance Frequency (GHz)	10.220 (0.78 mm) 9.424 (1.52 mm)	9.192 (1.52 mm)	9.620 (1.00 mm)	10.780 (0.50mm) 10.160 (1.52mm)	10.838 (0.52 mm)

Lastly, different kind of dielectric substrate samples having various substrate thickness have been studied for observation the resonance frequency and reflection coefficient as shown in Figure 4.10. Electrical characteristics of the substrate samples (AD350, AR450, FR4, Di527, CuClad217) are tabulated in Table 4.3 with respect to dielectric constant and loss tangent value. It can be noted that all resonance frequency response results are in a good agreement comparing the other permittivity and thickness sensing studies given in Figures 4.7, 4.8, and 4.9. For example, the resonance frequencies responses for Di527and CuClad217 having almost the same thickness values are observed in a narrow frequency band due to similar electrical properties of them. Besides, these resonance frequencies are obtained in order to the magnitude of the dielectric constant of the substrate samples.

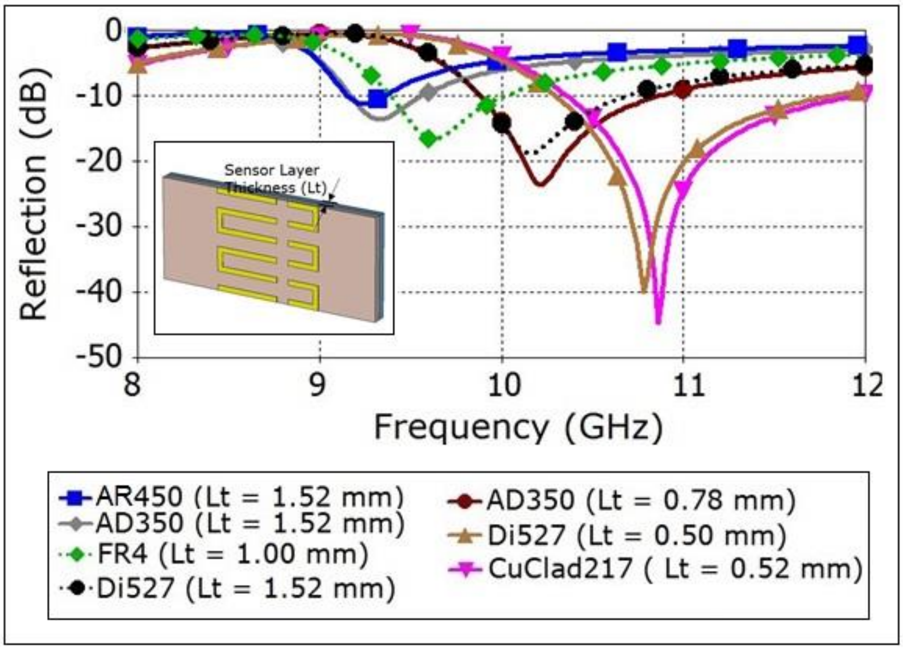

Figure 4.10. The resonance frequencies of the sensor structure for different kind of dielectric substrate with different sensor layer thicknesses

4.1.3. Experimental Studies of the SMLR based Sensor

The experimental studies for permittivity and thickness studies have been conducted by using PNA-L Agilent VNA. The experimental setup with two WR90 wave guide adapters, X band waveguide, sample holder and the sensor structure has been illustrated in Figure 4.11. The sensor structure shown in Figure 4.11(b) is produced by a PCB prototyping machine and it is embedded to the sample holder together with the sample. Different type of dielectric substrate samples which are AD350 with 0.78 mm of thickness, AD350 with 1.52 mm of thickness, AR450 with 1.52 mm of thickness, cu217 with 0.52 mm of thickness, di527 with 0.50 mm of thickness, di527 with 1.52 mm of thickness and FR4 with 1.00 mm of thickness are used in the experimental studies as shown in Fig. 4.11(c).

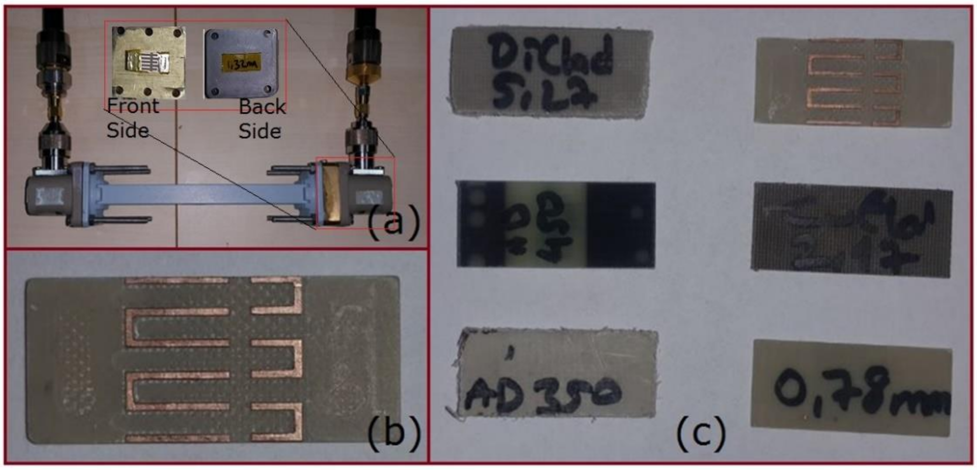

Figure 4.11. (a) Experimental setup, (b) manufactured sensor structure and (c) different kind of dielectric substrate samples

The thickness detection studies for Arlon type AD350 dielectric substrate samples have been realized both numerically and experimentally shown in Figure 4.12(a). There is about 200 MHz of frequency difference between the numerical and experimental results. This difference can be stem from the milling errors during the production process of the sensor structure and calibration errors of VNA during the measurement process. The resonance frequency point of the structure is decreasing and the reflection coefficient is increasing while the thickness of Arlon type AD350 dielectric substrate sample is increasing as illustrated in Figure 4.12(a). About 800 MHz of frequency difference corresponding 0.74 mm of thickness increment has been occurred both numerically and experimentally.

Arlon type AD350 and AD450 dielectric substrate samples having the same thickness value (1.52 mm) have been used for the permittivity detection study both numerically and experimentally as demonstrated in Figure 4.12(b). About 250 MHz resonance frequency difference corresponding the dielectric constant difference between them has been monitored for these samples both numerically and experimentally. Between these studies, an almost -5 dB difference in reflection coefficient is obtained. It is concluded that the proposed sensor structure can determine the thickness and permittivity values for Arlon type dielectric substrate samples.

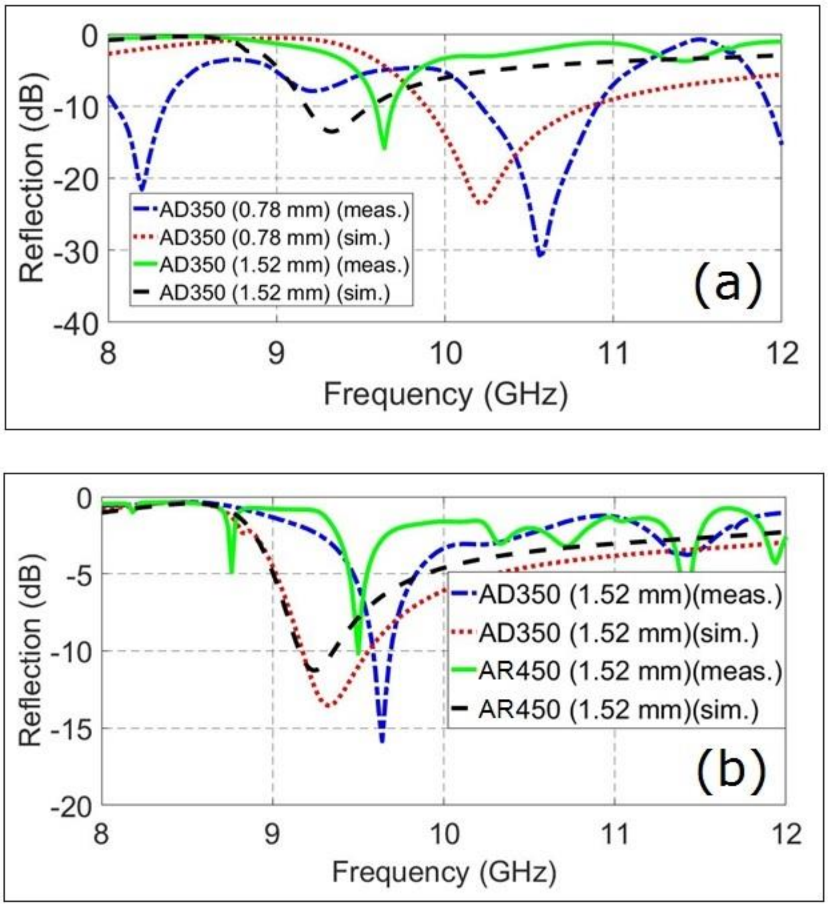

Figure 4.12. (a) Thickness and (b) permittivity sensing plots for Arlon type AD350 and AD450 dielectric substrates both numerically and experimentally

Another permittivity thickness study has been realized by using Arlon type of cu217 and di527 dielectric substrate samples with a 2.20 and 2.50 of dielectric constant, respectively. The 25 MHz of frequency difference corresponding to the 0.30 dielectric constant difference both numerically and experimentally as shown in Figure 4.13(b). The reflected power almost remains at the same level for both results.

The frequency difference and distortions are originated from non-perfect laboratory conditions and fabrication defects as mentioned before.

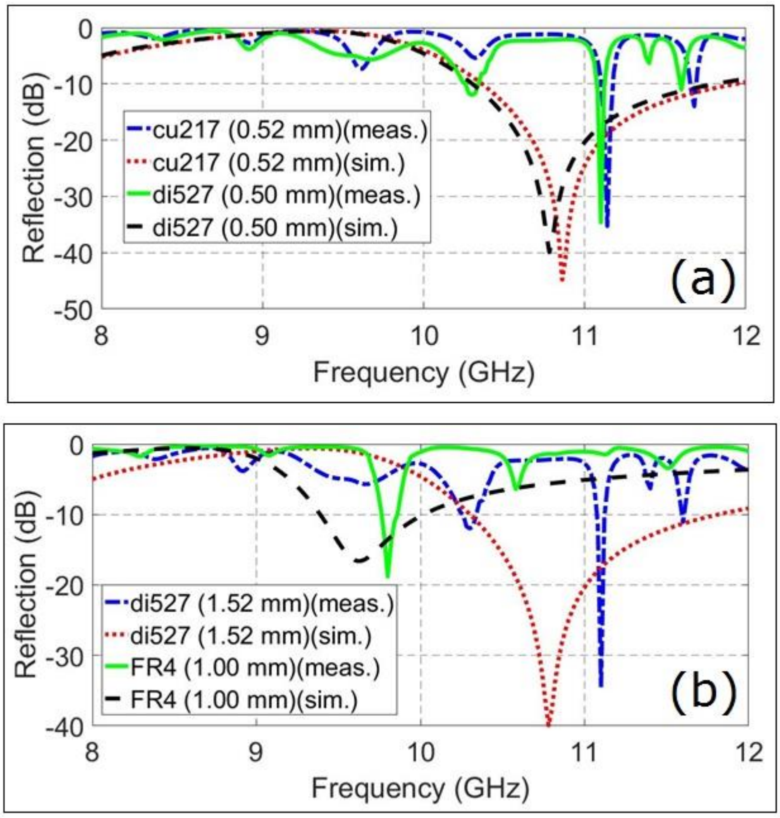

Figure 4.13. (a) Permittivity and (b) thickness sensing plots for Arlon type cu217, di527 and FR4 dielectric substrates both numerically and experimentally

Lastly, di527 and FR4 dielectric substrate samples have been performed for thickness sensing study as plotted in Figure 4.13(b). The numerical and experimental results are in a good agreement. The frequency shifts between the measured and simulated data for di527 and FR4 samples are 320MHz and 270MHz, respectively. The error ratios in the experimental results are at the same level considering the other researches in literature [Sabah et al., 2014; Tümkaya et al., 2017; Rahman et al., 2018]. Besides this, the reason why the measured curves have multiple peaks given in Figure 4.12 and 4.13 is the adhesive material effect which cannot been considered in simulations and the position of the sensor structure and sensing layer which is placed closely to the monopole side of waveguide adapter that results in near field effects and multiple sub wavelength signal radiation.

This section of the thesis study has been published in Journal of Electronic Materials. (doi.org/10.1007/s11664-018-6528-7)

4.2. Adulteration and Oil Quality Sensing Applications with OSR based Sensor

In this section, a MTM inspired omega-shaped resonator has been designed and implemented for adulteration and oil quality sensing applications both numerically and experimentally. The samples studied in this section are highly used in industry and they have very important role while utilizing from the industrial devices in energizing and lubrication phases. In addition, conditions and qualities of these materials is crucial issue to obtain maximum efficiency and minimum failure from the machines. The study covers adulteration detections of fuels (diesel and gasoline), lubricant quality, and transformer oil quality. The operating frequency range of the proposed sensor structure is X band. The sensor structure has been designed with respect to the X band waveguide dimensions to realize experimental studies inside the waveguide. Two WR90 type waveguide adapter and a sample holder has been used during the measurement process. The electrical characteristics of the samples have been examined with a dielectric probe kit at X band frequency regime. The results have been evaluated by comparing the numerical and experimental findings.

4.2.1. Design and Theory of the OSR based Sensor

The OSR based sensor structure has been designed numerically studied with FIT based CST Microwave Studio program. The full size of the sensor structure has been arranged corresponding the waveguide dimensions sizes as illustrated in Figure

4.14(a). Hence, the produced sensor structure can be easily implemented in an X band waveguide for experimental studies. The sensor has an FR4 type dielectric substrate The OSR is made from the copper type metal. Front and back sides of the sensor have OSR. The resonator have been designed by some parameters which are inner radius (r), line width (w), split gap width (g) and horizontal line width (*Hline*) as illustrated in Figure 4.14(a). The values of these parameters are 2.2 mm, 0.8 mm, 0.8 mm and 13 mm, respectively. The sensing layer thickness has been arranged as 10 mm as shown in Figure 4.14(b). This value is corresponded the sample holder thickness dimension using in experimental works.

The working frequency band for the OSR based sensor has been arranged X band. The dimensions of the resonator have been estimated by considering the quarter wavelength of the center frequency of X band.

The equivalent circuit diagram of the sensor structure has been examined to easily understand the working principle and the physical mechanism as shown in Figure 4.15. The OSR can be analyzed as three parts which are ring, horizontal arms and gap demonstrated in Figure 4.15(a). Basically, ring and horizontal arms have created inductive effects which can be defined as L_{ring} and L_{arm} respectively. The equivalent inductance (L_t) is the total of these inductive parts of the resonator.

The permittivity of the sample placed on the sensing layer can be expressed in Eq. (2.1). Hence the total capacitance (C_t) of the proposed structure is a function of the dielectric constant and dielectric loss of the sample loaded in the sensing layer given in Eq. (2.2).

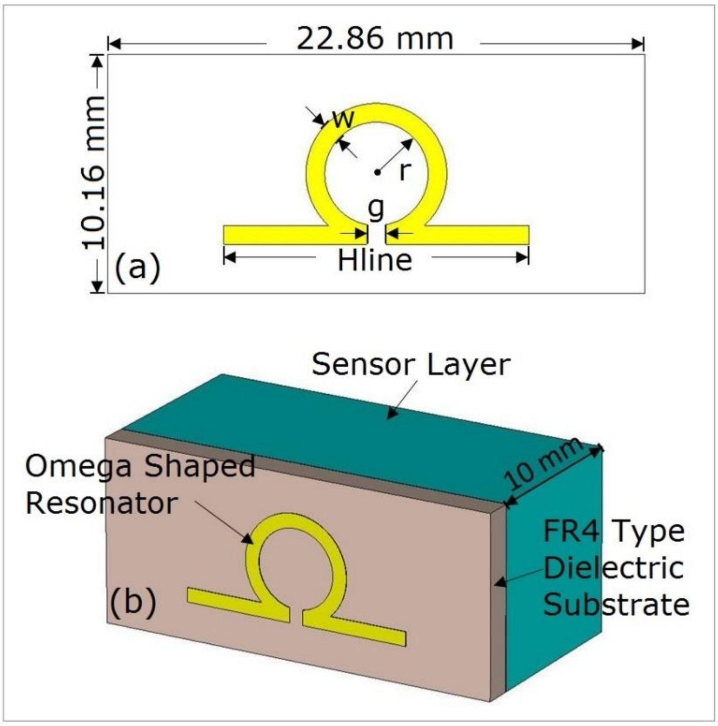

Figure 4.14. (a) The dimension parameters of the OSR and (b) general view of the sensor design

The equivalent circuit diagram of the sensor behaves like an RLC circuit shown in Figure 4.15(b) with mentioned circuit parameters. In addition to this, the sensing layer which can be changed with the different samples having different dielectric characteristics also generates additional capacitive effect as C_{sens}. Thus, the total capacitance C_t of the sensor can be expressed in Eq. (2.3).

The resonance frequency of the structure can be written in Eq. (2.6). Therefore, the sensing characteristics of the structure can be easily observed by the resonance frequency shifts.

Moreover, the equivalent impedance of the sensor can be written in Eq. (2.7). The impedance of free space is expressed in Eq. (2.8). The reflection calculation between these mediums can be represented in Eq. (2.9).

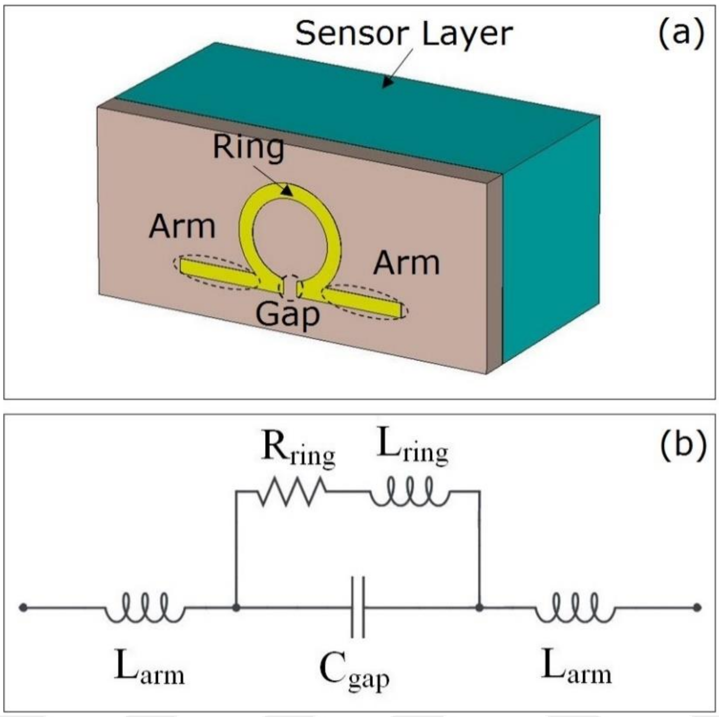

Figure 4.15. (a) Parts of the OSR based sensor structure and (b) equivalent circuit diagram of OSR

The impedance matching between the sensor and free space is numerically examined as illustrated in Figure 4.16. Considering the Eq. (2.9), while the impedance of the structure $Z_{eq}(\omega)$ approaches the impedance of the free space Z_0, the reflection $R(\omega)$ is approaches to zero. This relation can be seen in Figure 4.16. The refection magnitude is going to zero at the frequency of 11.70 GHz while the impedance of the structure is at maximum. Moreover, the imaginary part of the impedance of the structure is also zero and the transmission magnitude of the signal is at the maximum level at this frequency point.

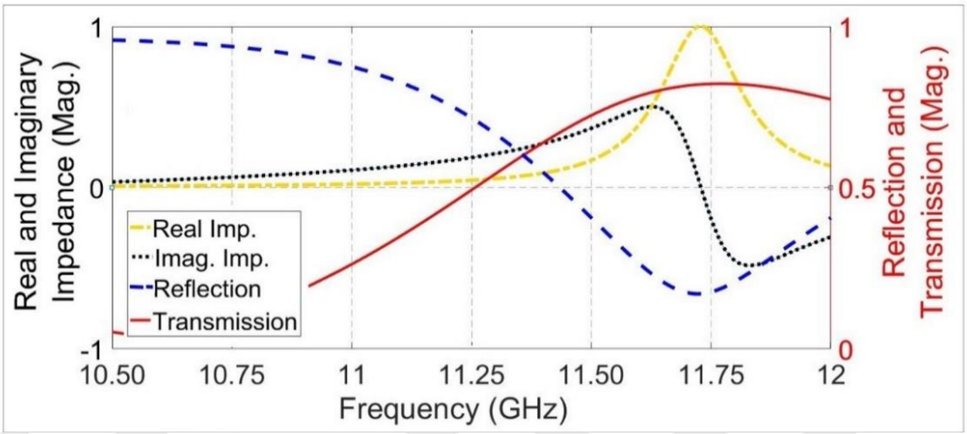

Figure 4.16. Normalized real impedance, imaginary impedance, reflection magnitude and transmission magnitude of the proposed structure

The relation between the impedance characteristics and maximum transmission ratio for the resonator has been explained the Figure 4.16. It can be concluded that the proposed resonator structure has the resonance frequency point at X band with respect to the maximum transmission ratio. On the other side, the study is focused on zero transmission ratios since the sensor structure has been sensitively discriminated of the samples at X band. Hence the electric field and surface current distribution of the sensor is numerically presented at operating frequency point of 9.85 GHz with zero transmission coefficient in Figure 4.17. The electric field is highly concentrated around the resonator part of the structure. Especially, it is located at the end of the horizontal arms and capacitive gap of the omega shaped resonator as shown in Figure 4.17(a). These concentrations can describe how the capacitive effects occur in the resonator part of the sensor structure. The surface current with opposite directions is driven by capacitive effects. It has occurred at both left and right horizontal inductive arm of the resonator with the opposite directions as shown in Figure 4.17(b). Hence, the zero transmission coefficient is obtained at the working frequency point of 9.85 GHz with these opposite surface currents.

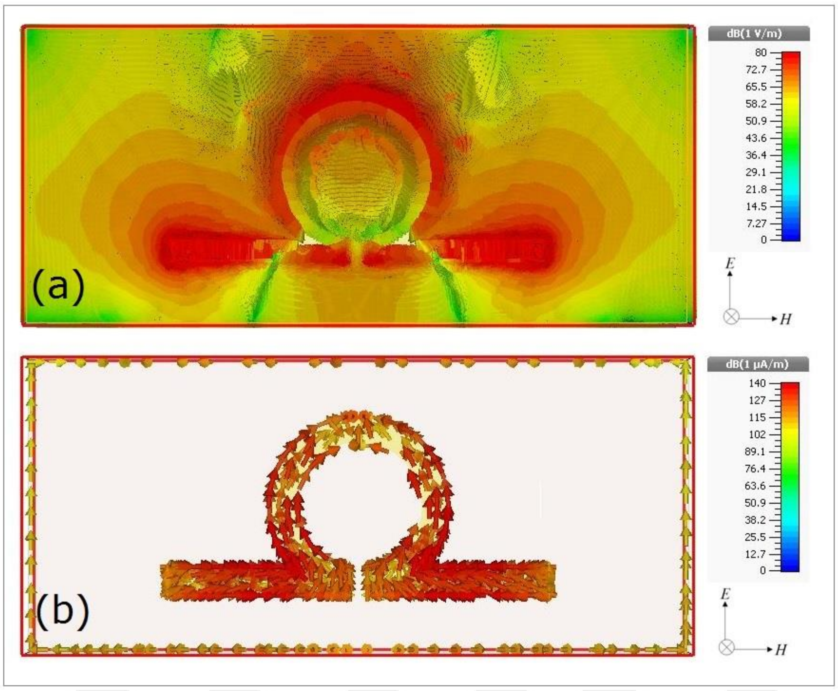

Figure 4.17. (a) Electric field and (b) surface current distribution of the proposed sensor at 9.85 GHz

4.2.2. Numerical and Experimental Setups for the OSR based Sensor

The numerical setup for sensor structure has been prepared by using FIT based CST Microwave Simulation software and it is illustrated in Figure 4.18. The OSR parts are placed to both front and back side of the dielectric layer. The sensing layer having a thickness of 10 mm which correspond to sample holder used in experimental studies has been arranged along the z direction. Two waveguide ports have been inserted to the front and back side of the structure to observe the transmitted power level. The reference planes are set with respect to both end plane of the structure. The operating frequency range has arranged as X band which corresponds to frequency range between 8 GHz – 12 GHz. The boundary conditions are set to the perfect electric conductor (PEC) along x- and y-axis which corresponds to waveguide boundary conditions as shown in Figure 4.18. The z-axis has determined as propagation direction.

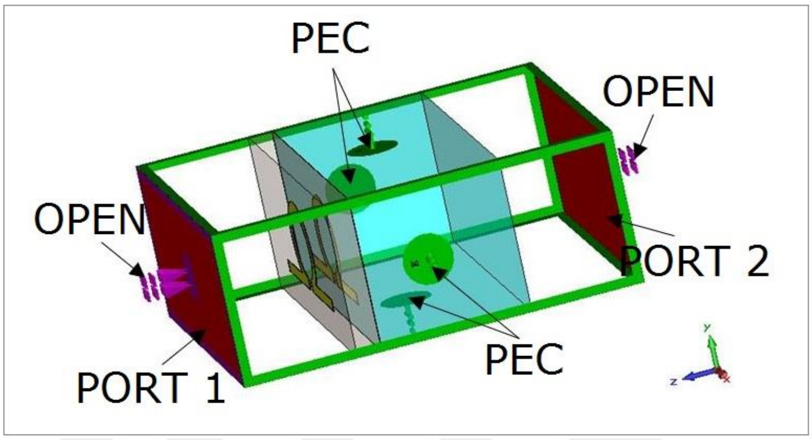

Figure 4.18. Numerical setup for OSR based sensor

The parametric studies have been achieved to monitor the effects of the dimensions of the resonator on the resonance frequency and transmission coefficient of the structure as demonstrated in Figure 4.19. The dimension parameters which are called as split gap width (*g*), line width (*w*) and horizontal line width (*Hline*) have been investigated by changing their values with certain ranges. The effect of the split gap width parameter (*g*) is observed between 0.9 mm and 0.7 mm by decreasing 0.1 mm in Figure 4.19(a). The resonance frequency is increasing when the split gap width is decreased. The variation is linearly observed about with 20 MHz increments. The transmission coefficient value has been remain at same level for all values of g. The resonance frequency is dramatically affected by the line width parameter (*w*). Parameter value of the *w* is changed from 1.0 mm to 0.2 mm by decreasing 0.2 mm as illustrated in Figure 4.19(b). It has been monitored that the line width parameter is decreasing once the resonance frequency is decreasing. This decrement has changed linearly about 180 MHz. The transmitted power level is increasing with the increment of the line width value.

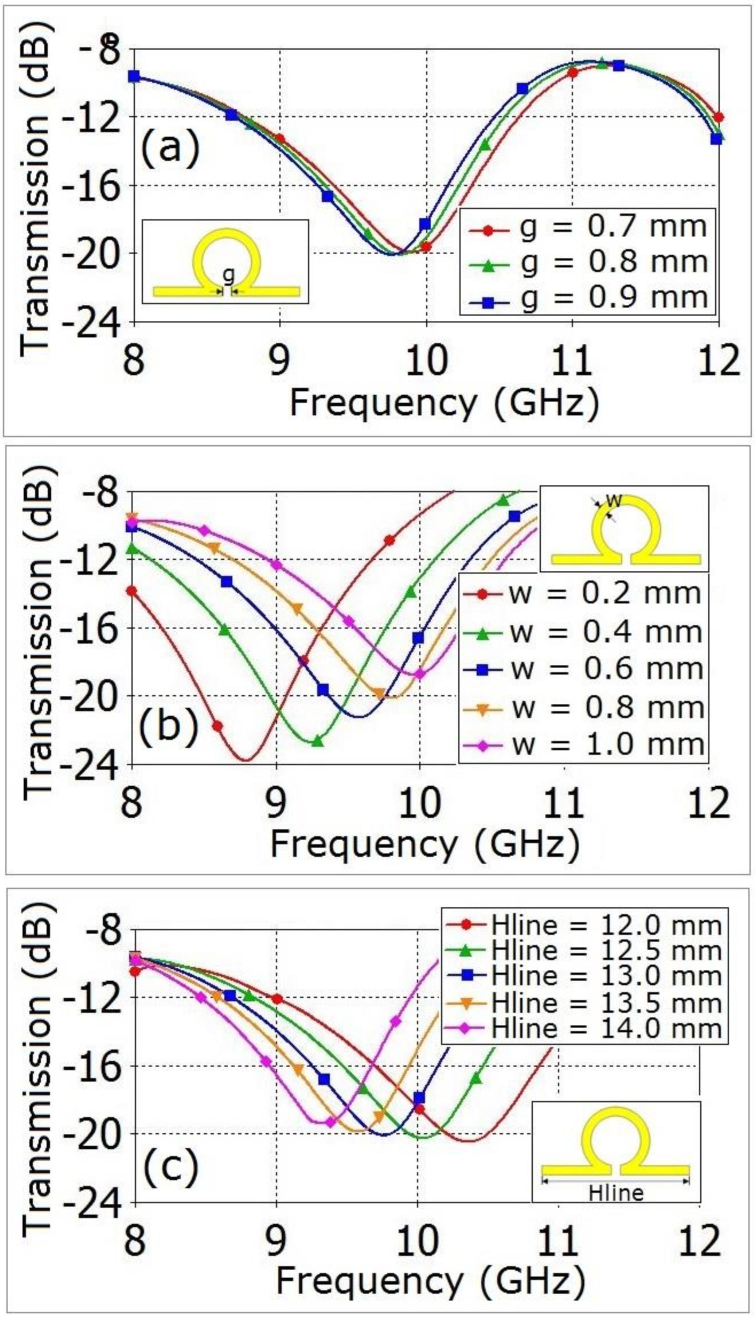

Figure 4.19. The parametric study for OSR based sensor structure; (a) split gap width parameter (*g*), (b) line width parameter *(w*) and (c) horizontal line width parameter (*Hline*)

Finally, the horizontal line width (*Hline*) parameter has been investigated between 14.0 mm to 12.0 mm by decreasing 0.5 mm at every phase. The variation of the resonance frequency has observed as about 160 MHz of increment for each step. The transmission coefficient has been barely affected of variation of the *Hline* value. It is concluded that the resonance frequency and transmission coefficient of the structure is highly affected by the resonator dimensions especially split gap width parameter.

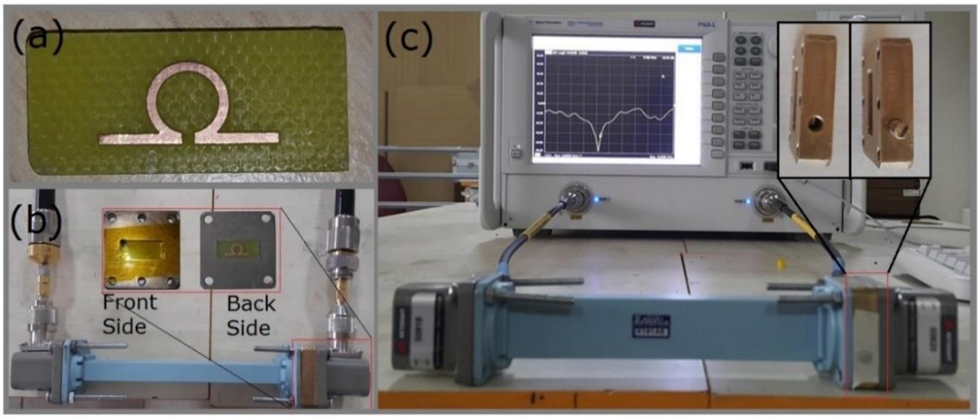

Figure 4.20. (a) Produced sensor structure, (b) waveguide configuration and (c) experimental setup

The proposed structure is manufactured by using a CNC based PCB prototyping machine. The fabricated sensor structure is illustrated in Figure 4.20(a). Experimental studies have been achieved with an X-band waveguide, two WR90 waveguide adapters and a proper sample holder as shown in Figure 4.20(b). The sample holder with a 10 mm of thickness dimension is loaded with the liquid sample at every measurement phase and it is placed to the front side of the waveguide. The produces sensor has embedded to the waveguide adapter coincided with the sample holder as shown in Figure 4.20(b). After the configuration, the waveguide setup has been connected to PNA-L Agilent VNA. The operating frequency range is arranged between 8 GHz to 12 GHz. An open ended coaxial probe has been used to detect the dielectric properties of the liquid samples. The experimental setup has been prepared and the transmission coefficient has been measured with the waveguide, adapters, sensor structure and liquid sample holder as shown in Figure 4.20. The liquid sample is firstly loaded by an injector via the channel placed in the top side inside the sample holder as shown in Figure 4.20(c). After that, the transmission coefficient is measured and in the same way, the sample is discharged from the holder. This method is applied for each measurement steps of the liquid samples.

4.2.3. Gasoline Sample Distinguishing Application of the OSR based Sensor

Gasoline is one of the highly used energy sources by many countries. The producer companies or governments are added to their own additives to mark the fuels. However, the unmarked gasoline fuels are sold by illegal ways as tax free. Hence, the purpose of this study is to solve this problem by distinguishing the authentic and inauthentic gasoline samples from each other.

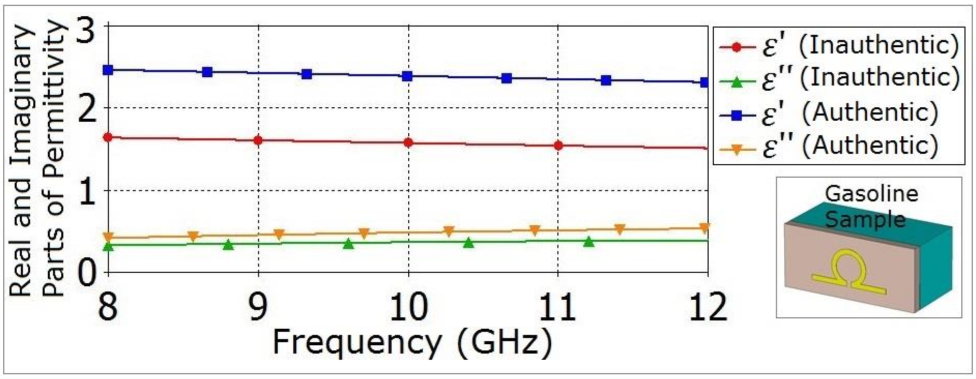

Figure 4.21. Dielectric constant and dielectric loss values of the authentic and inauthentic gasoline samples at X-band

The dielectric characteristics of the authentic and inauthentic samples are monitored between the 8 GHz and 12 GHz as demonstrated in Figure 4.21. Clear discrimination has been monitored between the samples. The dielectric constant values of the authentic gasoline samples and inauthentic gasoline samples are about

2.4 and 1.75, respectively. The dielectric loss values of them are about 0.45 and 0.40, respectively. The differences in the dielectric characteristics of these two samples are clearly seen in Figure 4.21.

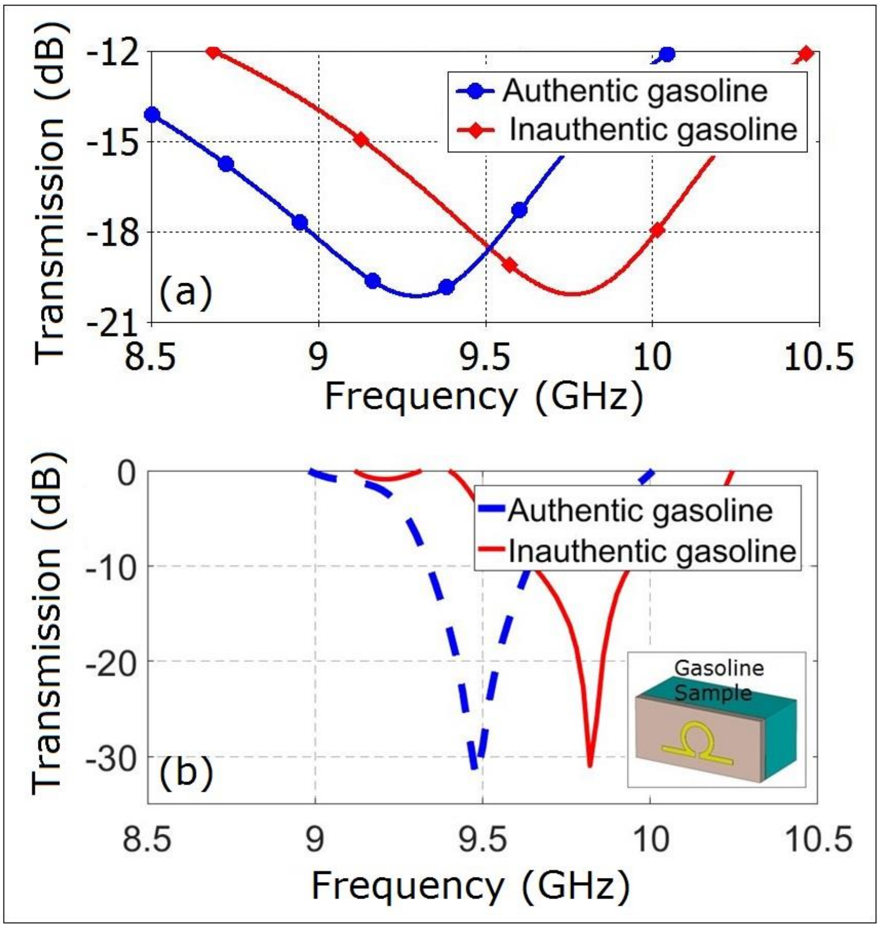

Figure 4.22. (a) Numerical and (b) experimental study plots for authentic and inauthentic gasoline samples

After the dielectric property determining study, the samples are defined in the CST Microwave simulation software as new materials. The numerical studies are realized by placing these materials into the sensing layer. The transmission coefficients for authentic and inauthentic gasoline samples are observed between 8.5

GHz and 10.5 GHz as shown in Figure 4.22(a). The resonance frequencies for authentic and inauthentic samples are 9.364 GHz and 9.772 GHz, respectively. About 408 MHz of frequency shift is obtained between these two resonance frequency points. The measured results for the authentic and inauthentic gasoline samples is shown in Figure 4.22(b). The measured resonance frequency points are monitored at 9.486 GHz and 9.847 GHz, respectively. The resonance frequency difference between these two frequency points is 361 MHz experimentally. It can be seen from Figure 4.22 that the simulated and measured results are in a good agreement and the proposed sensor structure is capable of discriminating the authentic and inauthentic gasoline samples from each other.

4.2.4. Diesel Sample Distinguishing Application of the OSR based Sensor

The other highly preferred fossil fuel as an energy source is diesel. This fuel (like gasoline) is an important commercial tool for international companies. To detection the inauthentic diesel is a crucial duty for the governments. This unbranded fuels also poses a great danger for the users with respect to engine healthiness. Hence, the authentic and inauthentic diesel sample distinguishing study is realized by using the proposed sensor structure.

The electrical properties of the authentic and inauthentic diesel samples are tested at the X-band frequency regime by using a dielectric probe kit as shown in Figure 4.23. At the frequency range of 8 GHz - 12 GHz, the dielectric constant value for authentic diesel sample is between 2.79 and 2.52, and for inauthentic diesel sample is between 2.46 and 2.18. The dielectric loss values are almost at the same values for the samples as illustrated in Figure 4.23.

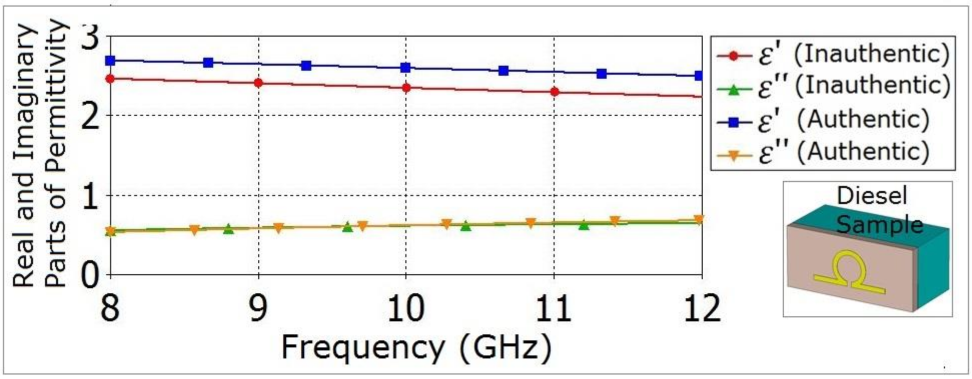

Figure 4.23. Dielectric constant and dielectric loss values of the authentic and inauthentic diesel samples at X-band.

The numerical and experimental studies to distinguish the authentic and inauthentic diesel samples are presented in Figure 4.24. The results are sketched at between the 8.5 GHz and 10.5 GHz. In the simulation studies, the lowest transmission coefficients are observed at the frequency points of 9.119 GHz and 9.311 GHz for authentic and inauthentic diesel samples, respectively as shown in Figure 4.24(a). As to experimental studies, mentioned lowest transmissions are monitored at the frequency points of 9.496 GHz and 9.669 GHz, respectively as shown in Figure 4.24(b). The frequency difference between the authentic and inauthentic diesel samples is 192 MHz in numerical and 173 MHz in experimental. The numerical and experimental studies of the sensor structure for diesel samples are given almost the same response except about the resonance frequency shift of 350 MHz. Hence, it can be concluded that the proposed sensor structure can be sensitively distinguished the authentic and inauthentic diesel samples from each other.

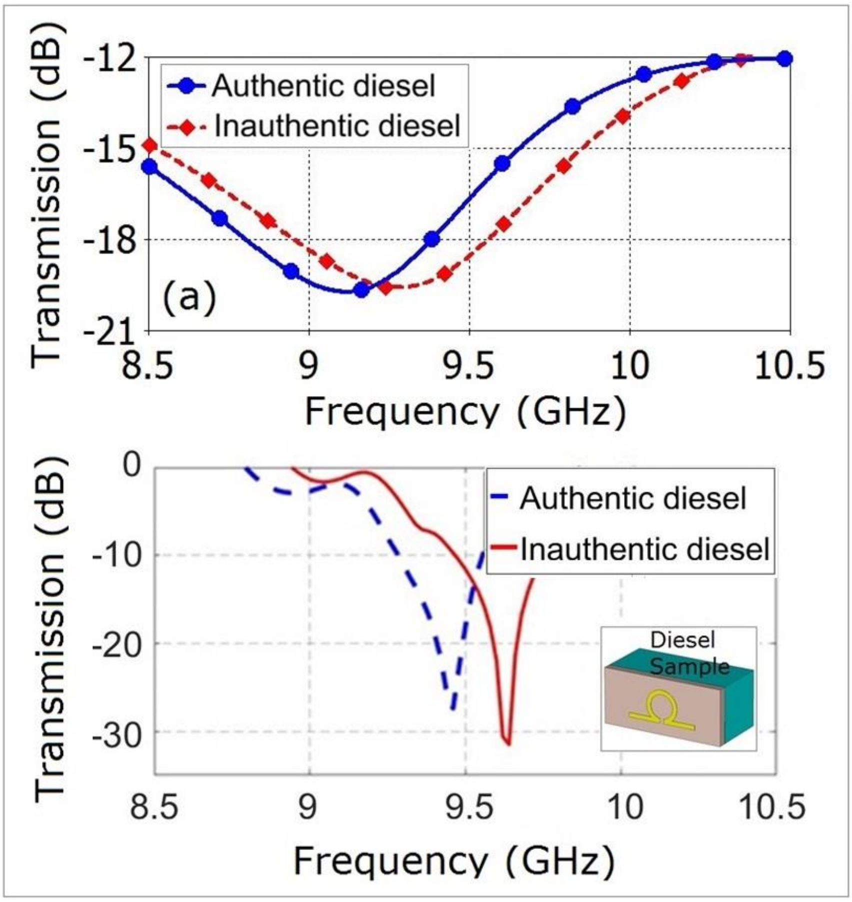

Figure 4.24. (a) Numerical and (b) experimental study plots for authentic and inauthentic diesel samples

4.2.5. Lubricant Sample Quality Detection Application of the OSR based Sensor

In this part, the lubricant samples which are used in the mechanisms such as engine systems, robotic machines, mechanics etc. have been investigated. It is very important to detect the machine or engine failures originated from the lube oil for safety and cost. Therefore, this section of the study has been focused on the discrimination between the clean and waste lubricant sample. The lubricant samples have taken from the machines which are operated in hydraulic systems. The electrical characteristics of the clean and waste lubricant samples are measured at X-band by means of the dielectric probe as shown in Figure 4.25. The dielectric constant values and dielectric loss values for the clean and waste lubricant samples have been observed very closely. The dielectric constant values are between about 2.5 and 2.2. Dielectric loss values are between about 0.5 and 0.7 at X-band.

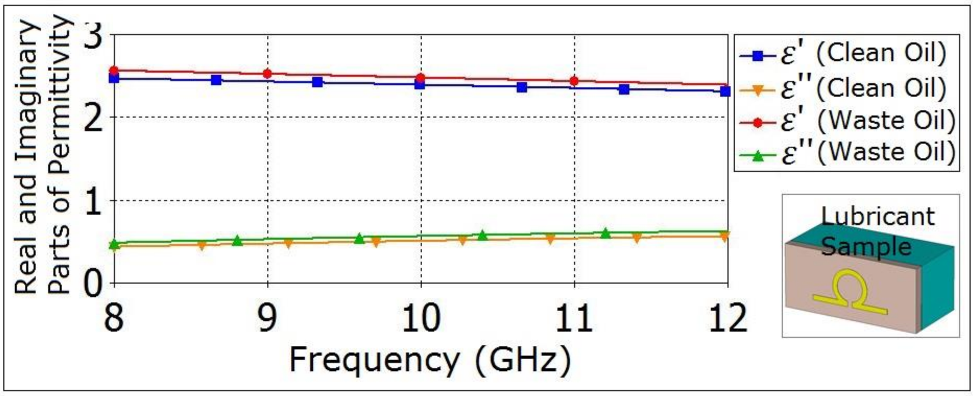

Figure 4.25. Dielectric constant and dielectric loss values of the clean and waste lubricant samples at X-band

It is hard to discriminate the clean lubricant sample from the waste oil since the dielectric properties of them is almost at the same. However, the proposed sensor structure has precisely detected of the quality of the oils. The numerical and experimental studies of the lubricant sample quality sensing are plotted in Figure 4.26. In the numerical studies. The minimum level of transmission is occurred at 9.257 GHz and 9.185 GHz for clean and waste oil, respectively. The lowest level of the transmission ratio in the experimental study is obtained at 9.502 GHz and 9.441 GHz for clean and waste oil, respectively. The frequency shifts are obtained as 72 MHz in simulation and 61 MHz in experimental. Although there is 200 MHz of frequency shift, the numerical and experimental results are in a good agreement such a detection study with very close electrical characteristics of the samples. Therefore, it can be said that the sensor structure is able to discriminate the clean and waste lubricant sample from each other, precisely and sensitively.

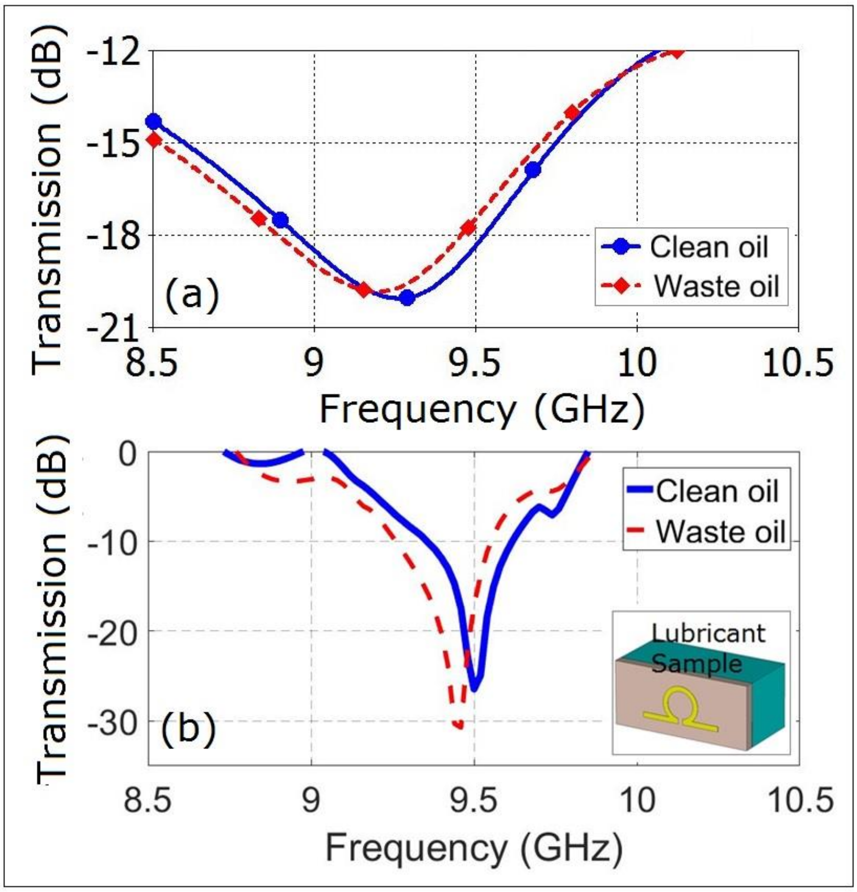

Figure 4.26. (a) Numerical and (b) experimental study plots for clean and waste lubricant samples

4.2.6. Transformer Oil Quality Detection Application of the OSR based Sensor

The last study is carried out for detection of the transformer oil quality at X-band both numerically and experimentally. Transformers have a key role in the industry for the utilization of electrical energy and controlling the energy flow. Thus, protection of the transformers is a very important topic for health and safety management and system failures.

In some type of transformers, special transformer oils are used for protection. Hence, this part of the study is focused on the transformer oil quality detection with clean and waste oils. The dielectric properties of the clean and waste transformer oil samples are measured at X-band regime as illustrated in Figure 4.27. The dielectric constant of the clean and waste oil samples are close to each other and they are about 2.9 and 2.7. The dielectric loss values of them are monitored at almost the same value which is about between 0.5 and 0.8. Hence, the dielectric constant parameter is the key to detect the quality of the transformer oil.

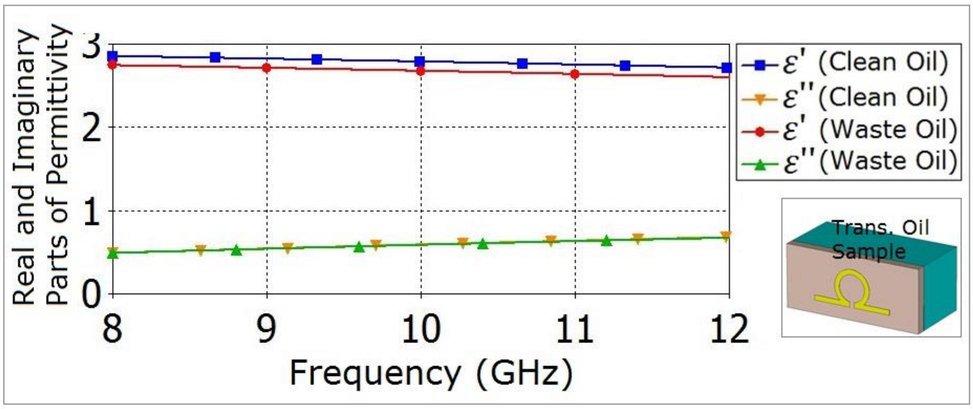

Figure 4.27. Dielectric constant and dielectric loss values of the clean and waste transformer oil samples at X-band

The numerical and experimental results for clean and waste transformer oils are plotted in Figure 15 between the frequencies of 8.5 GHz and 10.5 GHz. In the numerical studies, the lowest transmission coefficient values at this frequency range have been observed at the frequency points of 9.026 GHz and 9.103 GHz for clean and waste oil samples, respectively. The difference between these frequency points is 77 MHz as shown in Figure 4.28(a). In the experimental studies, these values have been monitored at the frequency points of 9.381 GHz and 9.446 GHz for clean and waste oil samples, respectively. The frequency shift between them is 65 MHz as demonstrated in Figure 4.28(b). The similar frequency shift (about 350 MHz) between the numerical and experimental results has occurred in the transformer oil quality study as well. However, the results are in a good agreement considering the frequency difference between the clean and waste oil. It can be concluded that the proposed structure can determine the transformer oil quality sensitively.

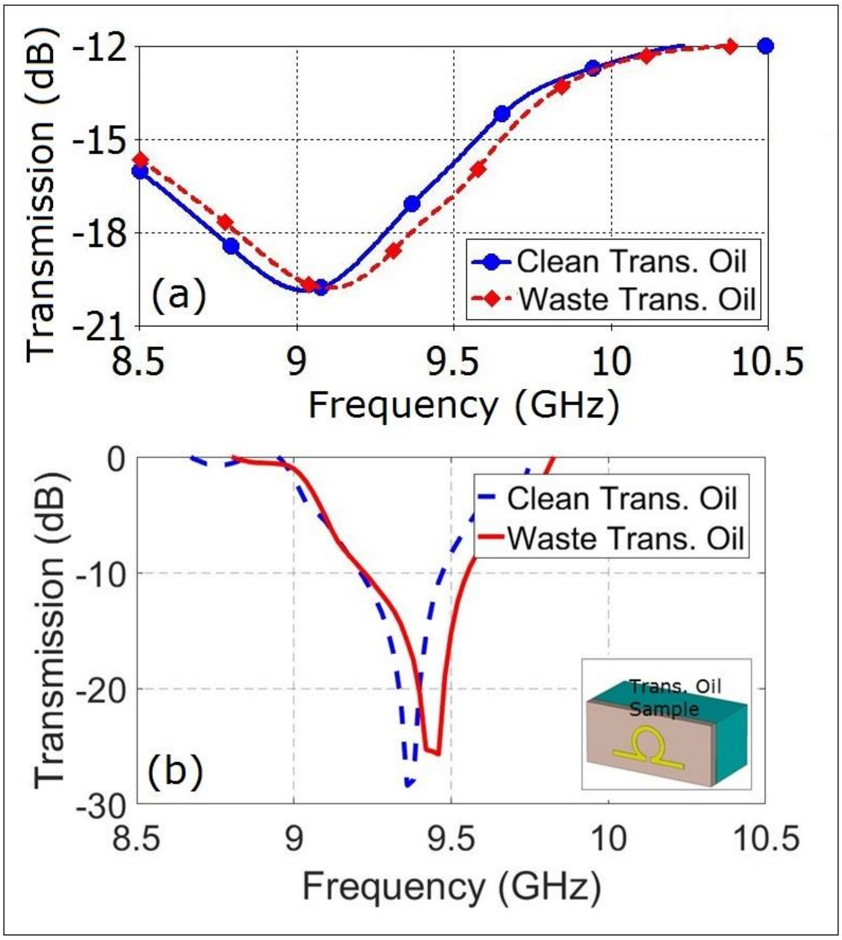

Figure 4.28. (a) Numerical and (b) experimental study plots for clean and waste transformer oil samples

This section of the thesis study has been published in Physica E: Low-dimensional Systems and Nanostructures. (doi.org/10.1016/j.physe.2019.113734)

4.3. Engine Lubricant Oil Quality Sensing Application

In this application, the electric LC type resonator has been designed at X band frequency regime for engine lube oil quality detection application. Two engine lubricant samples as clean and waste lubricant have been used. The electrical characteristics of the samples firstly measured by using a dielectric probe. After that the lubricant quality study has been realized by placing the sample to the sensing layer. Transmission coefficients are observed at near zero at the resonance frequencies. Finally, 100 MHz of resonance frequency difference are monitored between two lubricant samples. The sensor structure is a good candidate such an industrial application at microwave frequency regime.

4.3.1. Design of the LC Type Resonator based Sensor

The proposed sensor structure has been designed by inspiring the electrical LC resonator type. The resonator design consist of capacitive and inductive parts and it behaves like RLC circuit as shown in Figure 4.29(a). The FR4 type dielectric material has been used as substrate. The full wave commercial solver CST Microwave Studio simulation program has been used numerical studies. The numerical setup has been prepared by considering X band waveguide dimensions as illustrated in Figure 4.29 (b). Two waveguide ports are placed to the front and back side of the structure to monitor the transmission coefficient. The reference planes are set with respect to both end planes of the structure. The boundary conditions are set to the perfect electric conductor (PEC) along x- and y-axis which corresponds to waveguide boundary conditions. The z-axis has determined as propagation direction.

One of the important part of the sensor structure is sensing layer which is the part the samples placed. The sensing layer has been set to the back side of the resonator and it has a thickness of 10 mm which corresponds suitable waveguide sample holder in practical. This part affects the capacitive value of the structure by varying with the samples which have different electrical characteristics.

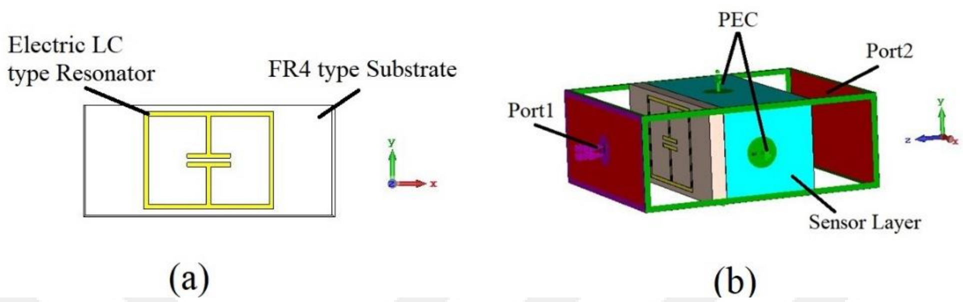

Figure 4.29. (a) Design and (b) numerical setup for the proposed sensor structure

4.3.2. Numerical Study of the LC Type Resonator based Sensor

The engine oil samples are firstly discriminated with respect to the electrical characteristics for detection application. The permittivity of the clean and waste engine lube oil is determined via an open-ended coaxial dielectric probe (performance probe type) connected to Agilent PNA-L VNA. The probe has been calibrated by air, water at 25°C and special short circuit kit. The dielectric probe is capable of measuring S-parameters for solids, semisolids (powder) and liquids. The permittivity values for the clean and waste oil are shown in Figure 4.30(a). The dielectric constant values are observed as about 2.35 and 2.45 for waste and clean oil samples, respectively. The dielectric constant difference between the clean and waste oil samples has been observed about 0.1.

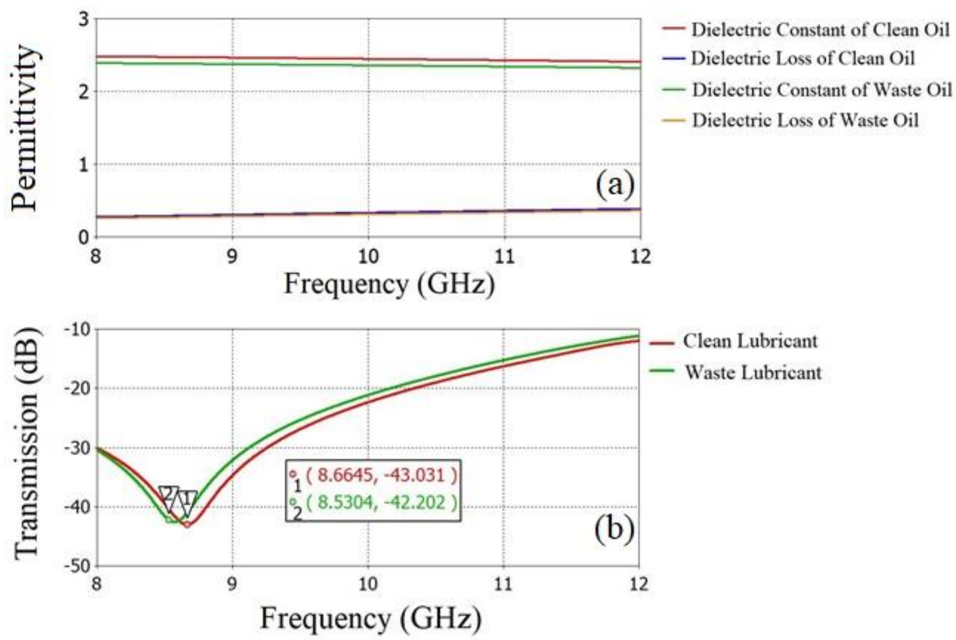

Figure 4.30. (a) Dielectric characteristics for the clean and waste oil samples and (b) engine oil quality detection study

The engine oil quality detection study has been numerically achieved at X band frequency regime. The clean and waste oil samples are placed on the sensing layer of the structure and the transmission coefficient has been monitored as demonstrated in Figure 4.30(b). The transmission coefficient for clean oil sample is obtained as -43 dB at 8.66 GHz and for the waste oil sample is obtained as -42 dB at 8.53 GHz. These coefficients corresponds to zero power transmission at that resonance frequency points. The difference between the resonances frequencies for the clean and waste oil samples has been monitored as 100 MHz. Hence, the proposed structure can be detect the engine oil qualities as clean and waste at X band frequency regime.

This section of the thesis study has been published in AIP Conference Proceedings. (doi.org/10.1063/1.5135408)

5. ANN APPROACH FOR LOCOMOTIVE MAINTENANCE

In this chapter, a novel technique has been introduced for determining engine malfunctions and qualities from engine lubricant samples, by eliminating the disadvantages of the spectral analysis method (SAM). This method is based on measuring the dielectric constant and loss factor of the engine lube oil samples. The particles which are mixed to the engine lube oil can be detected by obtaining dielectric characteristics at a certain frequency point or band. The aim of the study is to observe linear relationship between mentioned different amounts of particles with respect to the dielectric characteristics of the engine lubricant samples. Hence, the ANN method is used for monitoring the correlation between predicted and observed dielectric characteristics. Many ANN training algorithms such as Levenberg-Marquardt, Bayesian regularization and Quasi-Newton backpropagation can be used as the training model of weights. In this study, the Quasi-Newton backpropagation algorithm has been chosen due to providing close results with measurements.

The study is conducted at four different frequency points by adjusting the training and test data sets from lube oil samples of 33 locomotive engine systems. The dielectric characteristics of the lube oil samples are measured by a dielectric probe kit at four frequencies which are 2.40 GHz, 5.80 GHz, 7.40 GHz and 9.60 GHz. The dielectric characteristics of the lube oil can be affected from the particle variations inside the lube oil. Hence, this idea brings a novel approach for locomotive maintenance systems by observing the lube oil qualities. Moreover, sensor devices having real time response and low cost can be produced by using this new approach for the future works.

5.1. Spectral Analysis Method for Locomotive Maintenance

The study is focused on a spectral analysis device which determine diesel engine lubricant quality of the freight train by monitoring metallic particles inside the lube oil samples. The lubricant is affected from the failures of the locomotives, bad weather and rugged terrain conditions. The researchers have investigated the impact of the weather and environmental conditions such as low temperature on lubricant quality [Li et al, 2000; Bettol, 2010]. These unforeseen situations cause depreciation on mechanical parts of the locomotive engine system which has 2460 (A type), 1790 (Btype) or 1640 KW (C type). Every depreciated mechanical part leaves self-made particles into the engine lubricant. Therefore, spectral analysis method is applied for the lube oil samples to determine the rate and type of the particles mixed into the engine lubricant. For example, if the amount of chromium particles in the sample is above a certain level, it means that the chromium-plated piston liners of the locomotive engine are worn. Another example is that the high zinc level indicates corrosions in the motor bearings and galvanized metallic surfaces for 2460 KW and 1640 KW type of the locomotive engines. The engine system must be checked by taking dangerous level of mixed particles into the lube oil into consideration.

The manufacturer of the spectral analyzer (SA) is AMATEK and its model is SPECTROMAXx LMX05. Environmental conditions for the SA must be the temperature between 15-35°C and humidity under 80%. The Spectral Analysis can efficiently determine all important elements such as Fe, Al, Cu, Ni, Co, Ti, Mg, Zn, Sn and Pb in the metal industry. It is stabilized against the temperature fluctuations. The operating optical range of Spectral Analysis is between 140-670 nm and this range can be configured due to customer's application requirements.

Since the locomotives have very expensive engine systems, the method plays an important role in the maintenance phase. The mechanical failures, oil viscosity, filter life, fuel and water leak can easily be determined by this control mechanism. After analyzing the elements in lube oil, engine system problems are stabilized due to the critical level of detected element. Borderline of those mechanical particles in ppm and affected parts of the engine due to the observed material in lube oil are tabulated in Table 5.1.

Table 5.1. Borderline value, affected parts and recommended action for type A, B and C locomotive engines due to material in lube oil

Observed Material	Borderline (in ppm)	Affected parts in engine	Recommended Action
Iron (Fe)	125	Rings, liners, pistons	Check for rapid wear of rings and liners.
Aluminium (Al) and/or Silicon (Si)	5	Piston valves, rings, injectors, fuel	Check fuel cleanliness, injector calibration, tip erosion and notify fuel supplier. Check if piston rings are excessively worn.
Copper (Cu)	150	Bearings, bearing bushes, piston thrust washers	Measure the piston head clearance with lead readings to locate worn piston thrust washers. Check connecting rod bearing blade thrust faces for distress.
Lead (Pb)	75	Bearings, turbo charge bearings	Most likely lead flash is dissolving off bearings. Premature lead removal, before bearings are broken in, can lead to bearing distress, inspect and replace upper con rod bearings in service less than 6 months if lead flash has been removed from the unloaded area of the fish back bearing surface on turbocharged engines. If con rod bearings require replacement, wrist pin bearings should also be checked and replace if lead flash has been removed.
Zinc (Zn)	10	Lube oil additives, galvanized metallic surfaces	Check if oil is contacting with galvanized or zinc painted surface. Check if makeup oil in stock is within specifications. Notify lube oil supplier. Check for silver bearing failures.
Chromium (Cr)	20	Piston liners, blower bearings	Check for rapid wear of rings and liners.
Silicon (Si)	25	Sand dust soil contamination in engine parts	Improve air filter (maintenance is required)
In combination of Cu, Fe, Pb	Two out of three elements in borderline		Check for debris under crankshaft gear indicative of gear train bushing distress. Check idler gear bearing clearances. Check main and con rod bearings per maintenance manual.

Figure 5.1. A spectral analyzer

Zinc and copper borderline values are 500 ppm and 30 ppm for B and C locomotive engine type, respectively. The reason is that zinc oil is required for this type of engines. In addition, there is no excitation procedure for B type and this type of engines is monitored by following-up and making periodic maintenance. Table 5.1 has been created by the researchers utilizing the literature about the engine oils and automotive lubrication (Bartz, 2019).

For spectral analysis step, 33 oil samples are gathered from different locomotives and two sets of them are prepared to measure electrical and chemical characteristics. First 33 samples of different locomotives are used for spectral analysis tests of the elements and the second 33 samples are hold for analysis of electrical properties of oil under tests to investigate relationship between spectral and electrical analysis results. Table 5.2 shows the spectral analysis results (in ppm) for different lube oil samples. There are three types of engine with respect to the engine power in Table 5.2. Type A, B and C engines represent the engines with 2460, 1790 and 1640 kW of power, respectively. In addition, Type B engine needs a zinc-containing additive for lubrication as seen in Table 5.2 in column Zn. Iron (Fe), lead (Pb), aluminum (Al) levels in the samples are normal due to the critical reference value denoted in Table 5.1. The maintenance is required for some locomotive engines as the borderline is crossed for elements of Copper (Cu), Chromium (Cr) and Silicon (Si). Moreover, all engine lubricants and galvanized surface parts must be checked as the Zinc (Zn) level is high for almost all samples.

Table 5.2. Spectral analysis results for different locomotive engine lubricant samples

Engine Types	Locomotive No	Elements in Lube oil (in ppm)						
		Fe	Pb	Cu	Cr	Al	Si	Zn
A	A018	9	4	10	6	2	8	5
	A020	10	11	20	30	2	8	12
	A024	13	23	69	7	3	7	14
	A025	19	10	35	21	3	9	42
	A044	25	11	50	6	2	10	21
	A046	28	11	55	5	2	9	18
	A061	22	19	63	4	2	8	71
	A064	16	8	28	56	3	15	12
	A068	10	11	29	37	3	12	9
	A070	23	26	63	41	3	11	27
	A072	18	16	43	39	3	12	23
B	B116	32	5	16	4	2	14	656
	B133	25	5	13	9	2	14	633
	B155	25	5	9	2	2	16	681
	B180	49	7	10	6	2	14	603
	B188	16	2	5	3	1	8	647
	B202	120	9	66	18	4	11	605
	B236	81	5	15	5	2	14	580
	B268	41	5	14	3	2	9	668
	B279	43	9	19	4	2	10	621
	B281	34	5	19	11	2	15	668
	B310	53	6	15	2	2	12	729
	B337	72	9	26	9	3	12	607
	B348	63	4	5	2	1	12	645
	B358	10	6	8	3	2	2	692
	B369	31	8	17	2	2	8	697
	B381	102	7	72	14	3	16	718
	B386	35	7	19	3	2	7	650
	B395	42	10	27	4	3	10	601
C	C026	16	19	54	5	4	7	11
	C059	10	6	27	10	2	5	30
	C034	17	16	48	3	2	6	135
	C015	19	24	44	17	3	7	47

Although spectral analysis device provides reliable and detailed results as shown in Figure 5.1, it is very expensive, time consuming and non-real time technique. The sample gathering process from various locomotives takes time in this method. Besides, the locomotives can be far from the central station and maintenance center. The oil-samples are sent to the central laboratories for examination and it takes about a month to get the results. During this time period, the lube oil values of the locomotive engines can change due to time factor. Unfortunately, this localization problem increases the probability of failure in engine systems. Furthermore, this technique is costly and requires many human resources having special technical capacity.

With the new approach proposed in this study, it is aimed to determine the relationship between electrical properties and spectral characteristics of various lube oil as a substructure for future sensor devices that (i) can be integrated into the locomotive engines, (ii) can obtain real-time results, (iii) that are cheap and (iv) do not require human resources.

5.2. Dielectric Constant and Dielectric Loss Factor Measurement

Dielectric constant and loss factor measurement values for lube oil samples related to different locomotives are given in Table 5.3 at various frequency points of 2.40 GHz, 5.80 GHz, 7.40 GHz and 9.60 GHz. These frequency points are arbitrarily chosen to validate the relation between dielectric values and engine lubricant samples. The table refers that the dissipation factor, $\tan\delta$ increases depending on the frequency points as expected. It can be concluded that the lube oil samples have frequency dependent permittivity characteristics as shown in Table 5.3.

Every lube oil sample has unique content with respect to the mixing particles in different ratios and thus, it has unique dielectric constant and loss factor values as seen in Table 5.3. In addition, it is well known that the dielectric characteristic of the lube oil is not linear in the frequency domain. Hence, it cannot be expected a linear relationship between dielectric constant values of a certain sample at randomly chosen frequency points tabulated in Table 5.3.

The study focuses on the dielectric characteristics that change due to the lube oil qualities and ANN method is applied to monitor how these changes are affected from the amount of mixed mechanical particles to the engine lube oil. They have unique dielectric constant and loss values as seen in the table.

The measurements for each sample are realized by 5 times under the same circumstances (i.e., temperature range, calibration lifetime, etc.) and with the lab instruments by taking into consideration the related Agilent Technologies device standards. Therefore, each testing results obtained under the same conditions are reliable. The error bar figure related to the random measurement errors is plotted in Figure 5.2 at the frequency of 7.40 GHz. The error bars have been calculated by the standard deviation of the 5 random measurements. The dielectric constant or dielectric loss measurement result for each lubricant sample is determined by the average of the 5 random measurements. The standard deviation has been represented as the error bar for these measurement data. The reason why this frequency point is chosen is that the strong correlation between the measurement and ANN result. It means, the consistency between the estimated values by ANN and measured values by coaxial probe can provide the detection of the best operating frequency point to design sensing device. This graph is based on the standard deviation of the testing dataset which consists of 9 random samples with 7 contaminants which can be seen in Table 5.2. The other 24 samples rest from 33 samples are used as training datasets to obtain highly accurate results. It can be concluded that the measurements are repeatable within the accuracy rate of 10%.

Table 5.3. Dielectric constant, dielectric loss factor and dissipation factor measurement results for different locomotive engine lubricant samples

Loco No	**2.40 GHz**			**5.80 GHz**			**7.40 GHz**			**9.60 GHz**		
	ε_r'	ε_r''	$\tan\delta$	ε_r'	ε_r''	$\tan\delta$	ε_r'	ε_r''	$\tan\delta$	ε_r'	ε_r''	$\tan\delta$
A018	2.468	0.193	0.078	2.506	0.177	0.071	2.490	0.312	0.125	2.519	0.475	0.189
A020	2.793	0.019	0.007	2.837	0.223	0.079	2.794	0.373	0.133	2.807	0.617	0.220
A024	2.634	0.065	0.025	2.981	0.228	0.076	2.934	0.400	0.136	2.448	0.435	0.178
A025	2.781	0.022	0.008	3.024	0.280	0.093	2.966	0.431	0.145	2.722	0.518	0.190
A044	2.738	0.054	0.020	3.074	0.298	0.097	3.011	0.448	0.149	2.884	0.598	0.207
A046	2.807	0.044	0.016	3.023	0.280	0.093	2.966	0.438	0.148	2.965	0.679	0.229
A061	2.600	0.075	0.029	2.869	0.203	0.071	2.838	0.366	0.129	2.379	0.407	0.171
A064	2.767	0.030	0.011	3.071	0.298	0.097	3.009	0.452	0.150	2.919	0.659	0.226
A068	2.824	0.031	0.011	2.911	0.248	0.085	2.863	0.398	0.139	2.889	0.645	0.223
A070	2.608	0.075	0.029	2.747	0.170	0.062	2.721	0.318	0.117	2.390	0.413	0.173
A072	2.469	0.127	0.052	2.499	0.161	0.064	2.477	0.286	0.115	2.514	0.469	0.187
B116	2.565	0.113	0.044	2.460	0.083	0.034	2.459	0.229	0.093	2.671	0.421	0.157
B133	2.706	0.021	0.008	3.090	0.300	0.097	3.026	0.458	0.151	2.851	0.649	0.228
B155	2.514	0.128	0.051	2.514	0.127	0.051	2.504	0.263	0.105	2.477	0.458	0.185
B180	2.910	0.039	0.013	2.871	0.220	0.077	2.832	0.375	0.133	3.077	0.719	0.234
B188	2.769	0.072	0.026	2.912	0.254	0.087	2.863	0.406	0.142	2.880	0.648	0.225
B202	2.650	0.112	0.042	2.636	0.156	0.059	2.616	0.298	0.114	2.615	0.502	0.192
B236	2.640	0.090	0.034	2.666	0.148	0.055	2.649	0.300	0.113	2.498	0.470	0.188
B268	2.418	0.167	0.069	2.324	0.128	0.055	2.307	0.249	0.108	2.360	0.404	0.171
B279	2.567	0.098	0.038	2.495	0.139	0.056	2.482	0.269	0.108	2.464	0.449	0.182
B281	2.570	0.111	0.043	2.541	0.143	0.056	2.524	0.275	0.109	2.514	0.465	0.185
B310	2.541	0.119	0.047	2.586	0.140	0.054	2.569	0.281	0.109	2.512	0.472	0.188
B337	2.674	0.046	0.017	3.027	0.251	0.083	2.970	0.418	0.141	2.378	0.410	0.172
B348	2.686	0.034	0.013	2.589	0.163	0.063	2.573	0.295	0.114	2.613	0.521	0.199
B358	2.347	0.188	0.080	2.613	0.230	0.088	2.582	0.361	0.140	2.865	0.645	0.225
B369	2.376	0.192	0.081	2.274	0.105	0.046	2.267	0.229	0.101	2.475	0.458	0.185
B381	2.889	0.033	0.012	2.663	0.178	0.067	2.634	0.318	0.121	2.612	0.419	0.160
B386	2.462	0.178	0.072	2.375	0.134	0.056	2.368	0.255	0.108	2.542	0.481	0.189
B395	2.596	0.080	0.031	2.464	0.090	0.036	2.466	0.230	0.093	2.380	0.406	0.171
C026	2.659	0.035	0.013	2.484	0.113	0.045	2.473	0.256	0.104	2.571	0.413	0.167
C059	2.347	0.187	0.080	2.424	0.179	0.074	2.397	0.295	0.123	2.835	0.638	0.225
C034	2.612	0.082	0.031	2.637	0.147	0.056	2.616	0.302	0.116	2.461	0.457	0.186
C015	2.563	0.083	0.032	2.796	0.182	0.065	2.766	0.340	0.123	2.467	0.454	0.184

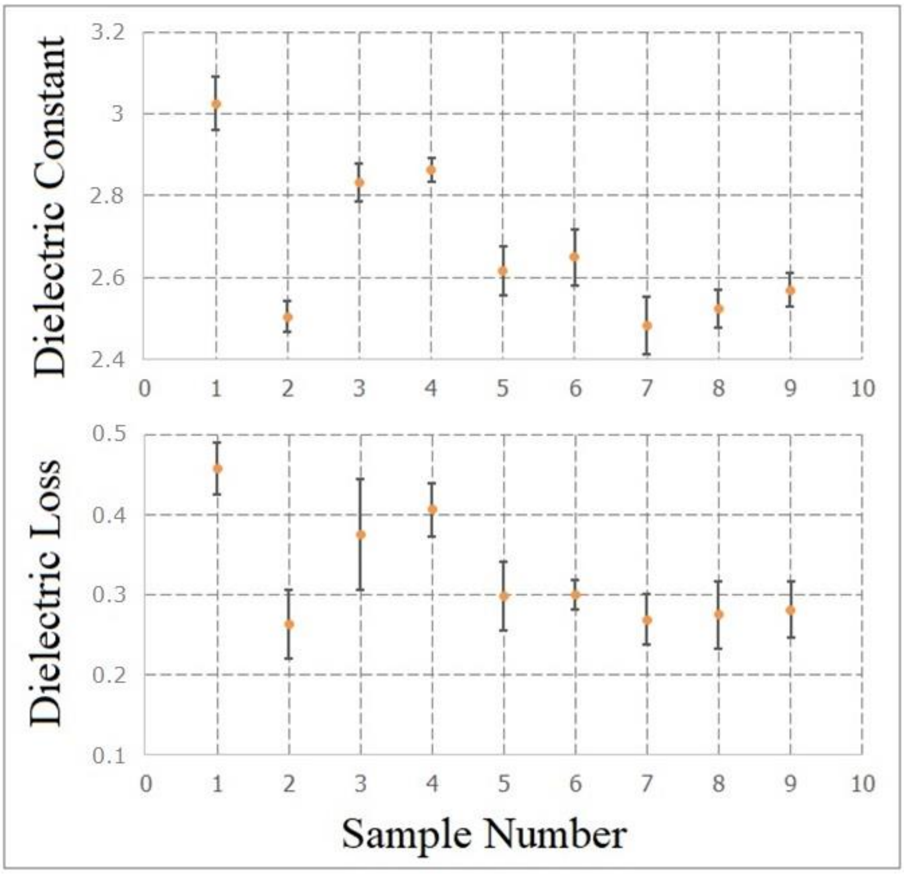

Figure 5.2 The error bar graphs of the testing data sets measured at the 7.40 GHz

5.3. ANN Application for Locomotive Maintenance

This study aims to detect correlation between dielectric characteristics of the different engine lube oils. Particles inside the lube oil samples which are observed through spectral analyzer given in the Table 5.2 are determined as input variables. The output variables are dielectric constant and loss measured by the dielectric probe kit. Therefore, training and testing data set groups having 7 containments in Table 5.2 are composed for regression analysis. An ANN model is evaluated in order to MSE, MAE, MAPE and regression coefficient R. The R shows the linear relationships between observed and estimated dielectric variations of the engine lube oils as illustrated in Figure 5.3. Dielectric constant and loss factor of the engine lubricant samples are measured at for different frequency points because the dielectric loss values increase while the measured frequency band is increasing. Hence, more than one dielectric constant and loss factor measurements are carried out for precision of the study. Moreover, it should be noted that training and testing data sets are not the same for each prediction phase because the observed dielectric constant and loss factor values are frequency dependent. Bayesian regularization backpropagation training algorithm is used for the optimization. This technique updates the weights due to Levenberg-Marquardt optimization. It determines the correct combination to obtain well-generalizing network by minimizing errors and weights. For each frequency point, 24 samples for training data set and 9 samples for test data set are used. Training of the ANN is driven until 1000 epochs. The statistics of the ANN model during the testing period is presented by Table 5.4 with different frequency points.

Table 5.4. Comparison of different frequency points with MSE, MAE, MAPE and R for testing period

	Dielectric Constant				**Dielectric Loss Factor**		
Frequency	**MSE**	**MAE**	**MAPE**	**R**	**MSE**	**MAE**	**R**
2.40 GHz	0.0052	0.0490	1.6323	0.7239	0.0009	0.0246	0.7627
5.80 GHz	0.0140	0.0629	2.1637	0.7951	0.0018	0.0347	0.7196
7.40 GHz	0.0114	0.0932	3.1016	0.8513	0.0023	0.0391	0.8015
9.60 GHz	0.0348	0.1785	6.5011	0.7463	0.0091	0.0917	0.7334

Observed and simulated dielectric constant and loss factor values are produced by an ANN model as illustrated in Figure 5.3 at the frequencies of (a) 2.40 GHz, (b) 5.80 GHz, (c) 7.40 GHz, (d) 9.60 GHz. The highest R values (0.8513 and 0.8015) are obtained at 7.40 GHz for both dielectric constant and loss factor, respectively. Although the value is almost at the same level for other three points, the linear relationship between observed and predicted values is in the sufficient level for all frequency points. The dielectric constant values are observed and predicted between 2.4 and 3 for each phase. However, the dielectric loss factor gradually increases due to frequency point changes. The correlation results for both outputs are in a good agreement.

As seen in the Table 5.4, the smallest MSE (0.0052 and 0.0009), MAE (0.0490 and 0.0246) and MAPE (1.6323) values for dielectric constant and loss factor occurred respectively at 2.40 GHz. The correlations at this frequency point are obtained as 0.7239 and 0.7627. Every prediction phases should be independently evaluated because the data set variations are different for each simulation due to frequency changes. It can be concluded that the MSE, MAE, MAPE and R values for each frequency point we estimated are acceptable.

It can be said that the all samples used in this study have different dielectric characteristics considering the four frequency points. The dielectric constant and dielectric loss factor results are correlated with the variation of the 7 containments in Table 5.2 by using ANN method. This approach strongly exhibits the relation between the dielectric characteristics and various contaminants of the engine lube oil. Many scientists have developed and realized sensor structures by improving waveguide or transmission line based sensor structures having a sensing layer to measure dielectric characteristics of the samples [Withayachumnankul et al. 2013; Akgol et al., 2017; Tamer et al., 2018]. In this respect, new sensor devices which can detect the amount of the contaminants inside of the lubricant can be achieved in future studies. Although, there are many sensor studies have been carried out to detect solid and liquid samples, there is no sensing device to detect lube oils with seven contaminants inside. The determination of each contaminant can provide to detect the specified engine failures defined in Table 5.1. The promised sensing device can also be integrated into the engine systems of the locomotives to obtain real time and low cost measurement as the future study.

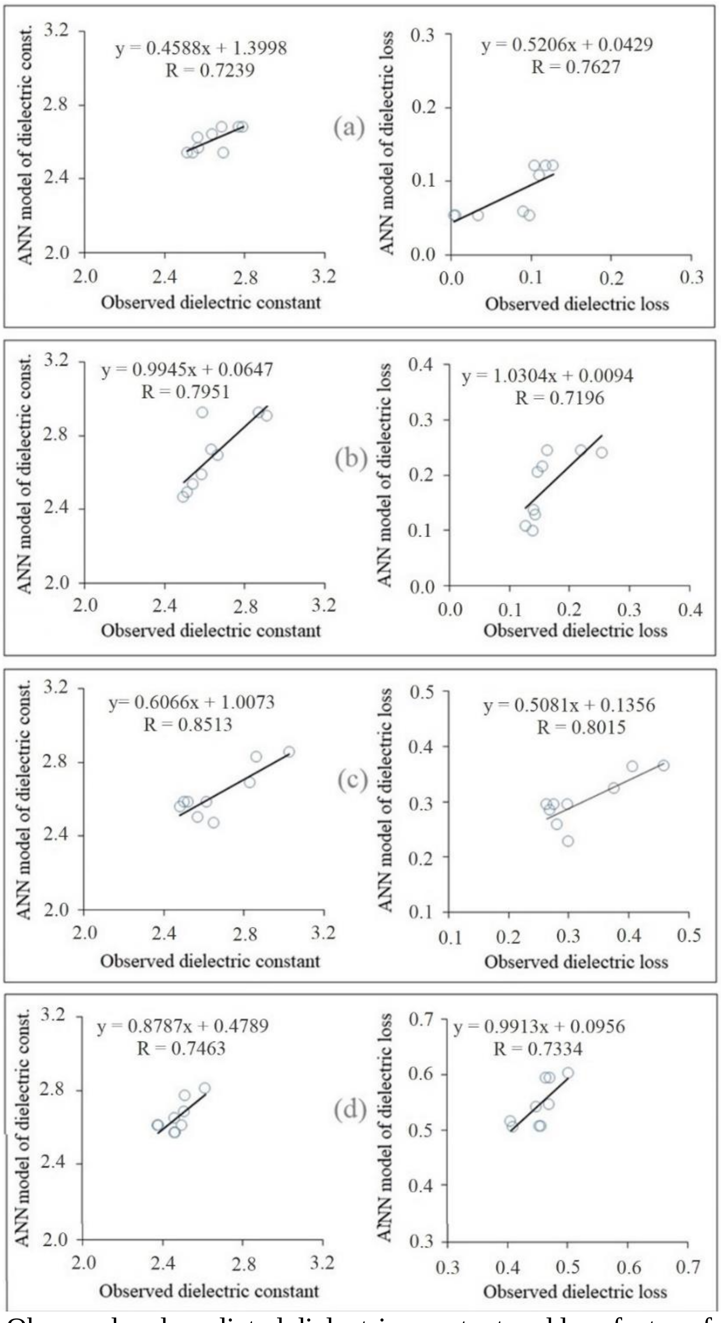

Figure 5.3. Observed and predicted dielectric constant and loss factor of engine lube oils at the frequencies of (a) 2.40 GHz, (b) 5.80 GHz, (c) 7.40 GHz and (d) 9.60 GHz.

This section of the thesis study has been published in Measurement. (doi.org/10.1016/j.measurement.2019.05.087)

6. DISCUSSIONS AND CONCLUSIONS

In chapter 3.1, a MTM based CSRR type multifunctional sensor structure is proposed by analyzing fluid, strain and rotation sensing ability in microwave regime both numerically and experimentally. The study is based on resonance frequency changes in CSRR magnetically coupled with a microstrip transmission line. The fluid, strain and rotation sensing applications are realized by using the samples having different dielectric feature and configuration in the sensing layer. These variations of the samples in the sensing layer create different capacitive effects which directly manipulate and shift the resonance frequency of CSRR. The sensor applications are achieved by monitoring resonance frequency changes both linearly and precisely.

The sensitivity performance of a sensor is highly important especially for critical applications. Beside this, multi-functionality of a sensor also increases interest for the sensor. The multifunctional sensors are especially important for limited space applications of devices. In addition, it provides opportunity to use unique sensing elements instead of three different ones. The sensing properties of a multifunctional sensor can be used one by one or together in an application. The proposed sensor can be adapted to both measures the contamination and the flow rate of the liquids by using the characteristics of liquid type and rotation measurement.

It is well known that displacements actually combine strain and a rigid-body rotation. Hence, exact displacement determination can be measured by this proposed combined sensor with the properties of measuring both strain and rotation characteristic [Arthur et al., 2011]. These properties can be used to determine instantaneous stress in the earth's crust. Another dual application area of the multifunctional sensor is sensing of both vorticity and fluid type. It is well known that the concept of circulation is closely related to the vorticity. The measurement of circulation provides the possibility to determine vorticity of fluid. Besides, with the fluid type sensing properties, the sensor gives a chance to measure both vorticity and fluid type [Rutherford, 1962].

The proposed sensor applications are highly reliable. The fluid sensor is contactless with the liquid under test. Hence, the number of measurement does not affect quality, reliability and mechanism of the sensor structure. In strain measurement process, the sample is positioned in the center of the sensing layer of CSRR without any contact. In this respect, the continuously placed samples cannot deform the sensing structure in strain measurement and the number of measurement does not change the measured data. The rotation sensing mechanism operates by rotating the sample under test in the circle of CSRR gap. In this rotation, the sample does not change both the structure and measurement characteristics of the resonator layer of the sensor. The contact with sensor and sample does not change the measurement data. Beside this, the measured values are repeated many times before final decision of reliability and reproducibility of the sensor.

In chapter 3.2, a MTM based labyrinth resonator type sensor structure is realized by using a microstrip transmission line. The results are obtained both numerically and experimentally with a good agreement. In the chemical liquid sensor section, electrical properties of the samples are measured and the numerical calculations have been realized in the simulation software. The experimental analysis of the chemical liquids has been planned to perform for much lower ratio changes in future studies. In the transformer oil quality sensing study, the electrical properties of the oil samples have been measured first. The sensing study has then been conducted both numerically and experimentally in order to compare and verify the results. The transmission resonance frequencies for the ethanol water and methanol water mixtures are linearly observed due to alcohol ratios in the mixture. Besides, the sensor structure distinguishes PEG 400 and Isopropyl Alcohol which show similar dielectric characteristic from each other in the chemical liquid sensing studies. The proposed sensor also exhibits a good performance in transformer oil quality detection study. There is a 40 MHz frequency difference between the waste and clean oil results. The measured and numerical results for transformer oil quality sensing study are in a good agreement with each other although there is a slight differences stem from the lab conditions, manufacturing process and calibration errors. It can be seen from the results that the sensor structure can be precisely detect fluidics and transformer oil quality even at their small dielectric variations. This structure can be used in many industrial application areas such as chemistry, medicine or energy.

In chapter 3.3, a split ring type resonator structure by integrating a transmission line has been used for microfluidic sensing applications. The ethanol-water mixtures have been used as samples and the numerical and experimental results for sensing applications are in a very good agreement. The operating frequency bands for the proposed five sensor structures have linearly changed with respect to the dimension coefficient. Hence, it is concluded that the split ring resonator based transmission line integrated structure can be reconfigured to the desired operating frequency ranges. The proposed structure can be used for the various samples which have different electrical characteristics at any frequency ranges.

In chapter 3.4, a double split ring resonator based sensor structure is proposed to monitor the wastewater quality at microwave frequency regime. The electrical properties of the samples obtained from three phases as output, back return and ventilation process in wastewater treatment facilities have been measured. It is seen that the sample taken from the output process had almost the same electrical value as the water. The transmission coefficient observed from the transmission line is about -10 dB for all samples. The resonance frequencies for the output, back return and ventilation process have been observed at about 1.758 GHz, 1.769 GHz and 1.853 GHz, respectively. This results show the linear relation between the resonance frequency and dielectric value. Hence the proposed structure can be efficiently used in wastewater treatment facility to decrease the cost of the measurement and to increase safety.

In chapter 4.1, a split meander line based permittivity and thickness sensor is proposed for microwave frequency regime both numerically and experimentally. The sensor structure is examined by observing resonance frequencies of the equivalent circuits. In this point, it is benefitted from the capacitive effects which are occurred in sensing layer of the proposed structure. In this way, the permittivity and thickness characteristics of the flat surfaced materials having different thickness and dielectric value are determined by using numerical and experimental methods. The measured and simulated results are in a good agreement but a certain frequency shift originated from calibration and fabrication errors occurred between these results for all tested samples. The proposed sensor structure can be used in many areas such as microwave engineering, material engineering and military purposes to test and improve micro and nano scale structures.

In chapter 4.2, in this study, a MTM inspired sensor structure has been presented for different industrial applications both numerically and experimentally. The electrical characteristics of the samples are firstly investigated at X-band frequency regime by using a coaxial type dielectric probe kit. The numerical studies are then realized for gasoline, diesel, lubricant and transformer oil samples. After that the proposed structure is manufactured and experimental analyses are carried out by PNA-L Agilent vector network analyzer and proper waveguide setup. Finally, numerical and experimental results are compared.

The proposed sensor structure is able to clearly distinguish the inauthentic and authentic gasoline samples from each other since their dielectric values are highly different. The other inauthentic fuel detection study has been achieved by the diesel samples. The sensor structure has successfully distinguished the inauthentic diesel sample from authentic diesel sample. The last two studies are about lubricant and transformer oil quality detection. Dielectric properties of the clean and waste lubricant samples is appear to be very similar. However, the sensor structure precisely exhibits the difference between the clean and waste samples with the frequency shift of 61 MHz in experimental. Accordingly, the dielectric values of the clean and waste transformer oil is very close to each other. The dielectric constant difference between these samples is about 0.15. The proposed sensor structure distinguishes sensitively the waste transformer oil sample from the clean sample with the 65 MHz in experimental. In conclusion, the sensor structure can be efficiently used in the industrial implementations at the X-band frequency regime. Moreover, the structure is low cost, durable and reconfigurable at any desired frequency range.

The operating frequency range of the study has been carefully chosen since the most important issue is to monitor sufficient differentiation between the samples. The X band frequency regime gives the precise results to observe the difference sensitively with the sensor structure. Moreover, this higher frequency regime provides to get compact size sensor structure. Although the sensor including waveguide and adapters is expensive as price, the sensing implementation results for the four different study is very sufficient, sensitive and precise. Some of these applications are about the adulteration to prevent the smuggling and to save a huge amount of money. Some of them are about the improvement machine/transformer safety of systems and decreasing the costs by detecting failures instantly. Hence, the cost of the measurement setup with waveguide and the price of the sensor structure can be negligible.

In the experimental process, transmission coefficients for every liquid sample have been measured by 10 times with the proposed sensor structure. The observed results remain constant. Hence it can be said that the sensor structure has high durability with substrate material having high flexural strength, thermal strength, and thermal stress. Moreover, proposed sensor sensitively distinguishes the samples from each other considering the other studies in the literature. In [Tumkaya et al., 2017], the sensor structure provided about 100 MHz frequency shift between the authentic and inauthentic diesel samples. In the same study, about 50 MHz frequency shift occurred between authentic and inauthentic gasoline samples. In [Tamer et al., 2018], the transmission line based sensor structure experimentally discriminated authentic and inauthentic diesel samples with 50 MHz of frequency shift considering the transmission coefficient. In [Rawat et al., 2016], the researcher proposed a high sensitive sensor structure which can detect the fuel adulteration by 27 MHz of frequency shift in resonance frequency. A similar study with kerosene had been realized in [Bakır et al., 2018] with 32 MHz of resonance frequency shift.

The difference between two liquid samples for four applications is directly proportional with the dielectric constant value. The dielectric constant and resonance frequency differences are about 0.65 and 361 MHz, 0.27 and 173 MHz, 0.12 and 61 MHz, 0.13 and 65 MHz for gasoline, diesel, lubricant and transformer oil samples, respectively. It can be seen from these values that some differences exist in sensitivity. However, these sensitivity differences are originated from the irregularity of the dielectric loss values of the samples. Although the dielectric constant values differences are the same for lubricant and transformer oil samples, the dielectric loss values differences are about 0.05 and zero for these samples, respectively. Hence the sensitivity difference is observed as about 4 MHz. The same sensitivity issue can be observed between results for gasoline and diesel samples. The direct relations can be observed between the dielectric constant difference and frequency shifts. However, the dielectric loss values of them play key role by determining the sensitivity. Although the simulations and experiments share similar resonance frequencies, their waveforms are different from each other. It can be seen that the quality factor (Q-factor) of the experimental results is higher than the simulated ones. The difference is originated from the waveguide calibration errors, probe loss and probe connection mismatches. This causes lower transmission ratio at resonance frequencies in experimental process.

The reason why the omega-shaped resonator is chosen is that it can response both electric and magnetic component of the incident electromagnetic wave [Aydin et al., 2008]. Since the split ring resonator based sensor structures only response to the magnetic component of the electromagnetic waves and sense the changes occurring in the magnetic field, they cannot be sufficient in some applications. On the other hand, the omega shaped resonator based sensor structure has the capability for more sensitive observations due to response both component of electromagnetic wave although it is polarization dependent like split ring resonator. In addition, the proposed sensor structure have compact size considering the operating frequency range, which can be considered as an advantageous for the implementations. Another advantageous side of the study is that the sensor promises a multi-functional sensing application which can distinguish the four different samples groups.

In chapter 4.3, MTM inspired sensor structure has been realized in numerical for engine lube oil quality detection at X band. The permittivity difference is observed between the clean and waste lube oil samples. This electrical difference create difference capacitive effect in the sensing layer of the sensor structure. Therefore, 100 MHz of resonance frequency shifts are obtained between these two samples. It is concluded that the sensor structure can be applied to industrial applications such as engine lubricant.

In chapter 5, an approach for locomotive maintenance techniques by examining engine lube oils has been proposed. Our aim is to obtain correlation between dielectric values of the locomotive engine lubricant and mechanical particle changes in the same lubricant. The dielectric constant and loss factor values of lubricant samples are measured by using a dielectric probe kit at four frequency points after the mechanical particles mixing with the lube oil are observed through a spectral analyzer. An ANN model is applied to predict dielectric variations of different locomotive engine lube oil samples. Various training and testing group's data sets are applied at four frequency points. The MSE, MAE, MAPE and R results are very convincing for all frequency points.

The correlation coefficients especially for the values at 7.40 GHz are enough to show relation between the electrical features and wear metal features of lube oil samples. Thanks to the proposed relationship, a microwave-based sensor device will be designed at this frequency band as a future study. This sensor device will be designed by using non-destructive techniques which is suitable for fast observation in order to easily observe and prevent the locomotive systems failures. In this respect, the exhibited relationship gives a chance to design a sensor which can provide a rough idea about the ingredient of the lube oil. Although the chemical analysis and microscopic observation techniques give more precise results, these techniques are not suitable for real-time analysis and have the possibilities to halt the locomotive systems. However, the proposed approach can easily observe engine failures instantly in order to prevent emergency situations.

The approach proposes a different measurement method since the idea is based on permittivity detection of engine lube oil for locomotive maintenance technique. Besides, the results are sufficiently reliable, since each sample is tested 5 times in order to finalize the values. Basically, if the R is approaching to 0.8 and the MAPE is smaller than 10%, the results are satisfying. Therefore, the MAPE and R results for dielectric constant at four different frequency points are reasonable results. The proposed approach can be used as an alternative technique rather than using non-real time and more expensive spectral analyzer method. The flowchart for the proposed model can be described as Figure 6.1. In addition, the study can be an important basis for the sensor devices which detects engine quality from lubricant samples for the future works.

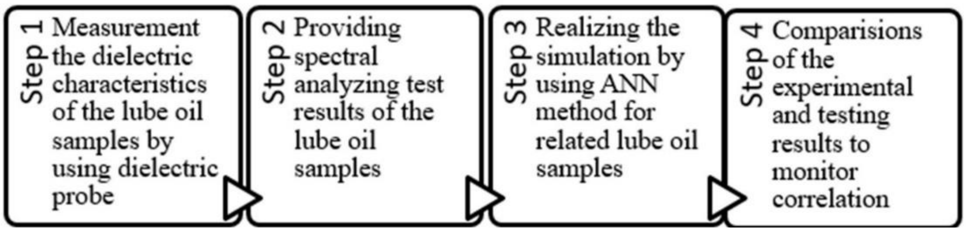

Figure 6.1. The flowchart for the proposed model

The relationship between relative dielectric constant and various particles in lubricant oil has been extracted by using ANN method at the related frequency point. Beside this, the accuracy of the ANN method has been demonstrated for some measurement results of the relative dielectric constant. It is expected that the created

ANN algorithm can be used to determine the relative dielectric constants of the lubricant oil with various particles of materials. This determination can provide to decide the failures of the engine that can come into existence. Hence, the created ANN approach can be used in a sensor system to detect the failures in future applications.

REFERENCES

Abduljabar, A. A., Rowe, D. J., Porch, A. and Barrow, D. A., (2014). "Novel microwave microfluidic sensor using a microstrip split-ring resonator." IEEE Transactions on Microwave Theory and Techniques 62(3): 679-688.

Abdulkarım, Y. I., Deng, L., Altıntaş, O., Ünal, E. and Karaaslan, M., (2019). "Metamaterial absorber sensor design by incorporating swastika shaped resonator to determination of the liquid chemicals depending on electrical characteristics." Physica E: Low-dimensional Systems and Nanostructures 114: 113593.

Akgol, O., Altıntas, O., Dalkılınc, E. E., Unal, E., Karaaslan, M. and Sabah, C., (2017). "Metamaterial absorber-based multisensor applications using a meander-line resonator." Optical Engineering 56(8): 087104.

Albishi, A. M. and Ramahi, O. M., (2017). "Microwaves-based high sensitivity sensors for crack detection in metallic materials." IEEE Transactions on Microwave Theory and Techniques 65(5): 1864-1872.

Alkurt, F. O., Altıntas, O., Ozakturk, M., Karaaslan, M., Akgol, O., Unal, E. and Sabah, C., (2020). "Enhancement of image quality by using metamaterial inspired energy harvester." Physics Letters A 384(1): 126041.

Altıntas, O., Unal, E., Akgol, O., Karaaslan, M., Karadag, F. and Sabah, C., (2017). "Design of a wide band metasurface as a linear to circular polarization converter." Modern Physics Letters B 31(30): 1750274.

Altıntaş, O., Aksoy, M. and Ünal, E., (2020). "Design of a metamaterial inspired omega shaped resonator based sensor for industrial implementations." Physica E: Low-dimensional Systems and Nanostructures 116: 113734.

Aris, R. (1962). Vectors, Tensors and the Equations of Fluid Mechanics, Prentice Hall, Englewood Cliffs, NJ.

Aristov, A. I., Manousidaki, M., Danilov, A., Terzaki, K., Fotakis, C., Farsari, M. and Kabashin, A. V., (2016). "3D plasmonic crystal metamaterials for ultra-sensitive biosensing." Scientific reports 6: 25380.

Aydın, K., Bulu, I. and Ozbay, E., (2007). "Subwavelength resolution with a negative-index metamaterial superlens." Applied physics letters 90(25): 254102.

Aydın, K., Li, Z., Bilge, S. and Ozbay, E., (2008). "Experimental and numerical study of omega type bianisotropic metamaterials combined with a negative permittivity medium." Photonics and Nanostructures-Fundamentals and Applications 6(1): 116-121.

Bağmancı, M., Karaaslan, M., Altıntaş, O., Karadağ, F., Tetik, E. and Bakır, M., (2018). "Wideband metamaterial absorber based on CRRs with lumped elements for microwave energy harvesting." Journal of Microwave Power and Electromagnetic Energy 52(1): 45-59.

Bakır, M., Karaaslan, M., Akgol, O., Altıntas, O., Unal, E. and Sabah, C., (2018). "Sensory applications of resonator based metamaterial absorber." Optik 168: 741-746.

Bakır, M., Karaaslan, M., Unal, E., Karadag, F., Alkurt, F. Ö., Altıntaş, O., Dalgac, S. and Sabah, C., (2018). "Microfluidic and fuel adulteration sensing by using chiral metamaterial sensor." Journal of The Electrochemical Society 165(11): B475.

Bartz, W. J. (2019). Engine oils and automotive lubrication, Routledge.

Bilotti, F., Toscano, A., Vegni, L., Aydın, K., Alıcı, K. B. and Ozbay, E., (2007). "Equivalent-circuit models for the design of metamaterials based on artificial magnetic inclusions." IEEE Transactions on Microwave Theory and Techniques 55(12): 2865-2873.

Blackham, D. V. and Pollard, R. D., (1997). "An improved technique for permittivity measurements using a coaxial probe." IEEE Transactions on Instrumentation and Measurement 46(5): 1093-1099.

Boresi, A. P., Chong, K. and Lee, J. D. (2010). Elasticity in engineering mechanics, John Wiley & Sons.

Chandwani, V., Agrawal, V. and Nagar, R., (2015). "Modeling slump of ready mix concrete using genetic algorithms assisted training of Artificial Neural Networks." Expert Systems with Applications 42(2): 885-893.

Chen, H., Chan, C. T. and Sheng, P., (2010). "Transformation optics and metamaterials." Nature materials 9(5): 387-396.

Chen, M., Fan, F., Shen, S., Wang, X. and Chang, S., (2016). "Terahertz ultrathin film thickness sensor below λ/90 based on metamaterial." Applied Optics 55(23): 6471-6474.

Chen, M., Singh, L., Xu, N., Singh, R., Zhang, W. and Xie, L., (2017). "Terahertz sensing of highly absorptive water-methanol mixtures with multiple resonances in metamaterials." Optics Express 25(13): 14089-14097.

Chen, Z., Guo, B., Yang, Y. and Cheng, C., (2014). "Metamaterials-based enhanced energy harvesting: A review." Physica B: Condensed Matter 438: 1-8.

Cong, L., Cao, W., Zhang, X., Tian, Z., Gu, J., Singh, R., Han, J. and Zhang, W., (2013). "A perfect metamaterial polarization rotator." Applied Physics Letters 103(17): 171107.

De Myttenaere, A., Golden, B., Le Grand, B. and Rossi, F., (2016). "Mean absolute percentage error for regression models." Neurocomputing 192: 38-48.

Ebrahimi, A., Withayachumnankul, W., Al-Sarawi, S. and Abbott, D., (2013). "High-sensitivity metamaterial-inspired sensor for microfluidic dielectric characterization." IEEE Sensors Journal 14(5): 1345-1351.

Ebrahimi, A., Withayachumnankul, W., Al-Sarawi, S. F. and Abbott, D., (2014). "Metamaterial-inspired rotation sensor with wide dynamic range." IEEE Sensors Journal 14(8): 2609-2614.

Erentok, A. and Ziolkowski, R. W., (2008). "Metamaterial-inspired efficient electrically small antennas." IEEE Transactions on Antennas and Propagation 56(3): 691-707.

Foteinopoulou, S., Economou, E. N. and Soukoulis, C., (2003). "Refraction in media with a negative refractive index." Physical review letters 90(10): 107402.

Gargari, A. M., Ozbey, B., Demir, H. V., Altıntas, A., Albostan, U., Kurc, O. and Ertürk, V. B., (2018). "A wireless metamaterial-inspired passive rotation sensor with submilliradian resolution." IEEE Sensors Journal 18(11): 4482-4490.

Geng, Z., Zhang, X., Fan, Z., Lv, X. and Chen, H., (2017). "A route to terahertz metamaterial biosensor integrated with microfluidics for liver cancer biomarker testing in early stage." Scientific reports 7(1): 1-11.

Gordon, J. A., Holloway, C. L., Booth, J., Kim, S., Wang, Y., Baker-Jarvis, J. and Novotny, D. R., (2011). "Fluid interactions with metafilms/metasurfaces for tuning, sensing, and microwave-assisted chemical processes." Physical Review B 83(20): 205130.

Govind, G. and Akhtar, M. J., (2019). "Metamaterial-inspired microwave microfluidic sensor for glucose monitoring in aqueous solutions." IEEE Sensors Journal 19(24): 11900-11907.

Haykın, S. (1998). Neural Networks: A Comprehensive Foundation. United States, Prentice Hall PTR Upper Saddle River, NJ.

He, X.-J., Wang, Y., Wang, J.-M. and Gui, T.-L., (2010). "Thin-film sensor based tip-shaped split ring resonator metamaterial for microwave application." Microsystem technologies 16(10): 1735-1739.

Hoffman, A. J., Alekseyev, L., Howard, S. S., Franz, K. J., Wasserman, D., Podolskiy, V. A., Narimanov, E. E., Sivco, D. L. and Gmachl, C., (2007). "Negative refraction in semiconductor metamaterials." Nature materials 6(12): 946-950.

Holloway, C. L., Kuester, E. F. and Novotny, D., (2009). "Waveguides composed of metafilms/metasurfaces: The two-dimensional equivalent of metamaterials." IEEE Antennas and Wireless Propagation Letters 8: 525-529.

Hosu, A., Cristea, V.-M. and Cimpoiu, C., (2014). "Analysis of total phenolic, flavonoids, anthocyanins and tannins content in Romanian red wines: Prediction of antioxidant activities and classification of wines using artificial neural networks." Food chemistry 150: 113-118.

Hu, X., Xu, G., Wen, L., Wang, H., Zhao, Y., Zhang, Y., Cummıng, D. R. and Chen, Q., (2016). "Metamaterial absorber integrated microfluidic terahertz sensors." Laser & Photonics Reviews 10(6): 962-969.

Huang, Y. and Wu, L. H., (2016). "Two-step complete calibration of magnetic vector gradiometer based on functional link artificial neural network and least squares." IEEE Sensors Journal 16(11): 4230-4237.

Hyndman, R. J. and Koehler, A. B., (2006). "Another look at measures of forecast accuracy." International journal of forecasting 22(4): 679-688.

Jafari, F. S. and Ahmadi-Shokouh, J., (2018). "Frequency-selective surface to determine permittivity of industrial oil and effect of nanoparticle addition in x-band." Journal of Electronic Materials 47(2): 1397-1404.

JARUWONGRUNGSEE, K., WITHAYACHUMNANKUL, W., WISITSORAAT, A., ABBOTT, D., FUMEAUX, C. and TUANTRANONT, A. (2012). Metamaterial-inspired microfluidic-based sensor for chemical discrimination. SENSORS, 2012 IEEE, IEEE.

Kabashin, A., Evans, P., Pastkovsky, S., Hendren, W., Wurtz, G., Atkinson, R., Pollard, R., Podolskiy, V. and Zayats, A., (2009). "Plasmonic nanorod metamaterials for biosensing." Nature materials 8(11): 867-871.

Karaaslan, M., Bağmancı, M., Ünal, E., Akgol, O., Altıntaş, O. and Sabah, C., (2018). "Broad band metamaterial absorber based on wheel resonators with lumped elements for microwave energy harvesting." Optical and Quantum Electronics 50(5): 225.

Keshavarz, A. and Vafapour, Z., (2018). "Water-based terahertz metamaterial for skin cancer detection application." IEEE Sensors Journal 19(4): 1519-1524.

Keshavarz, A. and Zakery, A., (2017). "Ultrahigh sensitive temperature sensor based on graphene-semiconductor metamaterial." Applied Physics A 123(12): 797.

Khorasani, A. and Yazdı, M. R. S., (2017). "Development of a dynamic surface roughness monitoring system based on artificial neural networks (ANN) in milling operation." The International Journal of Advanced Manufacturing Technology 93(1-4): 141-151.

Kısı, O., (2007). "Evapotranspiration modelling from climatic data using a neural computing technique." Hydrological Processes: An International Journal 21(14): 1925-1934.

Landy, N. I., Sajuyigbe, S., Mock, J. J., Smith, D. R. and Padilla, W. J., (2008). "Perfect metamaterial absorber." Physical review letters 100(20): 207402.

Lee, H.-J., Lee, J.-H., Moon, H.-S., Jang, I.-S., Choı, J.-S., Yook, J.-G. and Jung, H.-I., (2012). "A planar split-ring resonator-based microwave biosensor for label-free detection of biomolecules." Sensors and Actuators B: Chemical 169: 26-31.

Lee, K. H., Ahmed, I., Goh, R. S. M., Khoo, E. H., Li, E. P. and Hung, T. G. G., (2011). "Implementation of the FDTD method based on Lorentz-Drude dispersive model on GPU for plasmonics applications." Progress In Electromagnetics Research 116: 441-456.

Lezec, H. J., Dionne, J. A. and Atwater, H. A., (2007). "Negative refraction at visible frequencies." science 316(5823): 430-432.

Li, S., Devlin, M. T., Liesen, G. P., West, C. T. and Jao, T.-C., (2000). "Low Temperature Rheology of Engine Lubricants: Investigation of High Used Oil Pumping Viscosity." SAE transactions: 2895-2905.

Lin, Y.-S., (2017). "Complementary infrared metamaterials for volatile organic solutions sensing." Materials Letters 195: 55-57.

Liu, X., Li, C., Yao, K., Meng, X. and Li, F., (2009). "Invisibility cloaks modeled by anisotropic metamaterials based on inductor-capacitor networks." IEEE Antennas and Wireless Propagation Letters 8: 1154-1157.

Maci, S., (2010). "A cloaking metamaterial based on an inhomogeneous linear field transformation." IEEE Transactions on Antennas and propagation 58(4): 1136-1143.

Melik, R., Unal, E., Kosku Perkgoz, N., Puttlitz, C. and Demir, H. V., (2009). "Flexible metamaterials for wireless strain sensing." Applied Physics Letters 95(18): 181105.

Miyamaru, F., Hattorı, K., Shıraga, K., Kawashıma, S., Suga, S., Nıshıda, T., Takeda, M. and Ogawa, Y., (2014). "Highly sensitive terahertz sensing of glycerol-water mixtures with metamaterials." Journal of Infrared, Millimeter, and Terahertz Waves 35(2): 198-207.

Moosavi, S. S., Djerdir, A., Ait-Amirat, Y., Khaburi, D. A. and N'diaye, A., (2016). "Artificial neural network-based fault diagnosis in the AC–DC converter of the power supply of series hybrid electric vehicle." IET Electrical Systems in Transportation 6(2): 96-106.

Mortier, R. M., Orszulik, S. T. and Fox, M. F. (2010). Chemistry and technology of lubricants, Springer.

Muhammad, N., Fu, T., Liu, Q., Tang, X., Deng, Z.-L. and Ouyang, Z., (2018). "Plasmonic metasurface absorber based on electro-optic substrate for energy harvesting." Materials 11(11): 2315.

Mumby, S. J., (1989). "An overview of laminate materials with enhanced dielectric properties." Journal of Electronic Materials 18(2): 241-250.

Ni, B., Wang, Z., Zhao, R., Ma, X., Xing, Z., Yang, L., Huang, L., Lin, Y. and Zhang, D., (2017). "Realisation of a humidity sensor based on perfect metamaterial absorber." Optical and Quantum Electronics 49(1): 33.

Pendry, J. B., (2000). "Negative refraction makes a perfect lens." Physical review letters 85(18): 3966.

Rahman, M., Islam, M. and Samsuzzaman, M., (2018). "Design and analysis of a resonator based metamaterial for sensor applications." Microwave and Optical Technology Letters 60(3): 694-698.

Rawat, V., Kitture, R., Kumari, D., Rajesh, H., Banerjee, S. and Kale, S., (2016). "Hazardous materials sensing: An electrical metamaterial approach." Journal of Magnetism and Magnetic Materials 415: 77-81.

Rawat, V., Nadkarni, V. and Kale, S., (2016). "Highly sensitive electrical metamaterial sensor for fuel adulteration detection." Defence Science Journal 66(4): 421-424.

Reinhard, B., Schmitt, K. M., Wollrab, V., Neu, J., Beigang, R. and Rahm, M., (2012). "Metamaterial near-field sensor for deep-subwavelength thickness measurements and sensitive refractometry in the terahertz frequency range." Applied Physics Letters 100(22): 221101.

Rizza, C., Di Falco, A., Scalora, M. and Ciattoni, A., (2015). "One-dimensional chirality: strong optical activity in epsilon-near-zero metamaterials." Physical review letters 115(5): 057401.

Sabah, C., Dincer, F., Karaaslan, M., Unal, E., Akgol, O. and Demirel, E., (2014). "Perfect metamaterial absorber with polarization and incident angle independencies based on ring and cross-wire resonators for shielding and a sensor application." Optics Communications 322: 137-142.

Sabah, C., Turkmen-Kucuksarı, O. and Turhan-Sayan, G., (2014). "Metamaterial absorber-based sensor embedded into X-band waveguide." Electronics letters 50(15): 1074-1076.

Sadeqi, A., Nejad, H. R. and Sonkusale, S., (2017). "Low-cost metamaterial-on-paper chemical sensor." Optics express 25(14): 16092-16100.

Saghati, A. P., Batra, J. S., Kameoka, J. and Entesarı, K., (2017). "A metamaterial-inspired wideband microwave interferometry sensor for dielectric spectroscopy of liquid chemicals." IEEE Transactions on Microwave Theory and Techniques 65(7): 2558-2571.

Salim, A. and Lim, S., (2016). "Complementary split-ring resonator-loaded microfluidic ethanol chemical sensor." Sensors 16(11): 1802.

Sethi, K. K., Palai, G. and Sarkar, P., (2018). "Realization of accurate blood glucose sensor using photonics based metamaterial." Optik 168: 296-301.

Shahmarvandi, E. K., Ghaderi, M., Ayerden, P., De Graaf, G. and Wolffenbuttel, R., (2016). "Implementation of CMOS-compatible metamaterial absorber for gas sensing application." Procedia engineering 168: 1241-1244.

Shelby, R. A., Smith, D. R. and Schultz, S., (2001). "Experimental verification of a negative index of refraction." science 292(5514): 77-79.

Shih, K., Pitchappa, P., Manjappa, M., Ho, C. P., Singh, R. and Lee, C., (2017). "Microfluidic metamaterial sensor: Selective trapping and remote sensing of microparticles." Journal of Applied Physics 121(2): 023102.

Soffiatti, A., Max, Y., G Silva, S. and M De Mendonça, L., (2018). "Microwave metamaterial-based sensor for dielectric characterization of liquids." Sensors 18(5): 1513.

Sreekanth, K. V., Alapan, Y., Elkabbash, M., Ilker, E., Hinczewski, M., Gurkan, U. A., De Luca, A. and Strangi, G., (2016). "Extreme sensitivity biosensing platform based on hyperbolic metamaterials." Nature materials 15(6): 621-627.

Tamer, A., Alkurt, F. O., Altıntas, O., Karaaslan, M., Unal, E., Akgol, O., Karadag, F. and SABAH, C., (2018). "Transmission line integrated metamaterial based liquid sensor." Journal of The Electrochemical Society 165(7): B251.

Tip, A., (2004). "Linear dispersive dielectrics as limits of Drude-Lorentz systems." Physical Review E 69(1): 016610.

Torun, H., Cagrı Top, F., Dundar, G. and Yalcınkaya, A., (2014). "An antenna-coupled split-ring resonator for biosensing." Journal of Applied Physics 116(12): 124701.

Tümkaya, M. A., Dinçer, F., Karaaslan, M. and Sabah, C., (2017). "Sensitive metamaterial sensor for distinction of authentic and inauthentic fuel samples." Journal of Electronic Materials 46(8): 4955-4962.

Tümkaya, M. A., Karaaslan, M. and Sabah, C., (2018). "Metamaterial-based fluid sensor for identifying different types of fuel oil samples." Chinese journal of physics 56(5): 1872-1878.

Vafaei, M., Afrand, M., Sina, N., Kalbasi, R., Sourani, F. and Teimouri, H., (2017). "Evaluation of thermal conductivity of MgO-MWCNTs/EG hybrid nanofluids based on experimental data by selecting optimal artificial neural networks." Physica E: Low-dimensional Systems and Nanostructures 85: 90-96.

Vélez, P., Su, L., Grenier, K., Mata-Contreras, J., Dubuc, D. and Martín, F., (2017). "Microwave microfluidic sensor based on a microstrip splitter/combiner configuration and split ring resonators (SRRs) for dielectric characterization of liquids." IEEE Sensors Journal 17(20): 6589-6598.

Veselago, V., (1968). "Electrodynamics of substances with simultaneously negative electrical and magnetic permeabilities." Soviet Physics Uspekhi 10(4): 504-509.

Wang, H., Sivan, V. P., Mitchell, A., Rosengarten, G., Phelan, P. and Wang, L., (2015). "Highly efficient selective metamaterial absorber for high-temperature solar thermal energy harvesting." Solar Energy Materials and Solar Cells 137: 235-242.

Wang, R., Li, L., Tian, H., Liu, J., Liu, J., Tian, F., Zhang, J. and Sun, W., (2018). "Full telecomband covered half-wave meta-reflectarray for efficient circular polarization conversion." Optics Communications 427: 469-476.

Wang, S., Niu, M. and XU, D., (1998). "A frequency-varying method for simultaneous measurement of complex permittivity and permeability with an open-ended coaxial probe." IEEE transactions on microwave theory and techniques 46(12): 2145-2147.

Wang, X., Chen, F. and Semouchkina, E., (2013). "Implementation of low scattering microwave cloaking by all-dielectric metamaterials." IEEE microwave and wireless components letters 23(2): 63-65.

Withayachumnankul, W., Jaruwongrungsee, K., Tuantranont, A., Fumeaux, C. and Abbott, D., (2013). "Metamaterial-based microfluidic sensor for dielectric characterization." Sensors and Actuators A: Physical 189: 233-237.

Wu, J., Wang, P., Huang, X., Rao, F., Chen, X., Shen, Z. and Yang, H., (2018). "Design and validation of liquid permittivity sensor based on RCRR microstrip metamaterial." Sensors and Actuators A: Physical 280: 222-227.

Yoo, M., Kim, H. K. and Lim, S., (2016). "Electromagnetic-based ethanol chemical sensor using metamaterial absorber." Sensors and Actuators B: Chemical 222: 173-180.

Zeng, Y., Zhang, H., Zhang, H. and Hu, Z., (2010). "Effective permittivity calculation of composites with interpenetrating phases." Journal of electronic materials 39(8): 1351-1357.

Zhao, X., Ren, L., Liao, R., Li, J., Yang, L. and Wang, F., (2016). "Role of Relaxation on the Giant Permittivity and Electrical Properties of CaCu 3 Ti 4 O 12 Ceramics." Journal of Electronic Materials 45(6): 3079-3086.

Zhou, H., Hu, D., Yang, C., Chen, C., Ji, J., Chen, M., Chen, Y., Yang, Y. and mu, X., (2018). "Multi-band sensing for dielectric property of chemicals using metamaterial integrated microfluidic sensor." Scientific reports 8(1): 1-11.

Zhu, H., Cheung, S., Chung, K. L. and Yuk, T. I., (2013). "Linear-to-circular polarization conversion using metasurface." IEEE Transactions on Antennas and Propagation 61(9): 4615-4623.

BIOGRAPHY

Olcay Altıntaş was born in Kaman, Kırşehir, Turkey in 1988. He received the B.Sc. degree in electrical and electronics engineering from Cukurova University, Adana Turkey in 2011 and received his M.Sc. degree by studying in the field of the polarization converter metasurfaces from Mustafa Kemal University, Hatay, Turkey in 2015. From 2012 to 2015, he was a Research Assistant at the Department of Electrical and Electronics Engineering, Mustafa Kemal University. Since 2015, he has been a Research Assistant at the Department of Electrical and Electronics Engineering, Iskenderun Technical University, Hatay, Turkey. His main research interests includes metamaterial based sensors, absorbers, energy harvesters and polarization converters in microwave regime.

SCI/SCI-Expanded Publications and Conference Proceedings

Altıntaş, O., Aksoy, M., & Ünal, E. (2020). Design of a metamaterial inspired omega shaped resonator based sensor for industrial implementations. Physica E: Low-dimensional Systems and Nanostructures, 116, 113734.

Altintas, O., Aksoy, M., Unal, E., Akgol, O., & Karaaslan, M. (2019). Artificial Neural Network Approach for Locomotive Maintenance by Monitoring Dielectric Properties of Engine Lubricant. Measurement, 145, 678-686.

Altintaş, O., Aksoy, M., Ünal, E., & Karaaslan, M. (2019). Chemical Liquid and Transformer Oil Condition Sensor Based on Metamaterial-Inspired Labyrinth Resonator. Journal of The Electrochemical Society, 166(6), B482-B488.

Altintas, O., Aksoy, M., Unal, E., Karakasli, F., & Karaaslan, M. (2018). A split meander line resonator-based permittivity and thickness sensor design for dielectric materials with flat surface. Journal of Electronic Materials, 47(10), 6185-6192.

Altintas, O., Aksoy, M., Akgol, O., Unal, E., Karaaslan, M., & Sabah, C. (2017). Fluid, Strain and Rotation Sensing Applications by Using Metamaterial Based Sensor. Journal of The Electrochemical Society, 164(12), B567-B573.

Altıntaş, O., Aksoy, M., Ünal, E., & Karaaslan, M. (2019, November). Double split ring resonator based microfluidic sensor for wastewater treatment applications. In AIP Conference Proceedings (Vol. 2178, No. 1, p. 030011). AIP Publishing LLC.

Altıntaş, O., Aksoy, M., Ünal, E., & Karaaslan, M. (2019, November). Metamaterial inspired sensor for detection of engine lubricant oil condition. In AIP Conference Proceedings (Vol. 2178, No. 1, p. 030010). AIP Publishing LLC.

APPENDIX

Journal of The Electrochemical Society, 164 (12) B567-B573 (2017)
0013-4651/2017/164(12)/B567/7/$37.00 © The Electrochemical Society

Fluid, Strain and Rotation Sensing Applications by Using Metamaterial Based Sensor

Olcay Altintas,[a,b] Murat Aksoy,[b] Oguzhan Akgol,[a] Emin Unal,[a] Muharrem Karaaslan,[a] and Cumali Sabah[c,d,z]

[a]Department of Electrical and Electronics Engineering, Iskenderun Technical University, Iskenderun, Hatay 31200, Turkey
[b]Department of Electrical and Electronics Engineering, Cukurova University, Saricam, Adana 01330, Turkey
[c]Department of Electrical and Electronics Engineering, Middle East Technical University - Northern Cyprus Campus (METU-NCC), Kalkanli, Guzelyurt, TRNC / Mersin 10, Turkey
[d]Kalkanli Technology Valley (KALTEV), Middle East Technical University - Northern Cyprus Campus (METU-NCC), Kalkanli, Guzelyurt, TRNC / Mersin 10, Turkey

We propose a design of a metamaterial based sensor to be used in various applications including micro-fluid, strain and rotation sensing. The structure has a simple geometry composed of a single circular split ring resonator (CSRR) and it is possible to adjust the resonance frequency in the region of desired band. The resonance frequency is carefully selected so that the materials to be sensed have linear dielectric curves at that particular frequency range which iscrucial to design accurate sensing characteristic. Three importantapplications are investigated, namely density, rotation and tension sensing. First one is a fluid sensor in which the structure successfully distinguishes the density of ethyl alcohol ratio in pure water andethyl alcohol mixture. Secondly, strain sensing is carried out by observing the resonance frequency shift depending on the iron rod thickness which is placed in the center of the hole in the middle of the structure. The last application is determination of the rotation angle in a precise manner. Depending on a metal placed in the resonator with different theta angles ($-90 \leq \theta \leq 90$), the structure responses in different resonance frequencies. The structure demonstrates sensitive and very precise results in terms of the rotation angle.

Manuscript submitted June 28, 2017; revised manuscript received August 29, 2017. Published September 14, 2017.

Sensor applications always attract scientists and engineers. New sensor technologiesare introduced and have been investigated by many scientistsso far. These sensors are based on metamaterials (MTMs) which are materials with unusual electromagnetic responses. By using these extraordinary materials, it is possible to have negative permittivity and permeability simultaneously. MTMs[1-3] are mostly composed of periodic resonators providing the features like, perfect absorption,[4,5] perfect lenses,[6-9] negative refraction,[10-12] invisibility,[13-15] chirality,[16-18] super resolution[19,20] and etc. which cannot be found in regular materials.

Nowadays, many MTM based sensor structures have been developed in microwave regime in terms of the resonance frequency changes. Characterizations and applications of various type of sensing devicesbased on split ring resonator such as liquid and rotation sensing are investigated by Withayachumnankul et al.[21-24] These types of microfluidic sensor devices use the interaction between samples placed in sensor layer and electric field distribution supplied by the microstrip lines. Karaaslan and Bakir succeeded in developing a chiral MTM sensor structure to determine characteristics ofthe samples having especially chirality property.[25] Melik et al. achieved several types of MTM based strain sensor applications to detect mechanical deformation and implantable fracture in microwave frequencies. Those proposed sensor structures are examined on different kinds of polyamide and test instrumentationin the mentioned studies.[26-28] Furthermore, there are many sensor structures based on metamaterial absorber which have been presented by the scientific community in microwave and terahertz frequency regime. Principle of these studies is related on resonance frequency changes of reflected signal from the proposed structures.[29-31] In addition, Bakir et al. investigated various perfect MTM absorber based sensors and energy harvesting applications by using chip resistorswith free space measurement technique.[32,33]

In this paper, we present a metamaterial based sensor with fluid, strain and rotation sensing ability in microwave frequency regime both theoretically and experimentally. The proposed structure has a simple circular split ring resonator (CSRR) topology attached a micro strip transmission line to monitor transmitted signal. Firstly, the operating frequency of the structure is numerically and experimentally examined by assuming the sensor layer is empty. To perform the liquid sensing application, dielectric constant and dielectric loss values of ethanol-water mixture samples are measured in operating frequency band of the sensor by using a dielectric probe kit. Liquid sensing ability of the structure is then numerically analyzed by a simulation software program with respect to the obtained dielectric properties of the mixture. Afterwards, ethanol water mixtures are placed in the sensor layer of the fabricated structure and the energy transmission between two ports (S_{21}) is measured by using a network analyzer. The measurement is repeated for different ratios of the ethanol contentin the mixture. The ratio of ethanol is increased 20% at each test step. Secondly, strain sensing application is demonstrated by using metallic rods with different thickness values. Capacitive property of the CSRR is affected by the rod thickness placed in the sensor layer. Hence, the resonance frequency of the CSRR shifts to a certain frequency point with respect to the variation of the rod thickness. Finally, the rotation sensing application is realized by rotating a metallic rod with a thickness of 0.8 mm. In this work, metallic rod is placed in the sensing layer with different rotation angles varied between $-90 \leq \theta \leq 90$ and the corresponding resonance frequency changesare measured and recorded.

The circular split ring resonators for sensing particular phenomenon in metamaterial based sensor are chosen due to high electromagnetic precision of electrical properties variation of materials placed at the gap of the split ring resonator. Even a small fluctuation of permittivity and loss tangent of the material properties and location in the gap results in a resonance shift to high frequencies. It is due to the surround of the symmetrical properties of split ring with respect to the origin of the circle. The physical mechanism of the proposed circular split ring resonators gives chance to high sensitivity for small changes occurring in the gap.

As to electrical mechanism, whereas the thick transmission line transmits the wave from input to the output port, the split ring resonator mutually interacts with transmission line having higher inductive properties due to thinner line and the gap on the resonator provides a sharp and precision resonance at a fixed frequency level.

Numerical and Experimental Design of the Structure

The proposed sensor structure is constructed by using circular split ring resonator (CSRR) topology with a resonator gap as a sensing layer. A microstrip transmission line which creates magnetic coupling effect with the CSRR inclusion is properly integrated on the

[z]E-mail: sabah@metu.edu.tr

B482 Journal of The Electrochemical Society, 166 (6) B482-B488 (2019)
0013-4651/2019/166(6)/B482/7/$38.00 © The Electrochemical Society

Chemical Liquid and Transformer Oil Condition Sensor Based on Metamaterial-Inspired Labyrinth Resonator

O. Altintaş,[1,2] M. Aksoy,[2] E. Ünal,[1] and M. Karaaslan[1,z]

[1]Iskenderun Technical University, Department of Electrical and Electronics Engineering, Iskenderun, Hatay 31200, Turkey
[2]Cukurova University, Department of Electrical and Electronics Engineering, Saricam, Adana 01330, Turkey

In this study, the labyrinth resonator based chemical liquid and transformer oil condition sensor are presented in a microwave frequency range both numerically and experimentally. The transmission coefficient is observed by the magnetic coupling between the transmission line and resonator which also contains a sensing layer. The sensor structure is tested with the ethanol-water mixtures, methanol-water mixtures and different kind of pure chemical fluidics. In addition, the proposed sensor is used for distinguishing the waste and clean transformer oil sensitively. In the chemical liquids sensing study, linear response characteristics of the sensor have been investigated by the resonance frequency shifts for ethanol-water and methanol-water mixtures. The frequency shifts for each 10% steps of ethanol and methanol content have been monitored as about 25 MHz and 15 MHz, respectively. In the transformer oil condition sensing study, non-destructive methods have been used for providing the long term stability of the sensor structure. In addition, the measured response time between the signal applied from the input port and observation of the transmitted signal from the output port is around 5ns. This value is consistent with the period of the applied signal and the length of the receiver/transmitter cables and the sensor circuit.
 [DOI: 10.1149/2.1101906jes]

Manuscript submitted December 20, 2018; revised manuscript received February 21, 2019. Published April 9, 2019.

Nowadays, there is a growing interest in sensor studies among scientists along with industry 4.0. The robotic technologies with artificial intelligence need novel and more sensitive sensing mechanisms. The new sensing techniques in literature are mostly nondestructive and they response in real time. These techniques provide more precise results with respect to their alternatives. One of the new important sensor techniques is designed by using metamaterials/metasurfaces or left handed materials which are highly used in many application areas such as polarization conversion,[1–4] energy harvesting,[5–8] cloaking,[9–11] antenna[12–14] and etc. The reason why these metamaterial based sensor structures are highly used is their electrical characteristics. The resonator part of the sensor structure has the capacitive and inductive parts which provide strong resonance property. The small electrical changes occurred in the sensor layer of the resonator part allow monitoring the resonance frequency shifts sensitively. In addition, the response time between the applied and transmitted signal is in nanosecond level depending on the period of the applied signal and length of the receiver/transmitter cables and sensor circuit. Hence, this sensing method is highly preferred while the electrical characteristics of the samples are observable.

Many sensor studies have been realized in metamaterial based concept in the last decade. The sensor characterization and some application studies such as humidity, pressure and thickness sensing are realized in Refs. 15–17 at X band frequency regime. These studies use the waveguide measurement technique with proper waveguide adapter and sample holder. In Refs. 18–20, some researchers focus on the detection of the difference between the authentic and inauthentic fuel samples since the fuel adulteration is a big energy and financial problem for the countries. Thin film and strain sensing are also studied by the scientists in the thickness determination concept at terahertz and microwave regime.[21–23] Biosensors can also be designed by using metamaterials. Lee et al. and Torun et al. investigated split ring resonator based sensors to detect biomolecules.[24,25] In Refs. 26–28, the researchers used different type of metamaterial based sensor structure such as 3D plasmonic crystal metamaterials, plasmonic nanorod metamaterials and hyperbolic metamaterials to obtain ultrasensitive sensing mechanism for biosensing. Geng et al. studied a metamaterial biosensor integrated with microfluidics to diagnose liver cancer at terahertz regime.[29] In Refs. 30–33, many microfluidic metamaterial based sensing researches were carried out by using transmission line methods to detect chemical liquids ratios and to characterize sensor behavior at microwave regime.

Another study was realized by Acta in order to analyze the polychlorinated biphenyls in transformer oil by using a microfluidic device. The researchers achieved to detect toxic polychlorinated biphenyls occurred in the transformer oil.[36] In another study, Materon et al. proposed graphene-containing microfluidic and chip-based sensor devices for biomolecules. The scientists succeeded to develop a sensor device which allows to test with a small sample volume and having a high sensitivity and selectivity.[37] In addition to these studies, some review studies based on metamaterial microwave and microfluidic sensors are presented in the literature.[38,39]

In this study, metamaterial based sensor structure is investigated by using transmission line method. Labyrinth resonator integrated transmission line sensor structure is designed both numerically and experimentally. Finite integration technique (FIT) based 3D full wave electromagnetic solver CST Microwave Studio simulation program is used for simulation studies. Agilent Performance Network Analyzer (PNA-L) series vector network analyzer (VNA) and a dielectric probe kit are used to determine dielectric characteristics of the samples and to conduct experimental studies. The sensor structure and proper sample holder are manufactured by LPKF Protomat E33 PCB prototyping machine and a 3D printer. The study is divided into two sections; chemical liquid identification and transformer oil condition detection. Ethanol and methanol content ratios in the ethanol water and methanol water mixtures were already determined in the first study. Moreover, different kinds of chemical fluidics are detected with respect to their dielectric characteristics in this study. Secondly, waste and clean transformer oil is numerically and experimentally distinguished from each other with the help of the proposed sensor structure. The simulated and measured results are in a good agreement with each other and there is approximately 40 MHz frequency difference in both results. The sensor structure can be used in energy, chemical and medicine industries for many applications including dielectric characterization of fluidics, fuel adulteration sensing application and etc.

Theory and Design

The sensor structure has the transmission line integrated resonator-based architecture. The design and numerical studies are performed by using a full wave finite integration technique (FIT) solver based CST Microwave Studio simulation program. The resonator part of the proposed sensor structure has a unique labyrinth resonator (LR) design which attracts the attention of the researchers working on the metamaterial concept. The labyrinth resonator[30] consists of five nested double split ring resonators (DSRR) with a gap called sensor layer in

[z]E-mail: mehmetkaraaslan@iste.edu.tr

Double Split Ring Resonator Based Microfluidic Sensor for Wastewater Treatment Applications

Olcay Altıntaş[1, 2, a)], Murat Aksoy[2], Emin Ünal[1] and Muharrem Karaaslan[1]

[1] *Iskenderun Technical University, Department of Electrical and Electronics Engineering, Hatay 31200, Turkey*
[2] *Cukurova University, Department of Electrical and Electronics Engineering, Adana 01330, Turkey*

a)Corresponding author: olcay.altintas@iste.edu.tr

Abstract. In this study, microfluidic sensor structure has been proposed for wastewater treatment applications. Resonator part of the proposed sensor consist of double split ring resonator (DSSR) integrated transmission lines to observe transmission coefficient at resonance frequency. The wastewater samples are obtained at different phases in a treatment process such as ventilation, back return and output. The dielectric characteristics of these samples are measured via a dielectric probe connecting with a vector network analyzer. After that the samples are placed in the capacitive parts of the DSSR and the transmission coefficient are observed in resonance frequencies. They are obtained at 1.758 GHz, 1.766 GHz and 1.854 GHz for output, back return and ventilation process, respectively. These results are related with the chemical properties of samples such as amount of suspended solid, colloid and/or organic/inorganic matter. Hence the sensor is a candidate for wastewater treatment applications.

INTRODUCTION

The split ring resonator (SRR) is the first known design in metamaterial concept which is related with manmade material with unnatural electromagnetic properties such as negative permittivity, negative permeability and negative refraction etc. The metamaterials are used and examined in many applications areas like energy harvesters, polarization converters and antennas etc [1-9]. The metamaterial is also highly used in sensing applications by the researchers [10-14]. Metamaterial absorber based circular split ring resonator type structure has been designed for microfluidic, strain and rotation sensing application [10]. The other metamaterial based sensor structure has the chirality property and it has been used for discriminate the authentic and inauthentic fuel samples [11]. Labyrinth type sensor structure has been realized for transformer oil condition detection study at microwave frequency regime [12]. A split meander line resonator based sensor structure has been designed for determining dielectric characteristics of the solid samples having flat surface [13]. The swastika shaped metamaterial absorber based sensor structure has been achieved for detection various chemical liquids at X band [14].

The sensing application has been realized for a wastewater treatment facility in three different phases such as output, back return and ventilation. The wastewater is processed in all these three phases and the amount of suspended solid is measured in mg. The condition of the water is then determined. Hence this study offers a novel wastewater condition detection method by using the electrical characteristics of the samples. In this method, the electrical properties of the samples are measured between 1.5 GHz and 2 GHz. After that the double split ring resonator with strong resonance property has been designed by integrating transmission line to observe transmitted power in resonance frequency. Finally samples are placed into the sensor layer of the proposed sensor structure and the resonance frequencies are observed. The linear relationship is observed between the dielectric characteristic and resonance frequency. The proposed structure offer cheaper and safer measurement method for wastewater condition detection applications.

DESIGN OF THE STRUCTURE

The resonator part of the proposed sensor structure has been designed by inspiring double split ring resonator type metamaterial as shown in Figure 1(a). The transmission line is integrated to the resonator to observe transmission

Turkish Physical Society 35th International Physics Congress (TPS35)
AIP Conf. Proc. 2178, 030011-1–030011-4; https://doi.org/10.1063/1.5135409
Published by AIP Publishing. 978-0-7354-1925-4/$30.00

Journal of ELECTRONIC MATERIALS
https://doi.org/10.1007/s11664-018-6528-7

A Split Meander Line Resonator-Based Permittivity and Thickness Sensor Design for Dielectric Materials with Flat Surface

OLCAY ALTINTAS,[1,2] MURAT AKSOY,[2] EMIN UNAL,[1] FATOS KARAKASLI,[1] and MUHARREM KARAASLAN[1,3]

1.—Department of Electrical and Electronics Engineering, Iskenderun Technical University, 31200 Iskenderun, Hatay, Turkey. 2.—Department of Electrical and Electronics Engineering, Cukurova University, 01330 Saricam, Adana, Turkey. 3.—e-mail: muharrem.karaaslan@iste.edu.tr

A metamaterial-based permittivity and thickness sensor structure for dielectric substrate material has been proposed at the X band frequency regime. The sensor structure is designed by using a split meander line type resonator and examining it both numerically and experimentally. Various types of dielectric substrate samples have been used to verify the precise sensing characteristics of the proposed sensor. The sensor layer has been chosen as the back side of the sensor structure, and the reflection frequency of the incident signal has been examined. The sensor layer thickness has been varied from 0.4 mm to 1.6 mm for the thickness sensing study with two different types of dielectric substrate having the same electromagnetic characteristics. The permittivity sensing study has been carried out by several dielectric materials which have permittivity values between 10.20 and 1.96. The proposed sensor structure can be effectively used in many application areas such as microwave material design, the defense industry and in medical devices.

Key words: Metamaterial, sensor, permittivity, thickness

INTRODUCTION

Recently, it has been a very specific issue to meet military, medical or other industrial needs by improving new precise sensing techniques. Scientists are making huge efforts to investigate more sensitive structures by exploring new technological areas. Metamaterial- (MTM) and metasurface/metafilm (MS)[1] -based sensor structures are among rising trends in the sensor design area. These materials are known as double-negative media and they are mostly designed by using split ring resonators (SRRs) and their derivatives. Moreover, MTMs or MSs provide many extraordinary features such as negative refraction,[2] signal absorption,[3,4] polarization conversion,[5–7] cloaking[8,9] and super lens,[10,11] etc.

(Received March 7, 2018; accepted July 13, 2018)

In the last decade, researchers have developed various types of MTM-based sensor structures for many application areas,[12–25] and many MTM-based microfluidic sensor designs have been achieved.[12–15] These types of designs are based on the transmission magnitude or transmission frequency of the incident signal. The samples, which are placed in microfluidic channels, can affect the overall capacitance value of the sensor structures. Some other MTM-based studies have focused on determining the dielectric characterization of the liquid or solid samples in the X band.[16–19] The other topic is thin film sensing, which has been carried out by using split ring resonators for microwave applications.[20,21] In addition to these studies, MTM-based sensor structures have been used for medical and chemical purposes,[22–25] while some of them have been used for bio-sensing purposes such as cancer detection or blood glucose monitoring in the microwave frequency regime.[22–24] Moreover, various types of hazardous material detection studies have

Published online: 20 July 2018

Physica E 116 (2020) 113724

Contents lists available at ScienceDirect

Physica E: Low-dimensional Systems and Nanostructures

journal homepage: http://www.elsevier.com/locate/physe

Design of a metamaterial inspired omega shaped resonator based sensor for industrial implementations

Olcay Altıntaş [a,b,*], Murat Aksoy [b], Emin Ünal [a]

[a] Iskenderun Technical University, Department of Electrical and Electronics Engineering, Iskenderun, Hatay, 31200, Turkey
[b] Cukurova University, Department of Electrical and Electronics Engineering, Saricam, Adana, 01330, Turkey

ARTICLE INFO

Keywords:
Metamaterial
Dielectric
Fuel adulteration
Oil condition

ABSTRACT

In this study, the omega shaped resonator based sensor structure by inspiring of metamaterial (MTM) concept is presented at X-band frequency regime for industrial purpose both numerically and experimentally. Four distinguishing applications which are (i) authentic and inauthentic gasoline samples, (ii) authentic and inauthentic diesel samples, (iii) clean and waste lubricant samples and (iv) clean and waste transformer oil samples have been realized by determining dielectric properties of them. Although there are close dielectric constant values between the samples (about 0.65 for (i), 0.25 for (ii), 0.10 for (iii) and 0.15 for (iv)), the proposed sensor sensitively discriminates all sample groups with about a frequency shift of 250 MHz for (i), 180 MHz for (ii), 60 MHz for (iii) and 70 MHz for (iv). Sensor structure can be efficiently used many industrial applications since the results are sensitively and precisely obtained for proposed studies. In addition, the proposed sensor is durable, suitable for real-time applications and long-term stability considering the fabrication technique and nondestructive measurement method.

1. Introduction

Recently, the scientists focus on the high-tech sensors since the Industry 4.0 concept needs the sensor devices which have real-time operated, without requiring human resources and more precise. Moreover, some sectors ask for the sensing mechanism which can be achieved more sensitive, durable and long term stability with non-destructive methods. Hence, the researchers have investigated the metamaterial (MTM) based sensor structures to obtained novel and improved sensing characteristics. The MTM concept has been a popular research area among the scientists at the last decade. It has non-natural properties which are negative refraction index, reverse Snell Law and reverse Doppler Effect etc. Many applications and studies have been realized by the researchers in the topics such as absorbers [1,2], energy harvesters [3–5], polarization converters [6,7], super lenses [8,9], antennas [10, 11] and sensors [12–29].

Lots of MTM based sensor studies in the literature have been carried out in different approaches. Albishi et al. proposed a highly sensitive MTM based sensor structure which can be detected the cracks in the metallic materials [12]. Gargari et al. studied a wireless MTM inspired rotation sensor. Their sensing mechanism has sub milliradian resolution to measure elastic-region bending in materials such as steel [13]. Altintas et al. designed a circular split ring resonator for multipurpose sensing applications such as dielectric characterization of liquids, rotation detection of rods and strain sensing [14]. Saghati et al. improved a transmission line integrated sensor structure for dielectric spectroscopy of liquid chemicals in a wideband frequency regime both numerically and experimentally [15]. Wu et al. implemented a rectangular complementary-ring resonator based sensor to monitor permittivity of liquids at a working frequency of 900 MHz [16]. He et al. realized a thin film sensing application by using a tip shaped split ring resonator (SRR) MTM at microwave frequency regime [17]. Ni et al. proposed an MTM absorber based sensor structure to observe humidity of environment [18]. Keshavarz et al. realized an ultrahigh sensitive temperature sensor structure based on graphene semiconductor MTM in terahertz (THz) frequency regime [19]. Tumkaya et al. designed a MTM based sensor structure at X-band to discriminate authentic and inauthentic fuel samples [20]. Bakir et al. proposed a microfluidic and fuel adulteration sensing mechanism by using chiral MTM based structure in microwaves [21]. Tamer et al. investigated a transmission line based sensor for determining authentic and inauthentic gasoline samples [22]. Shahmarvandi et al. implemented a CMOS MTM absorber based gas sensing

* Corresponding author. Cukurova University, Department of Electrical and Electronics Engineering, Saricam, Adana, 01330, Turkey.
E-mail address: olcay.altintas@iste.edu.tr (O. Altintas).

https://doi.org/10.1016/j.physe.2019.113724
Received 8 July 2019; Received in revised form 29 August 2019; Accepted 21 September 2019
Available online 27 September 2019

Metamaterial Inspired Sensor for Detection of Engine Lubricant Oil Condition

Olcay Altıntaş[1, 2, a)], Murat Aksoy[2], Emin Ünal[1] and Muharrem Karaaslan[1]

[1] *Iskenderun Technical University, Department of Electrical and Electronics Engineering, Hatay 31200, Turkey*
[2] *Cukurova University, Department of Electrical and Electronics Engineering, Adana 01330, Turkey*

a)Corresponding author: olcay.altintas@iste.edu.tr

Abstract. A metamaterial (MTM) based sensor structure is proposed to determine engine lubricant condition at X band frequency regime. The resonator part of the structure is inspired electric LC resonator (ELC) type MTM which is highly used among the researchers. The sensing application is realized by benefiting the electrical properties of the lubricant samples. The dielectric characteristics of the clean and waste lubricant oils are measured by using a vector network analyzer and dielectric probe kit. The dielectric values are observed as about 2.35+j0.31 and 2.45+j0.34 for clean and waste oil samples, respectively. After, the ELC resonator based sensor structure are designed by including a sensor layer at the back. Finally, transmission resonance frequencies and phases are measured for both samples. The transmission coefficients are obtained nearly zero at 8.572 GHz and 8.664 GHz. Hence, the proposed sensor structure can distinguish the clean and waste lubricant oil samples with about 100 MHz.

INTRODUCTION

Metamaterials (MTMs) have unique electromagnetic properties such as simultaneously negative permeability and permittivity, negative refraction, reverse Cherenkov and reverse Doppler effects etc. Researchers have used those about 20 years for many different studies. Many researches in different fields such as absorber, antenna, energy harvesting, polarization rotator and sensor have been efficiently improved by using the MTM concept [1-14].

Lots of metamaterial based sensor studies have been realized by the researchers at different operating frequency ranges. The permittivity characteristic and thickness determination study had been realized X band frequency regime by using a split meander line resonator design [10]. A metamaterial absorber based design was used to detect the chemical liquid samples with respect to their electrical characteristics [11]. Chemical liquid sample and transformer oil condition detection application had been achieved by using metamaterial inspired transmission line integrated sensor structure [12]. A chiral metamaterial sensor is designed for microfluidic and fuel adulteration sensing implementations [13]. Multiple sensing applications such as fluid, strain and rotation had been realized by using a transmission line integrated circular split ring resonator based sensor structure [14].

In this study, the electric LC type resonator has been designed at X band frequency regime for engine lube oil condition detection application. Two engine lubricant samples as clean and waste lubricant have been used. The electrical characteristics of the samples firstly measured by using a dielectric probe. After that the lubricant condition study has been realized by placing the sample to the sensing layer. Transmission coefficients are observed at near zero at the resonance frequencies. Finally, 100 MHz of resonance frequency difference are monitored between two lubricant samples. The sensor structure is a good candidate such an industrial application at microwave frequency regime.

Turkish Physical Society 35th International Physics Congress (TPS35)
AIP Conf. Proc. 2178, 030010-1–030010-4; https://doi.org/10.1063/1.5135408
Published by AIP Publishing. 978-0-7354-1925-4/$30.00

Measurement 145 (2019) 678–686

Contents lists available at ScienceDirect

Measurement

journal homepage: www.elsevier.com/locate/measurement

Artificial neural network approach for locomotive maintenance by monitoring dielectric properties of engine lubricant

Olcay Altıntaş [a,b], Murat Aksoy [b], Emin Ünal [a], Oğuzhan Akgöl [a], Muharrem Karaaslan [a,*]

[a] Iskenderun Technical University, Department of Electrical and Electronics Engineering, Iskenderun, Hatay 31200, Turkey
[b] Cukurova University, Department of Electrical and Electronics Engineering, Saricam, Adana 01330, Turkey

A R T I C L E I N F O

Article history:
Received 16 February 2019
Received in revised form 27 April 2019
Accepted 25 May 2019
Available online 31 May 2019

Keywords:
Spectral analysis
Dielectric measurement
Artificial neural network
Engine lubricant

A B S T R A C T

In this paper, we proposed an approach for locomotive maintenance systems by observing engine lube oil. The mechanical particles in lube oil give information about locomotive engine system condition. The engine lubricant is monthly monitored by a spectral analyzer (SA) to detect engine system failure and routine maintenance time. However, this old fashioned technique has many disadvantages such as non-real time measuring, high cost and time consumption. A novel approach is proposed to eliminate these disadvantages. The new method determines the lubricant sample conditions with respect to electrical characteristics by using artificial neural network (ANN). The study focuses on a relationship between mechanical particles (in ppm) and dielectric characteristics of the lube oil samples. Therefore, ANN method is applied to observe linear relation between observed and predicted dielectric constant and loss factor values of the engine oil samples. The electrical characteristics of the samples are observed at four frequency points (2.40 GHz, 5.80 GHz, 7.40 GHz and 9.60 GHz). ANN studies are realized by using data at these frequency points. The regression (R) coefficients are obtained as 0.7239, 0.7951, 0.8513 and 0.7463 for dielectric constant and 0.7627, 0.7196, 0.8015 and 0.7334 for dielectric loss, respectively. Moreover, the mean square error (MSE), mean absolute error (MAE) and mean absolute percentage error (MAPE) are calculated and examined. The obtained results are very sufficient and this approach can be applied to a sensor device having low cost and real time working mechanism in the future.

1. Introduction

Nowadays, transportation is a very crucial phenomenon in terms of economic developments or comfort and safety demanded by humans. One of the fast, economical and reliable transportation systems are railways. The locomotives on railways have huge power engine systems and their maintenance is very important for safety and cost of journeys or commercial consignments. Detecting engine failures and maintenance times can be realized by observing engine lubricant conditions. The particles which are occurred by depreciation of mechanical parts of engine systems are mixed to the engine lube oil. When a certain amount of mechanical particle inside the sample exceeds the limit, mechanical parts of the engine must be urgently checked. According to the existing maintenance technique, the engine systems of locomotives should be checked and a lubricant sample should be taken from every station where a locomotive arrives in order to observe engine and oil conditions through a spectral analyzer (SA) device based on spectral analysis method. Spectral analysis is a method which uses Taylor series model to determine particular physical problems, process and analyze data in spectral basis [1]. This method examines the power distribution over frequency domain for finite data sequence and it takes part in many applied research fields such as meteorology, radar and sonar systems, medicine, seismology and so on [2–9]. The SA device is made by using this spectral analysis method to determine contamination and condition of engine lube oil. There are many disadvantages (such as non-real time testing, high cost and time consumption) of detecting engine failures from oil condition by using a SA whereas its results are in high accuracy.

Many methods for calculating and measuring dielectric properties of numerous materials or various mixtures are used by the scientific committee [22–28]. Venkatesh and Raghavan presented several experimental methods such as resonance cavity, open cavity, free-space transmission, reflected wave and coaxial transmission method for measuring dielectric properties of materials [22]. Yingzhon et al. proposed two-channel and differential dielectric spectroscopy measurement method for lubricant oil [23]. An impedance converter chip is designed for this dielectric spectroscopy

* Corresponding author.
E-mail address: muharrem.karaaslan@iste.edu.tr (M. Karaaslan).

https://doi.org/10.1016/j.measurement.2019.05.087
0263-2241/